



# DEPARTMENT OF PHYSICS

UNIVERSITY OF CAPE TOWN

IYUNIVESITHI YASEKAPA • UNIVERSITEIT VAN KAAPSTAD

Search for  $tWZ$  production in the Full Run 2 ATLAS  
dataset using events with four leptons

Jake Reich

Student Number: RCHJAK001

Supervisor: Dr. James Keaveney

Co-Supervisor: Dr. Sahal Yacoob

A thesis submitted in fulfilment  
of the requirements for the degree of  
Master in Science

August 2021

# Abstract

The search for  $tWZ$  production using  $139 \text{ fb}^{-1}$  of  $pp$  collision data at a centre-of-mass energy of  $\sqrt{s} = 13 \text{ TeV}$ , recorded by the ATLAS experiment at CERN, is presented. Events containing exactly four electrons or muons (tetralepton) are selected with additional criteria based on the number of jets, the number of  $b$ -tagged jets, and the number of  $Z$  boson candidates are used to define signal and control regions. The large  $t\bar{t}Z$  and  $ZZ$  backgrounds are distinguished from signal by a BDT-based algorithm. Inputs to the BDT-based algorithm include, a kinematic reconstruction algorithm which reconstructs leptonically decaying top quarks and a BDT-based algorithm which aims to classify  $\ell b$  systems originating from top quarks. The expected signal strength is extracted via a blinded maximum-likelihood fit to multiple signal and control regions. The measured signal strength is  $\mu(tWZ) = 1.91^{+0.95}_{-0.82}$ , leading to an expected significance of  $1.44\sigma$ . An expected upper limit on the signal strength is set and is given by  $\mu_{up}^{exp} = 1.61^{+2.35}_{-1.16}$ . Furthermore, a combined blinded maximum-likelihood fit was performed across the tetralepton and trilepton (studied in an independent analysis by Benjamin Warren (UCT) [80]) channels, to further increase the sensitivity of  $\sigma(tWZ)$ . The measured signal strength is  $\mu(tWZ) = 1.80^{+0.70}_{-0.65}$ , leading to an expected significance of  $1.61\sigma$ . An expected upper limit on the signal strength is set and is given by  $\mu_{up}^{exp} = 1.43^{+2.04}_{-1.03}$ .

# Declaration

*17 I certify that this assignment/report is my own work, based on my personal study and/or research and that I have  
18 acknowledged all material and sources used in its preparation, whether they be books, articles, reports, lecture notes,  
19 and any other kind of document, electronic or personal communication. I also certify that this assignment/report  
20 has not previously been submitted for assessment in any other unit, except where specific permission has been granted  
21 from all unit coordinators involved, or at any other time in this unit, and that I have not copied in part or whole  
22 or otherwise plagiarised the work of other students and/or persons.*

# Acknowledgements

24

# Contents

25	<b>1 Introduction</b>	7
26	<b>2 Theory</b>	8
27	2.1 Standard Model of Particle Physics . . . . .	8
28	2.1.1 The Top Quark . . . . .	9
29	2.2 $tWZ$ . . . . .	10
30	2.2.1 Tetralepton Channel . . . . .	10
31	2.2.2 Comparison to Trilepton Channel . . . . .	11
32	2.2.3 Motivation for the search for $tWZ$ production in the tetralepton channel . . . . .	12
33	<b>3 The ATLAS Experiment and Detector</b>	13
34	3.1 The ATLAS Experiment . . . . .	13
35	3.1.1 Large Hadron Collider (LHC) . . . . .	13
36	3.2 The ATLAS Detector . . . . .	14
37	3.2.1 Coordinate System and Kinematics . . . . .	15
38	3.2.2 Inner Detector . . . . .	15
39	3.2.3 Electromagnetic and Hadronic Calorimeters . . . . .	16
40	3.2.4 Muon Spectrometer . . . . .	16
41	3.2.5 Trigger and Data Acquisition System . . . . .	16
42	3.2.6 Particle Identification and Object Reconstruction . . . . .	16
43	<b>4 Analysis Setup and Strategy</b>	19
44	4.1 Data and Monte Carlo Simulation . . . . .	19
45	4.1.1 Data Samples . . . . .	19
46	4.1.2 Monte Carlo Samples . . . . .	19
47	4.2 Objects . . . . .	20
48	4.2.1 Leptons . . . . .	21
49	4.2.2 Jets . . . . .	21
50	4.2.3 $b$ -tagging . . . . .	22
51	4.3 Kinematic cuts . . . . .	22
52	4.4 Regions and Event Selection . . . . .	22
53	4.4.1 Optimization studies for event selection . . . . .	23
54	4.5 Signal and Control Regions . . . . .	26
55	4.5.1 $tWZ$ OF SR . . . . .	26
56	4.5.2 $tWZ$ SF SR . . . . .	27
57	4.5.3 $t\bar{t}Z$ CR . . . . .	28
58	4.5.4 $Z Z b$ CR . . . . .	28
59	4.5.5 $(tWZ)_{\text{fake}}$ CR . . . . .	40
60	4.6 Fake Lepton Estimation . . . . .	40
61	4.7 Machine Learning Techniques . . . . .	44
62	4.7.1 Object-level BDT . . . . .	46
63	4.7.2 Event-level BDT . . . . .	51
64	4.8 Two Neutrino Scanning Method ( $2\nu\text{SM}$ ) Algorithm . . . . .	56
65	4.8.1 The algorithm . . . . .	57
66	4.8.2 Calculating $w_{2\nu\text{SM}}$ . . . . .	58

67	4.8.3 Kinematic Veto . . . . .	59
68	4.9 Systematics . . . . .	61
69	4.9.1 Experimental uncertainties . . . . .	62
70	4.9.2 Theoretical uncertainties . . . . .	63
71	4.9.3 Generic shape systematics . . . . .	64
72	4.10 Analysis Pipeline and TRexFitter . . . . .	65
73	4.10.1 Fitting Procedure . . . . .	65
74	4.11 Results . . . . .	66
75	4.11.1 Tetralepton Channel . . . . .	66
76	4.11.2 Trilepton and Tetralepton Channels . . . . .	69
77	<b>5 Conclusion</b>	<b>74</b>

78

# Chapter 1

79

## Introduction

80 The production of a single top quark in association with a  $W^\pm$  and  $Z$  boson ( $tW^\pm Z$ ) at the CERN LHC is sensitive  
 81 to both the neutral and charged electroweak couplings of the top quark as the process involves the simultaneous  
 82 production of a  $W$  boson and a  $Z$  boson in association with the top quark. Due to the very large coupling of the  
 83 top quark to the Higgs boson, the electroweak couplings of the top quark are a theoretically well-motivated area in  
 84 which to search for the first signs of new physics. The recent lack of signs of new physics from LHC data tells us  
 85 that new physics is either very heavy, or is very weakly coupled to Standard Model particles, therefore we might  
 86 only observe signs of new physics in anomalous rates of well-chosen processes. A prime example of such a process  
 87 is  $tWZ$ . This has an extremely low production cross section (0.7 fb for  $\sqrt{s} = 13$  TeV [24]), meaning that it is an  
 88 extremely rare process to observe and subsequently, it has never been observed by any particle physics experiment.  
 89 However, the latest datasets recorded by the ATLAS experiment at the CERN LHC are sufficiently large to allow  
 90 a potential observation of this rare process. We use the Full Run 2 dataset recorded by the ATLAS to search for  
 91 the production of a top quark together with a  $W^\pm$  and  $Z$  boson in the channel with four leptons (two originating  
 92 from the decay of the  $Z$  boson, one from the associated  $W$  boson and one from the  $W$  boson which decays from  
 93 the top quark (together with a  $b$  quark)). In this analysis, we use a kinematic reconstruction technique which aims  
 94 to discriminate between  $tWZ$  and our most prominent background process,  $t\bar{t}Z$ . In addition to this, we implement  
 95 Machine Learning techniques (Boosted Decision Trees) to further isolate our  $tWZ$  signal. The dominant source of  
 96 the fake lepton background is from  $t\bar{t}Z$  events containing at least one fake lepton. The kinematic distributions of  
 97 this background are taken from simulation and its normalisation is constrained using a dedicated control region. As  
 98 this work forms the basis of an official ATLAS analysis, only blinded results are shown. A maximum likelihood fit  
 99 (blinded) is performed over our two  $tWZ$  signal regions and three control regions, measure the cross section of  $tWZ$   
 100 in the tetralepton channel. In order to increase the sensitivity of our  $tWZ$  signal, we perform another maximum  
 likelihood fit (blinded) over all regions defined for the tetralepton channel and the trilepton channel<sup>1</sup>.

---

<sup>1</sup>an independent analysis conducted by Benjamin Warren (University of Cape Town) [80]

102

# Chapter 2

103

## Theory

### 2.1 Standard Model of Particle Physics

104 The Standard Model (SM) is a Quantum Field Theory (QFT) which classifies all known elementary particles and describes their interactions. It is a well-tested model and has shown to be hugely successful in describing experimental data to great precision [altarelli2014higgs]. It incorporates three of the four fundamental forces of nature: the electromagnetic, the weak and the strong forces. In Figure 2.1, all known elementary particles described by the SM, are shown.

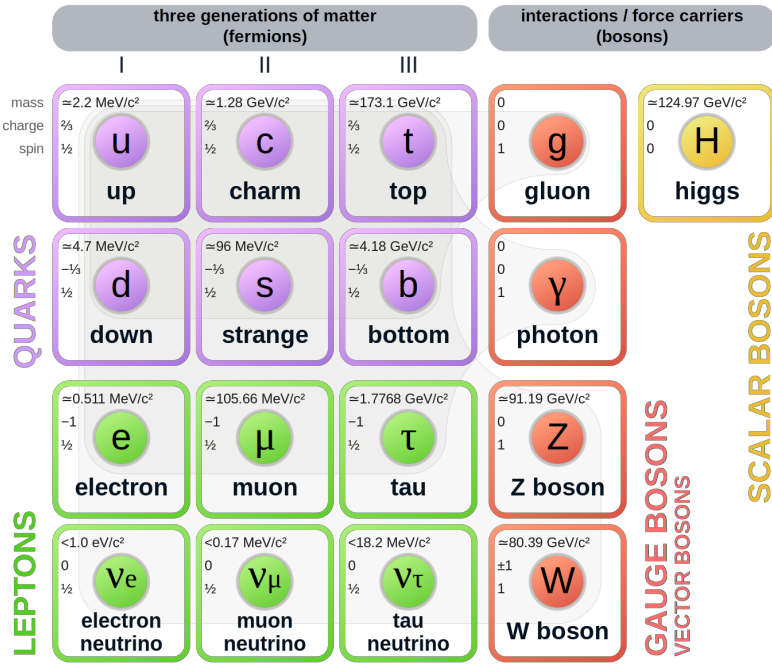


Figure 2.1: A summary of the elementary particles described by the SM [63] is shown. Fermions are shown on the left, with quarks shown in purple and leptons shown in green. Bosons are shown on the right, with gauge bosons shown in red and the Higgs boson shown in yellow. The mass, electric charge and spin of each particle is shown on the top left of each particle's block.

110 SM particles are uniquely described by their quantum numbers: mass, electric charge and spin. The SM particles  
 111 are split into main two classes, based off their spin quantum numbers. Particles which have half-integer spin are  
 112 called fermions, and those which have integer spin are called bosons. Fermions are further divided into three gener-  
 113 ations, each comprising of two quarks, one charged lepton and one neutrino. The particles of each generation have  
 114 identical electric charge and spin, but their masses differ. The masses of the particles in a generation increase with  
 115 increasing generation number, with generation 1 particles being the least massive and generation 3 particles being

116 the most massive. Quarks carry electric and colour charge, and can therefore interact via the electromagnetic, weak  
 117 and strong forces. Colour charge can take on three values: red, green and blue. Due to colour confinement [81],  
 118 quarks cannot be isolated from one another. They exist in colourless bound states, called hadrons, consisting of  
 119 two or more quarks. Hadrons consisting of an even number of quarks are known as mesons and those consisting of  
 120 an odd number of quarks are known as baryons. On the other hand, charged leptons (electron ( $e$ ), muon ( $\mu$ ) and  
 121 tau ( $\tau$ )) only carry electric charge and can therefore interact electromagnetically and weakly, but not through the  
 122 strong interaction. The electric and colour neutral fermions, neutrinos, can only interact via the weak force.

123  
 124 Particles are able to interact with one-another via the exchange of a gauge boson (boson with spin-1). Photons  
 125 are massless, spin-1 gauge bosons which mediate electromagnetic interactions between particles which carry electric  
 126 charge, such as quarks and charged leptons ( $e$ ,  $\mu$  and  $\tau$ ). The weak interaction is mediated by three massive gauge  
 127 bosons, the electrically charged  $W^+$  and  $W^-$  bosons and the electrically neutral  $Z$  boson. Gluons are massless,  
 128 spin-1 gauge bosons which mediate strong interactions between particles which carry colour charge, such as quarks.  
 129 Since gluons carry colour charge, they interact with themselves.

130  
 131 The massive, spin-0, electrically neutral Higgs boson mediates the Higgs field which gives mass to the  $W^\pm$  and  $Z$   
 132 bosons via the so-called Brout-Englert-Higgs mechanism [41, 49, 48]. The Brout-Englert-Higgs mechanism induces  
 133 spontaneous electroweak symmetry breaking to provide mass terms for the  $W^\pm$  and  $Z$  bosons in the electroweak  
 134 Lagrangian of the SM.

135  
 136 All particles described in the SM have their own antiparticle, with the same mass, but opposite charges. Some  
 137 particles, such as the photon, are their own antiparticle.

138  
 139 Although the SM has shown to be hugely successful, it is incomplete and fails to describe certain observed phenomena.  
 140 The most notable example being the absence of gravity from the SM. The gravitational force is  $\approx 10^{29}$  [74]  
 141 weaker than the weak force, therefore quantum gravitational effects are expected to only become significant at  
 142 energies much larger than that currently accessible by the LHC (known as the Planck scale  $\approx 10^9$  GeV) [53]. This  
 143 large difference in strength between the weak force and gravity is known as the Hierarchy Problem. Cosmological  
 144 observations infer that around 84% of the matter in the universe consists of gravitationally interacting matter known  
 145 as dark matter [52]. None of the particles described in the SM are good dark matter candidates, therefore the SM  
 146 only accounts for a small fraction of the total matter of the universe. The large discrepancy between the observed  
 147 amount of matter and antimatter in the universe, sometimes referred to as the matter-antimatter asymmetry, is  
 148 unable to be fully explained by the SM. Neutrinos in the SM are assumed to be massless, however observations  
 149 of neutrino oscillations (neutrinos undergoing flavour change as they travel through space) imply that neutrinos  
 150 do have mass [44]. Beyond the Standard Model (BSM) theories attempt to explain the phenomena which the SM  
 151 cannot. For example, a popular extension to the SM, Supersymmetry (SUSY) introduces new particles to the SM  
 152 which are counterparts to the existing SM particles with the same quantum numbers, except for their spins [55].  
 153 SUSY provides elegant explanations to many shortcomings of the SM, however none of the supersymmetric particles  
 154 described by SUSY have been observed experimentally [29].

### 155 2.1.1 The Top Quark

156 The top quark is the heaviest particle in the SM, with a mass of  $172.76 \pm 0.30$  GeV [47]. Since the coupling to  
 157 the Higgs boson is proportional to the mass of the interacting particle, the top quark is strongly coupled to the  
 158 Higgs boson. Physics processes involving top quarks is therefore a theoretically well-motivated area to search for  
 159 new physics, since it is the most likely particle to couple to new physics theories at the TeV scale. Its large mass  
 160 also makes it highly unstable, with a mean lifetime of  $\approx 0.5 \times 10^{-24}$  s [47]. The top quark's lifetime is shorter than  
 161 that of the hadronisation process, and it therefore decays before hadronising. We therefore cannot measure the top  
 162 quark directly, but indirectly via its decay products. Top quarks almost always decay to a  $W$  boson and a  $b$ -quark  
 163 ( $\frac{\Gamma(Wb)}{\Gamma(Wq(q=b,s,d))} = 0.957 \pm 0.034$  [47]).  $b$ -quarks are the second heaviest quark in the SM, however their lifetimes are  
 164 still longer than the hadronisation time scale [47]. In hadron collider experiments,  $b$ -quarks travel a short distance  
 165 in the detector before hadronising to form jets. In Table 2.1, the dominant final state branching fractions of the  
 166 top quark, are shown.

167 Hadronic final states are more than twice as likely than leptonic final states. Final state decays to different lepton  
 168 flavours are roughly equally probable.

169 Top quark production can be placed into two main categories: pair production ( $t\bar{t}$ ) and single-top production ( $t$ ) [72].

Decay Mode	Branching Fraction ( $\frac{\Gamma_i}{\Gamma}$ )
$t \rightarrow Wb \rightarrow e\nu_e b$	$(11.10 \pm 0.30)\%$
$t \rightarrow Wb \rightarrow \mu\nu_\mu b$	$(11.40 \pm 0.20)\%$
$t \rightarrow Wb \rightarrow \tau\nu_\tau b$	$(10.70 \pm 0.50)\%$
$t \rightarrow Wb \rightarrow q\bar{q}b$	$(66.50 \pm 1.40)\%$

Table 2.1: The dominant final state branching fractions of the top quark [47] are shown.

In the LHC, top quarks are mainly produced in pairs via strong interactions in gluon-gluon fusion ( $gg \rightarrow t\bar{t}$ ) or quark annihilation ( $q\bar{q} \rightarrow t\bar{t}$ ). Top quark production via gluon-gluon fusion is the dominating process, since gluons are the most dominant particles produced in  $pp$  collisions in the LHC [23]. The production cross section for  $t\bar{t}$  (leptonic final state) in  $pp$  collisions with  $\sqrt{s} = 13$  TeV was measured by ATLAS with a value of  $830 \pm 0.4(\text{stat}) \pm 36(\text{syst}) \pm 14(\text{lumi})$  pb [4], with good agreement between measurement and theoretical prediction.

The most abundant mechanisms leading to single top production include, those involving the exchange of a  $W$  boson and those involving the production of a top quark in association with a  $W$  boson [47]. In Table 2.2, single top production cross sections in  $pp$  collisions at  $\sqrt{s} = 13$  TeV for various channels, are shown.

Process	Total Cross Section [pb]
$bq' \rightarrow W \rightarrow tq$	$216.99^{+9.04}_{-7.71}$
$q\bar{q}' \rightarrow W \rightarrow \bar{b}t$	$10.32^{+0.40}_{-0.36}$
$bg \rightarrow b/t \rightarrow Wt$	$71.7 \pm 3.85$

Table 2.2: Single top production cross sections in  $pp$  collisions at  $\sqrt{s} = 13$  TeV for various channels [30] are shown. The prime superscript on  $q'$  indicates that the quark has a different flavour to  $q$ .

Single top production is suppressed compared to pair produced top production, with  $t\bar{t}$  production (leptonic final state) being around three times as likely to occur than single top production across all decay channels.

## 2.2 $tWZ$

### 2.2.1 Tetralepton Channel

In Figure 2.2, the Leading Order (LO) Feynman diagram for  $tWZ$  in the tetralepton channel, is shown.

#### 2.2.1.1 Backgrounds

The main backgrounds for  $tWZ$  (tetralepton channel) are the production of a two tops, both in the  $\ell\nu b$  final state channel, together with a  $Z$  boson ( $t\bar{t}Z$ ) and diboson production with fully leptonic final states ( $ZZ$ ). In Figure 2.2.1.1, LO Feynman diagrams for  $t\bar{t}Z$  and  $ZZ$  in the tetralepton channel, are shown.

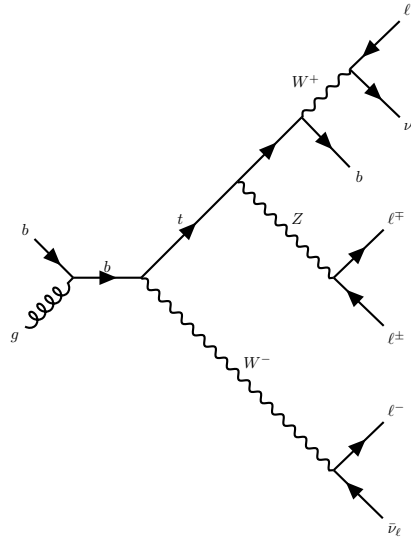


Figure 2.2: The LO Feynman diagram of  $tWZ$  production in the tetralepton channel is shown.

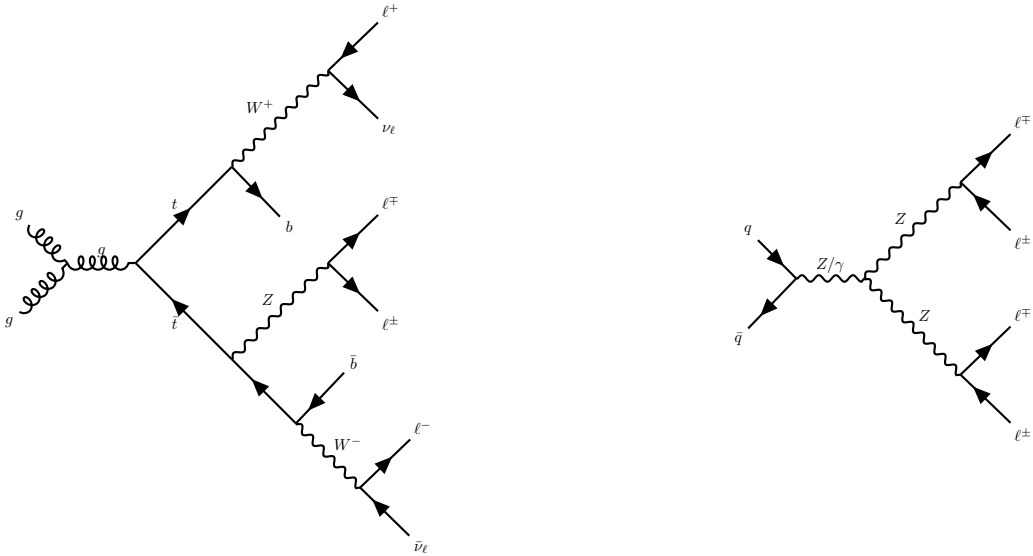


Figure 2.3: LO Feynman diagrams for  $t\bar{t}Z$  (left) and  $ZZ$  (right) in the tetralepton channel are shown.

$t\bar{t}Z$  contains four leptons and two  $b$ -quarks in its final state (inclusive  $\sigma(t\bar{t}Z) = 0.95 \pm 0.08_{\text{stat}} \pm 0.10_{\text{syst}}$  pb at  $\sqrt{s} = 13$  TeV [2]) and can easily mimic the  $tWZ$  signal process, for instance, by one of its  $b$ -jets getting missed during detection.  $ZZ$  contains four leptons and zero  $b$ -quarks in its final state (inclusive  $\sigma(ZZ) = 14.6^{+1.9}_{-1.8}(\text{stat})^{+0.5}_{-0.3}(\text{syst}) \pm 0.2(\text{theo}) \pm 0.4(\text{lumi})$  pb at  $\sqrt{s} = 13$  TeV [54]). One way in which  $ZZ$  can mimic the  $tWZ$  signal process is by reconstruction of a non-prompt  $b$ -jet.

## 2.2.2 Comparison to Trilepton Channel

The most apparent difference between the tri and tetralepton channels is the amount of statistics present, with the tetralepton channel having far less events in its phase space than that of the tri-lepton channel. The lack of statistics in the tetralepton channel can be attributed to its low production cross section,  $\sigma_{(tW^\pm Z).Br(4\ell)}^{\text{NLO}} = 0.7$  fb [24]. The tri-lepton channel has a production cross section ( $\sigma_{(tW^\pm Z).Br(3\ell)}^{\text{NLO}} = 3.9$  fb [24]) around a factor of 4 larger than that of the tetralepton channel. This difference between the production cross section of the two decay channels can be largely attributed to the difference in branching ratios ( $\frac{\Gamma_i}{\Gamma}$ ) between a hadronically decaying  $W$

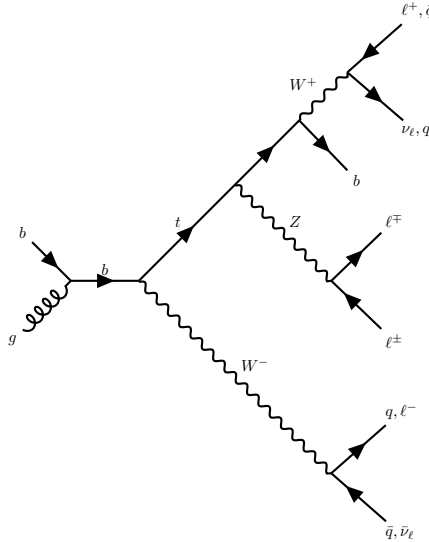


Figure 2.4: Example Feynman diagram of  $tWZ$  production in the tri-lepton channel.

202 boson,  $\frac{\Gamma_{W \rightarrow had}}{\Gamma_W} = (67.41 \pm 0.27)\%$  [47], present in the tri-lepton channel and a leptonically decaying  $W$  boson,  
 203  $\frac{\Gamma_{W \rightarrow \ell\nu}}{\Gamma_W} = (10.86 \pm 0.09)\%$  [47], present in the tetralepton channel.

204  
 205 Despite the tetralepton channel's low statistics, it is not subject to the large  $WZ$  background present in the trilepton  
 206 channel [80]. The tetralepton channel has a relatively large  $ZZ$  background (not present in the trilepton channel),  
 207 fortunately this can be easily suppressed due to the full reconstructability of the two leptonically decaying  $Z$ -bosons.

### 208 2.2.3 Motivation for the search for $tWZ$ production in the tetralepton channel

209 The recent lack of signs of new physics from LHC data [73] tells us that new physics is either very heavy, or is  
 210 very weakly coupled to SM particles. We therefore might only observe signs of new physics in anomalous rates of  
 211 well-chosen processes.  $tWZ$  is a prime example of such a process. It has an extremely low production cross section  
 212 (0.7 fb for  $\sqrt{s} = 13$  TeV [24]), and has subsequently never been observed by any particle physics experiment. Since  
 213  $tWZ$  involves a charged  $W$  boson and neutral  $Z$  boson, its cross section is sensitive to the charged and neutral  
 214 couplings to the top quark. In turn, the top quark is strongly coupled to the Higgs boson, due to its large mass.  
 215 In the SM Lagrangian, the top quark causes the Higgs boson mass to diverge to the Planck scale [32]. Many BSM  
 216 theories aim to get rid of this Higgs mass divergence to the Planck scale.  $tWZ$  is therefore an important process  
 217 in the search for signs of new physics and BSM physics.

218 Standard Model Effective Field Theory (SMEFT) [25] is such a BSM theory which is sensitive to  $tWZ$  produc-  
 219 tion [56, 62]. SMEFT attempts to describe physics at large energy scales which we have not yet been able to  
 220 probe experimentally. SMEFT inherits the same QFT framework as the SM, and adds Lagrangian terms to the  
 221 SM Lagrangian which describe the interactions of SM particles at higher energy scales. Analogous to the coupling  
 222 constants found in the SM Lagrangian, which indicate the interaction strengths between different particles, SMEFT  
 223 contains scalars which operate in the same way. These scalar coefficients are known as Wilson coefficients. It has  
 224 been shown that the cross section of  $tWZ$  is sensitive to many Wilson coefficients. An experimental constraint on  
 225 the cross section of  $tWZ$  is therefore expected to be impactful on a global fit on all the Wilson coefficients in SMEFT.

227  
 228 Prior to this analysis, only two experimental studies of  $tWZ$  in ATLAS have been done. Both take advantage of  
 229 trilepton channel to search for  $tWZ$  production. The first search utilised,  $36 \text{ fb}^{-1}$  of ATLAS data and an upper  
 230 limit on the cross section of  $tWZ$  was set at a value of  $\approx 6$  times the SM cross section [66]. The second search  
 231 utilised  $139 \text{ fb}^{-1}$  (Full Run 2) of ATLAS data and an expected upper limit on the cross section of  $tWZ$  was set at  
 232 a value of  $\approx 2.6$  times the SM cross section [80]. In Section 4.11.2, the latter analysis will be used in combination  
 233 with this analysis, in order to further increase the sensitivity of  $tWZ$ .

234

# Chapter 3

235

# The ATLAS Experiment and Detector

236

## 3.1 The ATLAS Experiment

237

ATLAS (A Toroidal LHC ApparatuS) is one of two general purpose detectors at CERN (the European Organization for Nuclear Research) near Geneva in Switzerland. These detectors collect data from the collisions provided by the worlds highest energy particle accelerator [26], the Large Hadron Collider (LHC) situated at CERN.

240

In this section, information about the LHC and the ATLAS detector are given. This includes technical aspects of the ATLAS detector and the processing of data into meaningful physics objects to be used in analyses. The following chapter consists of information from "The LHC Design Report" [26], "LHC Machine" [43] and "The ATLAS Experiment at the CERN Large Hadron Collider" [36] unless otherwise stated.

245

### 3.1.1 Large Hadron Collider (LHC)

246

The LHC is a circular 27 km particle accelerator located in an underground tunnel on the border between France and Switzerland. The accelerator consists of supercooled, superconducting magnets which accelerate and collide beams of protons at centre-of-mass energies up to  $\sqrt{s} = 13$  TeV at instantaneous luminosities of  $\mathcal{L} \sim 10^{34} \text{ cm}^{-2}\text{s}^{-1}$ . The LHC mainly produces these  $pp$  collisions, however heavy-ion collisions can be produced (typically lasting a month, annually) which reach centre-of-mass energies of  $\sqrt{s} = 5.02$  TeV/nucleon at instantaneous luminosities of  $\mathcal{L} \sim 10^{27} \text{ cm}^{-2}\text{s}^{-1}$ .  $pp$  beams consist of bunches of protons which collide every 25 ns, corresponding to a frequency of 40 MHz.

252

Several accelerator systems are used to accelerate protons and heavy ions to such high energies. Protons are extracted from a tank of ionised hydrogen gas and are injected into the Linear Accelerator 2 (LINAC), where they are linearly accelerated to momenta of 50 MeV. The proton bunches are then sequentially accelerated by a chain of circular accelerators. The chain starts with the Booster which accelerates the protons to momenta of up to 1.4 GeV. The proton bunches are then fed through to the Proton Synchrotron (PS) and the Super Proton Synchrotron (SPS) which accelerate the protons to momenta of up to 25 GeV and 450 GeV respectively. The protons are then transferred to two beam pipes of the LHC where they travel in opposite directions. Both proton beams are accelerated to their final momenta of 6.5 TeV, resulting in a centre-of-mass energy of 13 TeV. These proton beams then collide at one of the four main interaction points situated along the LHC.

262

The four main experiments located at the interaction points are ATLAS, the Compact Muon Solenoid (CMS), Large Hadron Collider Beauty (LHCb) Experiment and A Large Ion Collider Experiment (ALICE). ATLAS and CMS are general-purpose detectors which investigate a wide range of physics processes. Since both ATLAS and CMS can measure the same processes, they are able to cross-check and validate measurements taken by one another. LHCb is specifically designed to study decays of particles containing  $b$ -quarks. ALICE is designed to study the strongly interacting quark-gluon plasma which is formed at extremely high energy densities.

269

At the interaction points, the two proton beams which consist of protons in closely packed bunches, travel in opposite directions to one another and collide. We are only able to study one  $pp$  collision (event) at a time, however many hard  $pp$  collisions can occur per bunch crossing. These additional collisions are referred to as *pile-up*. Pileup complicates the reconstruction of the particles originating from the hard collision of interest.

274 **3.1.1.1 Luminosity**

275 This section consists of information from "Modern Particle Physics" [74], unless otherwise stated.

276  
277 The event production rate at the LHC,  $R(t)$ , for a certain process of interest is given by,

$$R(t) = \mathcal{L}(t)\sigma \quad (3.1)$$

278 where  $\mathcal{L}(t)$  is the instantaneous luminosity and  $\sigma$  and is the cross section of the process of interest. The instantaneous  
279 luminosity,  $\mathcal{L}(t)$ , is independent on the process of interest, and depends on various collider and beam parameters.  
280  $\mathcal{L}(t)$  can be written in terms of these parameters as,

$$\mathcal{L}(t) = f \frac{N n_1 n_2}{4\pi \sigma_x \sigma_y} \quad (3.2)$$

281 where  $f$  is the beam revolution frequency,  $N$  is the number of proton bunches colliding per second,  $n_1$  and  $n_2$  are the  
282 number of protons in the colliding bunches,  $\sigma_x$  and  $\sigma_y$  are the beam spread in the  $x$  and  $y$  directions respectively.  
283 The total integrated luminosity,  $L$ , across some time interval, is given by,

$$L = \int \mathcal{L} dt. \quad (3.3)$$

284 The units of  $L$  are inverse area, and are given by  $\text{fb}^{-1}$  at the LHC and the ATLAS detector.

285  
286 In Figure 3.1, the total integrated luminosity delivered to ATLAS, recorded by ATLAS, and certified to be good  
287 enough for physics analyses (the data passes certain quality control criteria) for  $\sqrt{s} = 13$  TeV  $pp$  collisions at the  
288 LHC is shown [76].

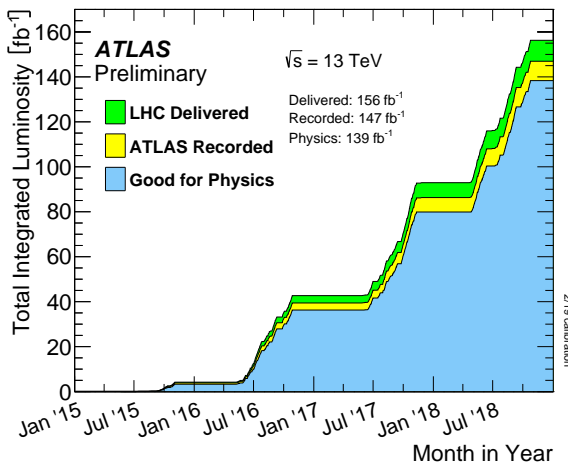


Figure 3.1: The total integrated luminosity delivered to ATLAS, recorded by ATLAS, and certified to be good enough for physics analyses (the data passes certain quality control criteria) for  $\sqrt{s} = 13$  TeV  $pp$  collisions at the LHC is shown [76]. The total integrated luminosity delivered by the LHC, recorded by ATLAS and certified to be good quality data are shown by the green, yellow and blue histograms respectively. The month and year of data taking is shown on the x-axis and the total integrated luminosity (in  $\text{fb}^{-1}$ ) is shown on the y-axis.

289 A total integrated luminosity of  $139 \text{ fb}^{-1}$  of data certified as good for physics was recorded by ATLAS between  
290 2015 and 2018. This data taking period is referred to as Run 2, since it proceeds the Run 1 data taking period  
291 (2011 and 2012) and the Long Shutdown 1 LHC upgrade period (2013 and 2014). In this analysis, we use the Full  
292 Run 2 dataset.

293 **3.2 The ATLAS Detector**

294 The ATLAS detector is a general purpose particle detector, located at one of the four interaction points along the  
295 LHC beam pipe (100 m below ground). In Figure 3.2, the schematic of the ATLAS detector, is shown.

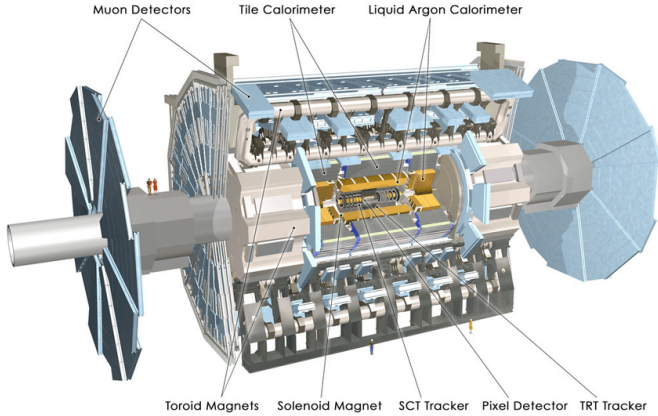


Figure 3.2: Schematic of the ATLAS detector [36]

296 The detector is cylindrically shaped which covers close to  $4\pi$  in solid angle. It has a length of 44 m, a diameter of  
 297 25 m and a mass of 7000 tons. ATLAS consists of four main sub-detectors arranged in concentric cylindrical layers  
 298 around the beam pipe. These include the inner detector, the electromagnetic calorimeter, the hadronic calorimeters  
 299 and the muon spectrometer. The sub-detectors record the momenta, energies and trajectories of different particles  
 300 produced in the collider, allowing for the reconstruction and identification of these particles to be used in physics  
 301 analyses.

### 302 3.2.1 Coordinate System and Kinematics

303 The ATLAS detector adopts a right-handed coordinate system. The origin is at the nominal interaction point with  
 304 the beam direction defining the  $z$ -axis. The  $x - y$  plane (or transverse plane) is perpendicular to the beam line,  
 305 with the  $x$ -axis pointing towards the centre of the LHC ring and the  $y$ -axis pointing upwards towards the Earth's  
 306 surface. The azimuthal angle,  $\phi \in [-\pi, \pi]$ , is measured in the transverse plane with respect to the positive  $x$ -axis.  
 307 The polar angle,  $\theta \in [0, \pi]$ , is measured in the  $z - y$  plane with respect to the positive  $y$ -axis. A quantity called  
 308 the pseudorapidity,  $\eta \in [0, \infty]$  is defined as,

$$\eta = -\ln \tan\left(\frac{\theta}{2}\right) \quad (3.4)$$

309  $\eta$  is often used as a measure of the polar angle, instead of  $\theta$ , since the difference in  $\eta$  between two particles,  $\Delta\eta$ , is  
 310 invariant under a Lorentz boost in the  $z$ -direction [77]. The angular distance between two physics objects,  $\Delta R$ ,  
 311 can be written as,

$$\Delta R = \sqrt{(\Delta\phi)^2 + (\Delta\eta)^2} \quad (3.5)$$

312 where  $\Delta\phi$  is the difference in  $\phi$  between the two physics objects of interest. Quantities defined in the transverse  
 313 plane are often used to describe the kinematics of physics objects in hadron collider experiments. The transverse  
 314 momentum,  $p_T$ , is defined as,

$$p_T = \sqrt{(p_x)^2 + (p_y)^2} \quad (3.6)$$

315 where  $p_x$  and  $p_y$  are the  $x$  and  $y$  components of the physics object's momenta, respectively. The transverse energy,  
 316  $E_T$ , is defined as,

$$E_T = \sqrt{m^2 + p_T^2} \quad (3.7)$$

317 where  $m$  is the invariant mass of the physics object.

### 318 3.2.2 Inner Detector

319 The inner detector is the first layer of concentric cylindrical sub-detector layers in the ATLAS detector. It is used  
 320 to identify charged particles and reconstruct the trajectories of charged particles produced in the collisions via  
 321 energy deposition in semiconductor material (hits) and the ionisation of gas. It consists of three complementary

322 sub-detectors (in order from nearest to farthest from the beam pipe): the Pixel Detector, the Semiconductor Tracker  
 323 (SCT) and the Transition Radiation Detector (TRT). The Pixel Detector and SCT are based on semiconductor  
 324 technology and have the highest granularity of any sub-detector in ATLAS, in order to cope with the high frequency  
 325 of collisions near the interaction point. The TRT consists of drift tubes (straws) containing a mixture of gas (70%  
 326 Xe, 27% CO<sub>2</sub> and 3% O<sub>2</sub>), which allows measurement of the energy deposited by charged particles through the  
 327 ionisation of the gas. Solenoid magnets surround the inner detector and bend the trajectories of charged particles.  
 328 The charges and momenta of particles can be inferred from their bent trajectories, which are reconstructed by the  
 329 hits produced via energy deposition in the Inner Detector.

### 330 3.2.3 Electromagnetic and Hadronic Calorimeters

331 The Electromagnetic Calorimeter (ECAL) and Hadronic Calorimeter (HCAL) surround the Inner Detector, with  
 332 the ECAL nearer to the beam line. The ECAL and HCAL provide accurate measurements of the energy of particles  
 333 which interact electromagnetically (e.g. photons and electrons) and hadronically (e.g. jets), respectively. Particles  
 334 entering the calorimeters interact with the detector material and create either a electromagnetic shower (in the  
 335 ECAL) or a hadronic shower (in the HCAL), depositing all their energy in the calorimeter cells. The calorimeters  
 336 consist of an active material and a passive absorber material. Active materials are used to measure the energy  
 337 deposited by the particles and passive absorber materials induce the electromagnetic and hadronic showers. The  
 338 ECAL uses liquid argon (LAr) as its active material and lead as its absorber material. The HCAL uses alternating  
 339 steel absorber layers and plastic scintillating tile layers as its active material. The primary mechanism of energy  
 340 deposition in the ECAL is through bremsstrahlung (for electrons) and pair production (photons). Hadrons usually  
 341 deposit a small amount of their energy in the ECAL, and interact via inelastic scattering with the nuclei of the  
 342 detector material. The hadronic showers (jets) produced in these nuclear interactions travel much further than an  
 343 electromagnetic shower, and for that reason, the volume of the HCAL is designed to occupy a much larger space  
 344 than that of the ECAL.

### 345 3.2.4 Muon Spectrometer

346 The Muon Spectrometer (MS) is the outermost sub-detector of ATLAS and surrounds the HCAL. Muons traverse  
 347 through the inner detector and calorimeters, with minimal energy loss, before reaching the MS. The MS consists  
 348 of trigger and high-precision tracking systems. Large superconducting toroid shaped magnets deflect the incoming  
 349 muons to measure their trajectories and subsequently their momenta via the curvature of the trajectories. The MS  
 350 measures muon trajectories as they ionize gas (filled with Ar and CO<sub>2</sub> gas) in the MS drift chambers.

### 351 3.2.5 Trigger and Data Acquisition System

352 The Trigger and Data Acquisition System (TDAQ) manages and handles the large amount of data produced within  
 353 the ATLAS detector. In Run 2,  $pp$  bunch crossings occur every 25 ns, corresponding to an event rate of 40 MHz.  
 354 The TDAQ system performs a fast preliminary reconstruction to select events with signatures which are interesting  
 355 for physics analyses. The information collected from these events are permanently stored for offline reconstruction  
 356 and analysis, and the rest (the vast majority of events) are discarded. The trigger system reduces the 40 MHz data  
 357 rate to around 1 kHz.

### 358 3.2.6 Particle Identification and Object Reconstruction

359 Particles originating from  $pp$  collisions, or from their subsequent decays, traverse through the ATLAS detector and  
 360 interact with its different sub-detectors, producing characteristic electronic signals. These signals are then processed  
 361 by various algorithms to reconstruct and identify the physics objects (e.g. electrons, muons, jets) in the event. This  
 362 section outlines the procedures used to define these physics objects.

#### 363 3.2.6.1 Tracks and primary vertices

364 The trajectories of charged particles, or tracks, are reconstructed in the ID. First, energy is deposited by charged  
 365 particles (hits) in pixels or strips, in the Pixel and SCT detectors respectively. Adjacent pixels or strips are grouped  
 366 together in *energy clusters*. Energy clusters define 3D space-points indicating the location where the charged  
 367 particle traversed. Track seeds are then defined as sets of three space-points, in either the Pixel or SCT detectors.  
 368 A Kalman filter [9] is then used to build track candidates from the track seeds. Often, multiple track candidates

are built per track seed, therefore an ambiguity solver [34] is needed for finding the track which best represents the traversal of the charged particle. The ambiguity solver ranks each track from a given seed based on, the number of associated hits, the number of holes (expected hits which are absent), track momenta and the  $\chi^2$  of the track fit. Low ranked tracks are then discarded. High ranked tracks are refitted, introducing information from the TRT.

The primary vertex is the location of the  $pp$  collision of interest (i.e. from the hard scatter). The primary vertex from the hard scatter needs to be identified, to isolate the event of interest from unwanted pile-up events. In the event reconstruction procedure [61], the primary vertex is defined as the vertex of the event with the largest sum of  $(p_T)^2$  (corresponding to the measured  $(p_T)^2$  of the particle from its reconstructed track) of its associated tracks. Furthermore, the primary vertex is required to have at least two associated tracks. To reduce contamination from fake tracks used in primary vertex reconstruction, only tracks which pass certain tight selection criteria are used in the reconstruction procedure. An iterative fitting procedure is then used to reconstruct the primary vertex. The best vertex position is fitted from the reconstructed tracks and a selected seed position. In each iteration, the less compatible tracks are down-weighted and the next best vertex position is recomputed. All incompatible tracks are then removed and the fitting procedure is repeated until all tracks have a corresponding vertex or no additional vertices can be found with the remaining set of tracks.

### 3.2.6.2 Electrons

Since electrons are charged particles, they give rise to tracks in the Inner Detector and deposit energy in the ECAL via electromagnetic showering. Electrons are therefore reconstructed and identified from signals in the Inner Detector and ECAL. Electrons are reconstructed using a dynamic clustering algorithm [1] which matches electron candidate tracks in the Inner Detector to energy clusters in the ECAL. First, energy clusters which have local maxima are identified using a sliding window algorithm [6]. Tracks are then matched to the energy clusters, forming electron candidates for each energy cluster. Often, many electron candidates are found. Electron candidates are ranked based on the  $\Delta R$  between the track and energy cluster, and the number of Pixel Detector hits and holes. The electron candidate with the highest rank is chosen as the electron track.

A likelihood discriminant is used to identify electrons. Quantities measured in the Inner Detector and ECAL are used as input, such that they discriminate well between prompt isolated electrons and other physics objects (e.g. jets, electron from a photon conversion, electron from a semi-leptonically decaying hadron). Important input variables include the shape of the electromagnetic shower, track quality in the Inner Detector and information from the TRT. Three working points (*loose*, *medium*, *tight*) are defined, based on different cuts on the output of the likelihood discriminant. The *loose* working point has the weakest background rejection power (higher efficiency), whereas the *tight* working point has the strongest background rejection power (lower efficiency).

### 3.2.6.3 Muons

Muons leave tracks in the Inner Detector and the MS. They traverse the ECAL and HCAL with no significant energy loss. Muons are therefore reconstructed and identified from information in the Inner Detector and MS. Tracks are reconstructed [5] in the Inner Detector and MS independently. Both tracks are combined, using a global  $\chi^2$  fit, resulting in reconstructed muon candidates.

Similar to electron identification, muons use a likelihood discriminant to identify prompt muons and suppress background contamination (mainly from pion and kaon decays). Four working points are defined to cover needs of different physics analyses: *loose*, *medium*, *tight* and *high- $p_T$*  [5].

### 3.2.6.4 Jets and $b$ -tagging

Due to colour confinement, free quarks and gluons cannot exist. Therefore, coloured particles emerging from the interaction point result in collimated streams of colourless particles, known as jets. Jets deposit energy in the Inner Detector and in the HCAL. Jets in ATLAS are reconstructed from topological clusters using the anti- $k_t$  algorithm [27]. Topological clusters are groups of adjacent calorimeter cells which originate from *seed* cells. Seed cells are defined to contain at least 4 times the average amount of noise expected in the cell<sup>1</sup>. All cells adjacent to the seed cell are grouped together given that the energy deposited within the cell is at least  $2\sigma$ . This process is repeated until there are no adjacent cells which meet the above criteria. All adjacent cells to the cluster are then

<sup>1</sup> $\sigma$ : average noise in a given cell

<sup>419</sup> added, with no requirement on the energy deposited within these cells.

<sup>420</sup> Different tagging algorithms are used to identify the quark flavour which initiated a jet.  $b$ -quark tagging is used  
<sup>421</sup> extensively in top physics, due to the  $b$ -quark present in the top quark's dominant decay channel (See Table 2.1).  
<sup>422</sup> Hadrons arising from  $b$ -quark hadronisation have mean lifetimes  $\sim 1.5$  ps and travel (on average) a few mil-  
<sup>423</sup> limetres before decaying. This creates a secondary vertex within the jet (See Figure 3.3). This characteristic decay  
<sup>424</sup> signature, along with several other unique features of  $b$ -jets, are exploited in  $b$ -tagging algorithms to distinguish  
<sup>425</sup>  $b$ -jets from  $c$ - or light flavour jets. In Figure 3.3, an illustration of the production of a  $b$ -jet, is shown.

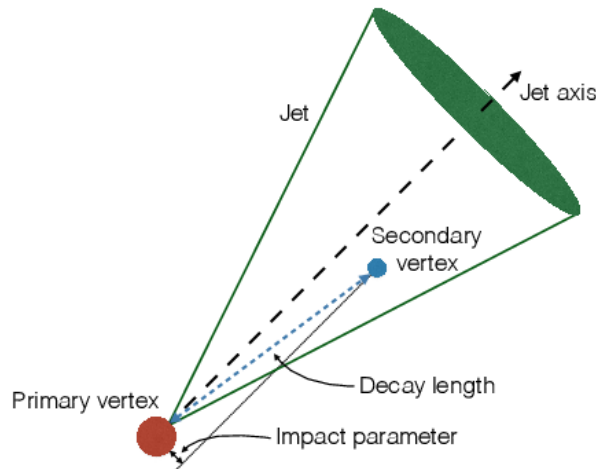


Figure 3.3: An illustration [37] of the production of a  $b$ -jet is shown. This illustrates the presence of a secondary vertex within a  $b$ -jet.

<sup>427</sup> In this analysis, we use the recommended DL1r (Deep-Learning Flavour Tagger) tagging algorithm [17]. The DL1r  
<sup>428</sup> algorithm combines outputs from several low-level tagging algorithms using a Deep Neural Network and outputs  
<sup>429</sup> the probability that a given input jet is identified as a  $b$ ,  $c$  or light flavoured jet.

430

# Chapter 4

431

# Analysis Setup and Strategy

## 432 4.1 Data and Monte Carlo Simulation

### 433 4.1.1 Data Samples

434 The  $pp$  collision data used in this analysis was collected with the ATLAS detector at the LHC from 2015 to 2018. This  
 435 data period of data taking is referred to as Run 2. During this period,  $pp$  collisions at  $\sqrt{s} = 13$  TeV, corresponding  
 436 to an integrated luminosity ( $\mathcal{L}$ ) of  $156 \text{ fb}^{-1}$ , were delivered by the LHC. The ATLAS detector managed to record  
 437  $147 \text{ fb}^{-1}$  of this total delivered data.  $139 \text{ fb}^{-1}$  of the data recorded by ATLAS is considered to be good enough for  
 438 physics analyses (the data passes certain quality control criteria) and placed into the *Good Runs List* [46]. We use  
 439 the Run 2 datasets from the Good Runs List, called `mc16a`, `mc16d` and `mc16e` with integrated luminosity's of  $36.2$   
 440  $\text{fb}^{-1}$ ,  $44.3 \text{ fb}^{-1}$  and  $58.5 \text{ fb}^{-1}$  respectively.

### 441 4.1.2 Monte Carlo Samples

442 Simulated Monte Carlo (MC) samples were generated and used to model the SM  $tWZ$  signal and its backgrounds.  
 443

444 The following background processes are considered:

- 445 • **t $\bar{t}Z$ :**  $t\bar{t}$  with an associated  $Z$ -boson, in the tetralepton final state. Therefore, both top-quarks decay leptonically  
 446 (e.g.  $t \rightarrow W^+ b \rightarrow \ell^+ \nu b$ ) and of these top-quarks emits a  $Z$ -boson which decays leptonically ( $Z \rightarrow \ell^\pm \ell^\mp$   
 447 (OSSF lepton pair)). This results in a final state with 4 leptons and 2 b-quarks.
- 448 • **ZZ:** Diboson production with a tetralepton final state, therefore both  $Z$ -bosons decay leptonically ( $Z \rightarrow \ell^\pm \ell^\mp$   
 449 (OSSF lepton pair)).
- 450 • **other:** Processes with a relatively minimal, but non-negligible background contribution

- 451    -  $VVV (V = W/Z)$
- 452    -  $t\bar{t}$
- 453    -  $t\bar{t}W$
- 454    -  $t\bar{t}WW$
- 455    -  $t\bar{t}H$
- 456    -  $WZ$
- 457    -  $t\bar{t}t$
- 458    -  $t\bar{t}t\bar{t}$
- 459    -  $tZq$

460 The MC simulations are achieved via the use of event generators and parton shower generators. Event generators  
 461 simulate the  $pp$  collisions (hard events) by sampling the proton's Parton Distribution Functions (PDFs) at the  
 462 desired energy scale. The parton shower generators simulate any incoming or outgoing particles from the hard  
 463 process, which carry QCD color charge and can therefore lead to parton showers.

464

465 The production of  $tWZ$  events is simulated with the `MADGRAPH5_AMC@NLO 2.3.3` generator providing matrix  
 466 element (ME) calculations at NLO. The events are interfaced with `PYTHIA 8.235` for the parton shower.

467

468 The production of  $t\bar{t}Z$  and  $t\bar{t}W$  events are simulated with the `MADGRAPH5_AMC@NLO 2.3.3` generator providing ME  
 469 calculations at NLO. The events are interfaced with `PYTHIA 8.210` for the parton shower.

470

471 Event generation of  $tWZ$  and  $t\bar{t}Z$  results in diagrams which overlap with one another, that is, these diagrams  
 472 contain the same initial and final state particles. Several methods exist in order to separate between the two  
 473 processes, by removing the overlap, therefore avoiding double counting. There are two different diagram removal  
 474 procedures, diagram removal procedure 1 (DR1) [39] and diagram removal procedure 2. We use the DR1 scheme  
 475 to remove the overlap (interference) between  $tWZ$  and  $t\bar{t}Z$ .

476

477 Diboson processes which feature the three charged leptons and one neutrino or four charged lepton in their final  
 478 states, such as  $WZ$  and  $ZZ$ , are simulated using `SHERPA 2.2.2` at NLO precision. The events are interfaced with  
 479 `SHERPA` for the parton shower.

480

481 Fully leptonic triboson processes such as  $WWW$ ,  $WWZ$ ,  $WZZ$ , and  $ZZZ$  containing up to six leptons in their final  
 482 states are simulated using `SHERPA 2.2.2` at NLO precision. The events are interfaced with `SHERPA` for the  
 483 parton shower.

484

485 The production of  $t\bar{t}$  events are simulated with the `POWHEG` generator providing ME calculations at NLO. The  
 486 events are interfaced with `PYTHIA 8.210` for the parton shower.

487

488 The production of  $t\bar{t}t$ ,  $t\bar{t}\bar{t}$  and  $t\bar{t}WW$  are simulated using the `MADGRAPH5_AMC@NLO 2.2.2` generator at LO  
 489 precision. The events are interfaced with `PYTHIA 8.186` for the parton shower.

490

491 The production of  $t\bar{t}$  with an associated Higgs boson,  $t\bar{t}H$ , are generated using the `MADGRAPH5_AMC@NLO 2.6.0`  
 492 generator at NLO precision. The events are showered using `PYTHIA 8.230`.

493

494 The production of  $t\bar{t}$  events is simulated with the `POWHEG` generator providing ME calcualtions at NLO. The events  
 495 are showered using `PYTHIA 8.230`.

496

497 The production of a single top quark in association with a  $Z$ -boson and an extra parton,  $tZq$ , is simulated using  
 498 `MADGRAPH5_AMC@NLO 2.3.3` at NLO prescision. The events are interfaced with `PYTHIA 8.230` for the parton shower.

499

500 In Table 4.1, the event generator and parton shower used for each process's sample are shown.

Process	Event Generator	Cross section calculation	Parton Shower
$tWZ$	<code>MADGRAPH5_AMC@NLO 2.3.3</code>	NLO	<code>PYTHIA 8.235</code>
$t\bar{t}Z$	<code>MADGRAPH5_AMC@NLO 2.3.3</code>	NLO	<code>PYTHIA 8.210</code>
$ZZ, WZ$	<code>SHERPA 2.2.2</code>	NLO	<code>SHERPA</code>
$VVV (V = W/Z)$	<code>SHERPA 2.2.2</code>	NLO	<code>SHERPA</code>
$t\bar{t}$	<code>POWHEG</code>	NLO	<code>PYTHIA 8.230</code>
$t\bar{t}W$	<code>MADGRAPH5_AMC@NLO 2.3.3</code>	NLO	<code>PYTHIA 8.210</code>
$t\bar{t}WW$	<code>MADGRAPH5_AMC@NLO 2.2.2</code>	LO	<code>PYTHIA 8.186</code>
$t\bar{t}H$	<code>MADGRAPH5_AMC@NLO 2.6.0</code>	NLO	<code>PYTHIA 8.230</code>
$t\bar{t}t, t\bar{t}\bar{t}$	<code>MADGRAPH5_AMC@NLO 2.2.2</code>	LO	<code>PYTHIA 8.186</code>
$tZq$	<code>MADGRAPH5_AMC@NLO 2.3.3</code>	NLO	<code>PYTHIA 8.230</code>

Table 4.1: The event generator and parton shower used for the signal and background process's MC samples is shown.

## 501 4.2 Objects

502 In this section the physics objects (leptons, jets and  $b$ -tagged jets) used in this analysis are outlined.

### 503 4.2.1 Leptons

504 In this analysis we only consider  $e$  and  $\mu$  leptons, since  $\tau$  leptons are difficult to detect in the ATLAS detector.  
 505  $\tau$  leptons are challenging to detect since they have an extremely short lifetime ( $290.3 \pm 0.5$  fs [47]) which causes  
 506 them to decay before reaching any detector components and therefore can only be reconstructed via their decay  
 507 products.

508  
 509 In addition to our selection criteria of exactly four leptons, we require that the Leading (L), Next-to-Leading (NL),  
 510 Next-to-Next-to-Leading (NNL) and Next-to-Next-to-Next-to-Leading (NNNL) leptons have  $p_T$  greater than 28,  
 511 18, 10 and 10 GeV respectively. Here we have chosen to apply relatively loose object-level cuts in an attempt to  
 512 maximize our signal statistics, since the analysis is heavily statistically limited.

513  
 514 Reconstructed electrons are required to be within  $|\eta| < 2.47$  and excluding the transition region between the barrel  
 515 and end-cap calorimeters at  $1.37 < |\eta| < 1.52$ . Reconstructed muons are required to be within  $|\eta| < 2.5$ .

516  
 517 The transverse impact parameter,  $d_0$ , is defined as the minimal spacial distance between the object's (here we  
 518 are referring to leptons) trajectory and the primary vertex (the vertex associated with the  $p$ - $p$  hard scatter).  
 519 The longitudinal impact parameter,  $z_0$ , is defined as the value of  $z$  of the point on the object's trajectory which  
 520 determines  $d_0$ . To ensure consistency between the lepton and the primary vertex, we require that  $|\frac{d_0}{\sigma(d_0)}| < 5$ ,  
 521  $|z_0 \sin \theta| < 0.5$  mm for electrons and  $|\frac{d_0}{\sigma(d_0)}| < 3$ ,  $|z_0 \sin \theta| < 0.5$  mm for muons, following the current recommenda-  
 522 tions [75].

523  
 524 To avoid instances where one detector signal can result in multiple different reconstructed objects, an overlap  
 525 removal is applied which ignores all but one of these objects. We use the current recommended configuration [45].

526  
 527 Electrons are selected using a likelihood based discriminant [1] which takes measurements from the tracking  
 528 system, calorimeter system and quantities derived from both the tracking and calorimeter system as input. Muons  
 529 are selected using AnalysisBase's Muon Selection Tool [65].

530  
 531 Loose electrons are defined with the criteria above, using the `LooseAndBLayerLH` ( $\sim 91\%$  selection efficiency for  
 532 electrons with  $E_T > 30$  GeV [40]) identification working point. Similarly, tight electrons are defined with the  
 533 criteria above, using the `TightLH` ( $\sim 80\%$  selection efficiency for electrons with  $E_T > 30$  GeV [40]) identification  
 534 working point. Both loose and tight muons use the `Medium` ( $\sim 95\%$  selection efficiency [5]) identification working  
 535 point.

536  
 537 Tight leptons additionally require that they are sufficiently isolated from other particles produced in the collision.  
 538 This is done by defining a cone of radius  $\Delta R = \sqrt{\Delta\eta^2 + \Delta\phi^2}$  around the particle of interest and summing the  $p_T$   
 539 of all the reconstructed particles surrounding the particle of interest, situated within the cone. A quantity,  $I_{rel}$ , is  
 540 then defined as  $I_{rel} = \frac{\sum p_T(\text{surrounding candidate})}{p_T(\text{candidate})}$ , the ratio of this sum to the  $p_T$  of the lepton candidate. If this value  
 541 is large, it is likely that the particle of interest originated from a jet (together with many other particles), whereas  
 542 a prompt decay product resulting from the hard scatter will have little to no energy surrounding it ( $I_{rel} \ll 1$ ).  
 543 We use Analysis Base's `IsolationSelectionTool` with the `PLVTight` ( $\sim 70\%$  efficiency [7]) and `PLVTight` ( $\sim$   
 544 70% efficiency at  $p_T = 30$  GeV [33]) working points for tight electrons and tight muons respectively (following the  
 545 current recommendations [69]).

546  
 547 In Table 4.2, a summary of the selection criteria for leptons is shown.

### 548 4.2.2 Jets

549 Jets are reconstructed using the anti- $k_t$  algorithm (See Section 3.2.6.4). We use the `AntiKt4EMPFlowjets` ( $\sim$   
 550 97% average efficiency with JVT (outlined in the subsequent paragraph)  $> 0.2$  [75]) working point (following the  
 551 current recommendations [75]).

552  
 553 The jet-vertex-tagger (JVT) and the forward jet-vertex-tagger (fJVT) are likelihood discriminant which aim  
 554 to suppress pile-up jets. We use the `Medium` working point for the JVT and the fJVT (following the current  
 555 recommendations [68]). We additionally require that jets have a JVT value greater than 0.5.

	Electrons		Muons	
	Tight	Loose	Tight	Loose
$p_T$ cuts	$p_T(\ell_1, \ell_2, \ell_3, \ell_4) > (28, 18, 10, 10)$ GeV "recommended"			
Overlap Removal				
$\eta$ cuts	$ \eta(\ell_e)  < 2.47$ excluding $1.37 <  \eta(\ell_e)  < 1.52$		$ \eta(\ell_\mu)  < 2.5$	
Impact Parameters	$ \frac{d_0}{\sigma(d_0)}  < 5$ , $ z_0 \sin \theta  < 0.5$ mm		$ \frac{d_0}{\sigma(d_0)}  < 3$ , $ z_0 \sin \theta  < 0.5$ mm	
Identification WP	TightLH	LooseAndBLayerLH	Medium	Medium
Isolation WP	PLVTight	Not Used	PLVTight	Not Used

Table 4.2: A summary of the requirements applied for selecting tight and loose leptons ( $e, \mu$ ) is shown.

556  
557 Jets are required to be within  $p_T(\text{jet}) > 20$  GeV. We apply these looser  $p_T$  cuts in an attempt to increase our  
558 limited signal statistics. A forward jet is a signature of single top production, we therefore require jets to have  
559  $|\eta| < 4.5$  in order to include these forward jets.

### 560 4.2.3 $b$ -tagging

561 The DL1r  $b$ -tagger [64] was used to identify jets as  $b$ -jets (See Section 3.2.6.4). We use different DL1r working  
562 points to identify  $b$ -jets in our event selection (See Section 4.4). The working points are defined based off a cut on  
563 the DL1r score corresponding to a  $b$ -jet tagging efficiency of 60%, 70%, 77% and 85%.

564 Since we are heavily statistically limited, we aim to increase the amount of statistics in our regions. In an attempt  
565 to achieve this goal in the  $t\bar{t}Z$  CR,  $b$ -tagged jets were placed under *tight* and *loose* definitions. A tight  $b$ -tagged jet  
566 is defined as a jet which passes the 77%, 70%, 65% or 60% DL1r  $b$ -tagger working point. A loose  $b$ -tagged jet is  
567 defined as a jet which passes 85% DL1r  $b$ -tagger working point, but not the 77%, 70%, 65% or 60% DL1r  $b$ -tagger  
568 working points. Different numbers (and definitions) of tight and loose  $b$ -tagged jets were tried in each region, with  
569 the final selection criteria being chosen which maximised the expected significance of  $\sigma(tWZ)$  (See Section 4.4.1).

## 571 4.3 Kinematic cuts

572 The invariant mass of the OSSF lepton pair coming from the  $Z$  boson must equal the invariant mass of the  $Z$  boson,  
573 and noting that  $e, \mu$  reconstruction and identification in the ATLAS detector has a high efficiency [57], we can use  
574 these OSSF leptons to reconstruct  $Z$  bosons with relatively high confidence. We therefore define a  $Z$  candidate  
575 as an OSSF lepton pair with an invariant mass,  $m_{\text{OSSF}}$ , satisfying the condition,  $|m_{\text{OSSF}} - m_Z| < 30$  GeV, where  
576  $m(Z)$  is the nominal  $Z$  boson mass (91.1876 GeV [47]). We use this wider mass window to cover the full range of  
577 the  $m(Z)$  distribution, in an attempt to increase the number of events which pass our baseline selections. Multiple  
578  $Z$  candidates can be present in certain decay channels (e.g.  $eeee$ ,  $\mu\mu ee$ ,  $\mu\mu\mu\mu$ ). In these cases, the  $Z$  candidate  
579 which has an invariant mass closest to the nominal  $Z$  boson mass is chosen.

580 In order to suppress potential fakes and quarkonia (low mass resonances such as  $J/\psi$  and upsilon) we require that  
581 all OSSF lepton pairs have an invariant mass,  $m_{\text{OSSF}}$ , greater than 10 GeV.

583  
584 The final state lepton charges must sum to zero. We therefore require,  $\sum_{i=1}^4 \text{charge}(\ell_i) = 0$ .

## 585 4.4 Regions and Event Selection

586 We define two  $tWZ$  SRs, as opposed to one  $tWZ$  SR, in an attempt to suppress and constrain the  $ZZ$  background.  
587 We require that both  $tWZ$  SRs have exactly four tight leptons, exactly one  $Z$ -boson candidate, exactly one tight  
588  $b$ -tagged jet (from the decay of the top quark) and greater than or equal to one jet. The two  $tWZ$  SR's differ  
589 by the flavours of their leptons which don't originate from the decay of a  $Z$ -boson (Non- $Z$  leptons). The  $ZZ$   
590 background has two  $Z$ -bosons which decay into a pair of OSSF lepton pairs, in order to mimic the  $tWZ$  signal.

Baseline selections				
$N_\ell = 4$ $p_T(\ell_1, \ell_2, \ell_3, \ell_4) > (28, 10, 10, 10)$ GeV $p_T(\text{jet}) > 20$ GeV, $ \eta(\text{jet})  < 4.5$ , $\text{jvt} > 0.5$ $ \eta(\ell_e)  < 2.47$ excluding $1.37 <  \eta(\ell_e)  < 1.52$ $ \eta(\ell_\mu)  < 2.5$ $\sum_{i=1}^4 \text{charge}(\ell_i) = 0$ All OSSF lepton pairs require $m_{\text{OSSF}} > 10$ GeV				
Regions				
$tWZ$ OF SR	$tWZ$ SF SR	$t\bar{Z}$ CR	$ZZb$ CR	$(tWZ)_{\text{fake}}$ CR
$N_\ell(\text{tight}) = 4$	$N_\ell(\text{tight}) = 4$	$N_\ell(\text{tight}) = 4$	$N_\ell(\text{tight}) = 4$	$N_\ell(\text{tight}) = 3$ $N_\ell(\text{loose and NOT tight}) = 1$
$N_Z$ candidate = 1	$N_Z$ candidate = 1	$N_Z$ candidate = 1	$N_Z$ candidate = 2	$N_Z$ candidate = 1
$N_{\text{jet}} \geq 1$	$N_{\text{jet}} \geq 1$	$N_{\text{jet}} \geq 2$	$N_{\text{jet}} \geq 1$	$N_{\text{jet}} \geq 1$
$N_{\text{b-jet}}(\text{tight}) = 1$	$N_{\text{b-jet}}(\text{tight}) = 1$	$N_{\text{b-jet}}(\text{tight}) \geq 1$ $N_{\text{b-jet}}(\text{loose}) \geq 0$ $N_{\text{b-jet}}(\text{tight}) + N_{\text{b-jet}}(\text{loose}) = 2$	$N_{\text{b-jet}}(\text{tight}) = 1$	$N_{\text{b-jet}}(\text{tight}) = 1$
Opp. Flavour Non-Z leptons	Same Flavour Non-Z leptons	-	-	-

Table 4.3: A summary of the requirements applied for selecting events in the signal and control regions is shown.

We take advantage of this to define a  $tWZ$  region rich in  $ZZ$  background and one with a minimal  $ZZ$  background component. This is done by requiring that one of the  $tWZ$  SRs has its two non- $Z$  leptons to have opposite flavour and the other  $tWZ$  SR is required to have its non- $Z$  leptons to have the same flavour. These two disjoint  $tWZ$  SRs are named  $tWZ$  OF SR and  $tWZ$  SF SR respectively. We therefore expect that the  $tWZ$  SF SR contains the majority of  $tWZ$ 's  $ZZ$  background events.

In order to check the modelling of the most dominant background components in our signal region, we have modified our selection criteria to define  $t\bar{Z}$  and  $ZZb$  control regions. The  $t\bar{Z}$  control region has the same requirement on the number of reconstructed  $Z$  boson candidates in the signal region (due to a commonality on the number of  $Z$  bosons present in both processes), however we require at least two jets and that exactly two of these jets are  $b$ -tagged (corresponding to the  $b$ -quark jets originating from the two top-quark decays). We choose to define a  $ZZb$  region, as opposed to a  $ZZ$  region, since the  $ZZ$  background present in the  $tWZ$  signal region contains exactly one  $b$ -tagged jet. Therefore defining a region with  $ZZ$  plus exactly one  $b$ -jet more closely resembles the  $ZZ$  background present in the signal region. In addition to this, mis-modelling of  $ZZ$  has been seen in other analyses [3, 35], further motivating the use of a  $ZZb$  control region over a  $ZZ$  CR. The  $ZZb$  CR requires exactly two  $Z$  boson candidates and exactly one  $b$ -tagged jet, resulting in an implicit requirement on the number of jets ( $N_{\text{jet}} \geq 1$ ).

In order to constrain the fake lepton component contained within the  $t\bar{Z}$  sample, we define a  $(tWZ)_{\text{fake}}$  CR which is as similar as possible to the  $tWZ$  CR but is enhanced in fakes. This is achieved by defining the  $(tWZ)_{\text{fake}}$  CR to inherit the same selection criteria as the  $tWZ$  SRs however, in this case, we require exactly 3 tight leptons and exactly 1 loose (and NOT tight) lepton (since looser leptons are more likely to be fakes, compared to tighter leptons). A  $(t\bar{Z})_{\text{fake}}$  CR (requiring exactly 3 tight leptons and exactly 1 loose (and NOT tight) lepton) was tried as an alternative to the  $(tWZ)_{\text{fake}}$  CR, however a much larger suppression of fakes were observed in this region (compared to the  $(tWZ)_{\text{fake}}$  CR). This suppression of fakes can be explained by the extra  $b$ -tagged jet requirement (exactly two  $b$ -tagged jets are required in the  $t\bar{Z}$  region, compared to exactly one in the  $tWZ$  SRs (See Table 4.3)) which causes suppression of fakes via the overlap removal procedure [45].

In Table 4.3, a summary of the final selection criteria and region definitions is shown.

#### 4.4.1 Optimization studies for event selection

In order to find the selection criteria for jets and leptons which maximized sensitivity to the  $tWZ$  signal, studies were performed by plotting the expected significance ( $Z_\mu^{exp}$ ) and expected upper limit ( $\mu_{up}^{exp}$ ) for different selection

622 criteria. The fitting procedure as described in Section 4.10.1 was used to calculate the expected upper limits and  
 623 expected significances in this study. The same selection criteria and regions defined in Table 4.3 was used (unless  
 624 otherwise specified), except for the selection(s) which were being optimised in each case.

625  
 626 In Figure 4.1 the expected significance ( $Z_\mu^{exp}$ ) and expected upper limits ( $\mu_{up}^{exp}$ ) for different  $\eta(jet)$  cuts are shown.

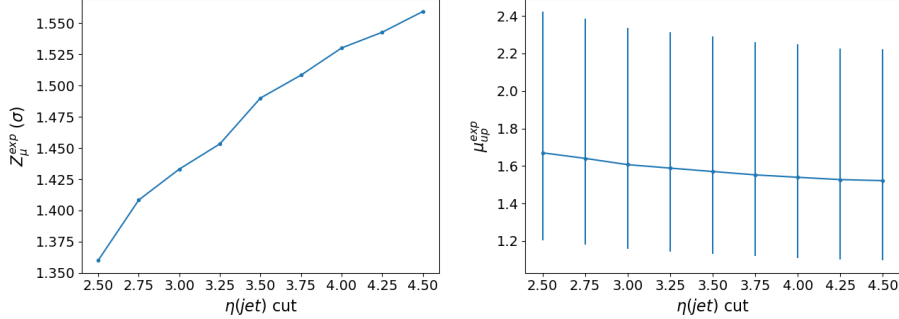


Figure 4.1: **Left:** Expected significance ( $Z_\mu^{exp}$ ) for different  $\eta(jet)$  cuts is shown. The cuts applied on the  $\eta(jet)$  are shown on the x-axis and corresponding expected significance from the likelihood fit is shown on the y-axis.  
**Right:** Expected upper limit ( $\mu_{up}^{exp}$ ) for different  $\eta(jet)$  cuts is shown. The cuts applied on the  $\eta(jet)$  are shown on the x-axis and corresponding expected upper limits are shown on the y-axis. Error bars representing the total uncertainty on the expected upper limits are shown as vertical lines.

627  
 628 From Figure 4.1, we can see that the  $\eta(jet)$  cut which maximises the sensitivity of  $tWZ$  in the tetralepton channel  
 629 is requiring that  $\eta(jet) < 4.5$ . This selection criteria was set for the  $\eta(jet)$  across all regions.

630  
 631 In Figure 4.2 the expected significance ( $Z_\mu^{exp}$ ) and expected upper limits ( $\mu_{up}^{exp}$ ) for different  $p_T(jet)$  cuts are shown.

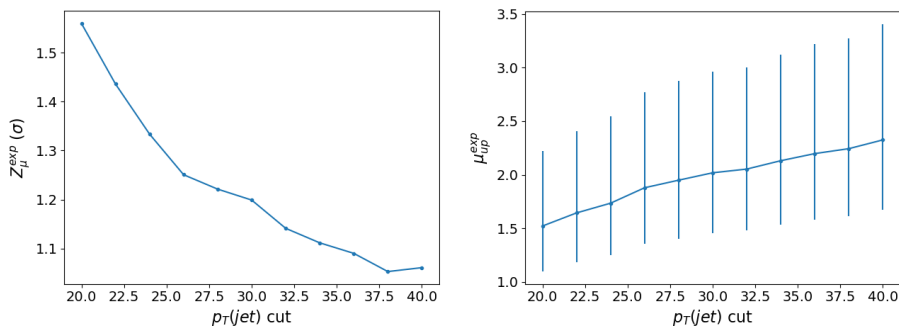


Figure 4.2: **Left:** Expected significance ( $Z_\mu^{exp}$ ) for different  $p_T(jet)$  cuts is shown. The cuts applied on the  $p_T(jet)$  are shown on the x-axis and corresponding expected significance from the likelihood fit is shown on the y-axis.  
**Right:** Expected upper limit ( $\mu_{up}^{exp}$ ) for different  $p_T(jet)$  cuts is shown. The cuts applied on the  $p_T(jet)$  are shown on the x-axis and corresponding expected upper limits are shown on the y-axis. Error bars representing the total uncertainty on the expected upper limits are shown as vertical lines.

632  
 633 From Figure 4.2, we can see that the  $p_T(jet)$  cut which maximises the sensitivity of  $tWZ$  is requiring that  
 634  $p_T(jet) > 20\text{GeV}$ . This selection criteria was set for the  $p_T(jet)$  across all regions.

635  
 636 In Figure 4.3 the expected significance ( $Z_\mu^{exp}$ ) and expected upper limits ( $\mu_{up}^{exp}$ ) for a range of different configurations  
 637 of DL1r  $b$ -tagged jet working points across different regions.

638 From Figure 4.3, we can see that requiring that  $b$ -tagged jets pass the 77% DL1r WP in the  $tWZ$  SR,  $(tWZ)_{fake}$   
 639 CR and the  $ZZb$  CR and that at least one  $b$ -tagged jet in the  $t\bar{t}Z$  SR passes the 77% DL1r WP (the other jet is  
 640 just required to pass the 85% DL1r WP) maximises the sensitivity overall (compared to the other investigated  
 641 configurations). This configuration was chosen  $b$ -tagged jets.

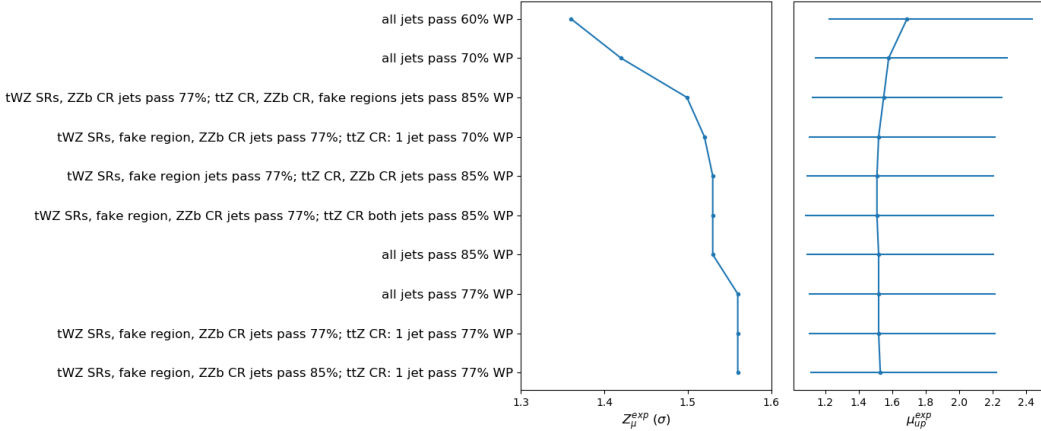


Figure 4.3: Expected significance ( $Z_\mu^{\text{exp}}$ ) and expected upper limit ( $\mu_{\text{up}}^{\text{exp}}$ ) for different configurations of DL1r  $b$ -tagged jet working points is shown. The common y-axis shows the different configurations of DL1r  $b$ -tagged jet working points. On the left panel, the expected significance from the likelihood fit is shown on the x-axis. On the right panel, the expected upper limit from the likelihood fit is shown on the x-axis (with the corresponding total uncertainty represented by horizontal lines).

642

643 The  $p_T$ (L Lepton) is constrained by the single lepton triggers (Table ??). We choose to apply a cut on the  
 644  $p_T$ (NL Lepton) slightly tighter than the tightest single lepton  $p_T$  cut in the trigger. We can however, try optimising  
 645 the  $p_T$ (NL Lepton) cut by comparing the expected significance and limit for a range of  $p_T$ NL Lepton cuts to  
 646 determine the cut which maximizes sensitivity.

647

648 In Figure 4.4 the expected significance ( $Z_\mu^{\text{exp}}$ ) and expected upper limits ( $\mu_{\text{up}}^{\text{exp}}$ ) for different  $p_T$ (NL Lepton) cuts is  
 shown.

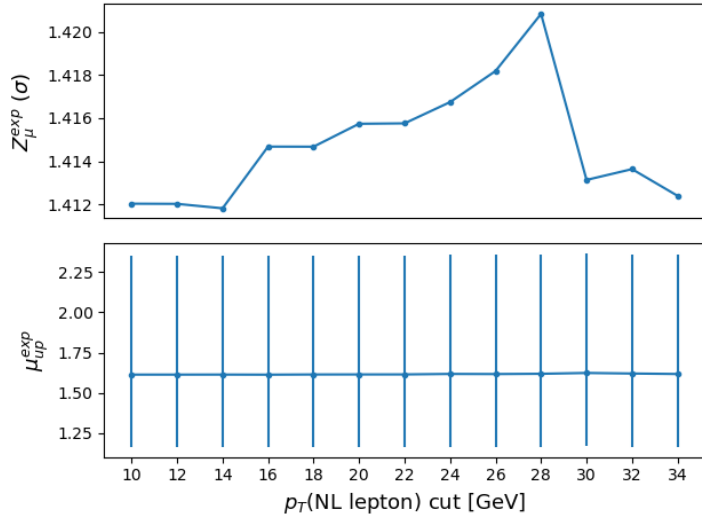


Figure 4.4: Expected significance ( $Z_\mu^{\text{exp}}$ ) and expected upper limit ( $\mu_{\text{up}}^{\text{exp}}$ ) for different  $p_T$ (NL Lepton) cuts is shown. The common x-axis shows cut applied to the  $p_T$  of the next-to-leading lepton. On the top panel, the expected significance from the likelihood fit is shown on the y-axis. On the bottom panel, the expected upper limit from the likelihood fit is shown on the y-axis (with the corresponding total uncertainty represented by vertical lines).

649

650 Since there is a very small change between the different  $p_T$ (NL Lepton) cuts on the sensitivity of  $tWZ$ , we choose  
 651 to apply a  $p_T$ (NL Lepton) cut at 18 GeV (avoiding a  $p_T$  cut near the sharp drop in expected significance after  
 652 28 GeV), therefore applying a cut above the tightest, looser dilepton trigger  $p_T$  cut (17 GeV) to suppress any

653 systematic from the modelling of the trigger efficiency.

## 654 4.5 Signal and Control Regions

655 In this section, pre-fit distributions of variables in each region are shown. More pre-fit distributions for each region  
 656 are shown in the appendix (Section ??). For each figure in this section, the data is given by the black points and  
 657 the MC predictions for each process are given by the histograms. The vertical lines on the data points represent  
 658 the total uncertainty in the data and the diagonal lined bands represent the total MC uncertainty. The lower panel  
 659 in each plot shows the ratios of the data to the theoretical predictions. Bins with a  $\frac{signal}{background}$  yield greater than  
 660 0.1 are kept blinded. Blinded bins are shaded with black diagonal lines and their data points are omitted.

661 In Table 4.4, the pre-fit yields for each sample in each region is shown.

	$tWZ$ OF SR	$tWZ$ SF SR	$t\bar{t}Z$ CR	$ZZb$ CR	$(tWZ)_{fake}$ CR
$t\bar{t}Z$	$13.9325 \pm 1.84643$	$10.1343 \pm 1.36039$	$31.7149 \pm 4.46776$	$5.26303 \pm 0.696828$	$19.1224 \pm 2.50011$
$t\bar{t}Z$ fakes	$0.0687541 \pm 0.0482172$	$0.032827 \pm 0.026286$	$0.0709734 \pm 0.043509$	$0.0474576 \pm 0.0301512$	$4.94775 \pm 2.48939$
$tWZ$	$3.81359 \pm 0.392241$	$2.57584 \pm 0.326401$	$2.61991 \pm 0.861557$	$1.4023 \pm 0.156686$	$4.93485 \pm 0.692143$
$ZZ$	$0.546045 \pm 0.18975$	$8.76232 \pm 2.66871$	$1.22357 \pm 0.376889$	$46.0616 \pm 13.9203$	$7.76724 \pm 2.36894$
other	$t\bar{t}$	$6e-06 \pm 3.04506e-06$	$0.250783 \pm 0.44226$	$0.269883 \pm 0.223373$	$6e-06 \pm 3.04506e-06$
	$tZq$	$0.0827265 \pm 0.0399222$	$0.0757694 \pm 0.0355101$	$0.0637132 \pm 0.0293762$	$0.0590199 \pm 0.0244576$
	$t\bar{t}W$	$0.00674747 \pm 0.00793546$	$0.00279491 \pm 0.00287747$	$6e-06 \pm 3.04506e-06$	$0.00221727 \pm 0.00562041$
	$WZ$	$0.0439316 \pm 0.0241635$	$0.0397876 \pm 0.0154764$	$0.0134837 \pm 0.0128327$	$0.0474188 \pm 0.0330635$
	$t\bar{t}t$	$0.000987429 \pm 0.000768187$	$0.00249801 \pm 0.00138007$	$0.0141085 \pm 0.00486102$	$6e-06 \pm 3.04506e-06$
	$t\bar{t}\bar{t}$	$0.00934516 \pm 0.0080725$	$0.0107503 \pm 0.00852049$	$0.0570846 \pm 0.0206271$	$6e-06 \pm 3.04506e-06$
	$t\bar{t}WW$	$0.0293456 \pm 0.0263573$	$0.0296011 \pm 0.0196075$	$0.26412 \pm 0.0936908$	$0.013096 \pm 0.0323943$
	$VVV(V = W/Z)$	$0.280384 \pm 0.0866421$	$0.191257 \pm 0.0595588$	$0.0696624 \pm 0.0228108$	$0.171171 \pm 0.0526519$
	$t\bar{t}H$	$0.854064 \pm 0.177974$	$0.674566 \pm 0.141771$	$1.98187 \pm 0.406211$	$0.151447 \pm 0.0357703$
Total		$19.6684 \pm 1.95158$	$22.7832 \pm 3.10338$	$38.3633 \pm 4.6342$	$53.2187 \pm 13.9618$
data		-	-	36	49
					57

Table 4.4: The pre-fit yields for each sample in each region is shown.

662 The statistical uncertainty associated with the number of raw MC events (weighted by MC event weights) can  
 663 be quantified by the Number of Equivalent Events [42],  $N_{equiv}$ , which relates the sample of  $N$  weighted events to  
 664  $N_{equiv}$  events with all MC event weights equal to 1, that would have the same relative statistical fluctuation.  $N_{equiv}$   
 665 can be written as,

$$N_{equiv} = \frac{(\sum_i^N w_i)^2}{\sum_i^N w_i^2} \quad (4.1)$$

666 where  $w_i$  is the MC event weight for event  $i$ . The standard uncertainty of  $N_{equiv}$  is given by  $u(N_{equiv}) = \sqrt{N_{equiv}}$ .

667 In Table 4.5, the number of equivalent events,  $N_{equiv}$  (and its percentage uncertainty), is shown for each sample  
 668 in each region.  $N_{equiv}$  is relatively large, compared to the background processes, for the  $tWZ$  signal in all regions.

	$tWZ$ OF SR	$tWZ$ SF SR	$t\bar{t}Z$ CR	$ZZb$ CR	$(tWZ)_{fake}$ CR			
	$N_{equiv}$	Uncertainty [%]	$N_{equiv}$	Uncertainty [%]	$N_{equiv}$	Uncertainty [%]	$N_{equiv}$	Uncertainty [%]
$tWZ$	$6463.29 \pm 80.39$	1.24	$4153.0 \pm 64.44$	1.55	$4800.67 \pm 69.29$	1.44	$2497.07 \pm 49.97$	2.0
$t\bar{t}Z$	$1363.87 \pm 36.93$	2.71	$1031.04 \pm 32.11$	3.11	$3237.01 \pm 56.89$	1.76	$561.41 \pm 23.69$	4.22
$ZZ$	$50.89 \pm 7.13$	14.02	$975.61 \pm 31.23$	3.2	$267.85 \pm 16.37$	6.11	$7023.35 \pm 83.81$	1.19
other	$748.0 \pm 27.35$	3.66	$2.47 \pm 1.57$	63.58	$4.23 \pm 2.06$	48.6	$255.32 \pm 15.98$	6.26
$t\bar{t}Z$ fakes	$6.72 \pm 2.59$	38.56	$1.31 \pm 1.14$	87.34	$16.05 \pm 4.01$	24.96	$7.15 \pm 2.67$	37.41
Total	$8632.77 \pm 92.91$	1.08	$6163.44 \pm 78.51$	1.27	$8325.81 \pm 91.25$	1.1	$10344.3 \pm 101.71$	0.98
							$12044.27 \pm 109.75$	0.91

Table 4.5: The number of equivalent events,  $N_{equiv}$  (and its percentage uncertainty), is shown for each sample in each region.

670 This tells us that we have a large number of raw MC events for the  $tWZ$  sample. An extended  $tWZ$  sample was  
 671 generated to increase the number of signal events used to train the event-level BDT (See Section 4.7.2).

### 673 4.5.1 $tWZ$ OF SR

674 In this section, pre-fit distributions of variables in the  $tWZ$  OF SR are shown. More pre-fit distributions for the  
 675  $tWZ$  OF SR are shown in the appendix (Section ??).

676

677 In Figure 4.5 MC predictions for  $p_T$ ,  $\eta$  and  $\phi$  for leading (L) leptons and next-to-leading (NL) leptons in the  $tWZ$   
 678 OF SR region is shown.

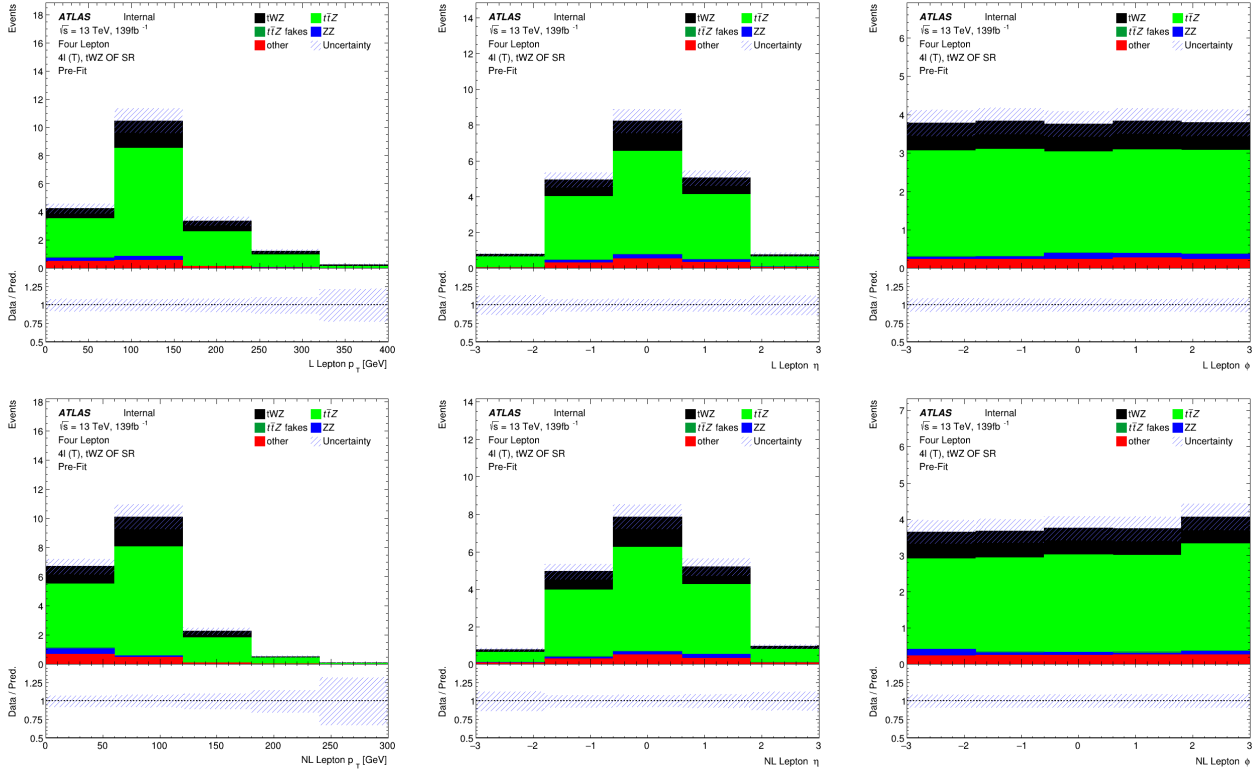


Figure 4.5: MC predictions for  $p_T$ ,  $\eta$  and  $\phi$  for leading (L) leptons (top row) and next-to-leading (NL) leptons (bottom row) in the  $tWZ$  OF SR region is shown.

679 In Figure 4.6 MC predictions for  $p_T$ ,  $\eta$  and  $\phi$  for leading (L) jets and next-to-leading (NL) jets in the  $tWZ$  OF SR  
 680 region is shown.  
 681 In Figure 4.7 MC predictions for  $p_T$ ,  $\eta$  and  $\phi$  of the next-to-next-to-leading (NNL) jets,  $H_T$  (scalar sum of Jet  $p_T$ )  
 682 and the Number of jets in the  $tWZ$  OF SR region is shown.  
 683 In Figure 4.8 MC predictions for  $p_T$ ,  $\eta$  and  $\phi$  of the leading b-tagged jets, the scalar sum of b-tagged jet  $p_T$  and  
 684 the Number of b-tagged jets in the  $tWZ$  OF SR region is shown.

### 685 4.5.2 $tWZ$ SF SR

686 In this section, pre-fit distributions of variables in the  $tWZ$  SF SR are shown. More pre-fit distributions for the  
 687  $tWZ$  SF SR are shown in the appendix (Section ??).  
 688  
 689 In Figure 4.9 MC predictions for  $p_T$ ,  $\eta$  and  $\phi$  for leading (L) leptons and next-to-leading (NL) leptons in the  $tWZ$   
 690 SF SR region is shown.  
 691 In Figure 4.10 MC predictions for  $p_T$ ,  $\eta$  and  $\phi$  for leading (L) jets and next-to-leading (NL) jets in the  $tWZ$  SF SR  
 692 region is shown.  
 693 In Figure 4.11 MC predictions for  $p_T$ ,  $\eta$  and  $\phi$  of the next-to-next-to-leading (NNL) jets,  $H_T$  (scalar sum of Jet  $p_T$ )  
 694 and the Number of jets in the  $tWZ$  SF SR region is shown.  
 695 In Figure 4.12 MC predictions for  $p_T$ ,  $\eta$  and  $\phi$  of the leading b-tagged jets, the scalar sum of b-tagged jet  $p_T$  and  
 696 the Number of b-tagged jets in the  $tWZ$  SF SR region is shown.

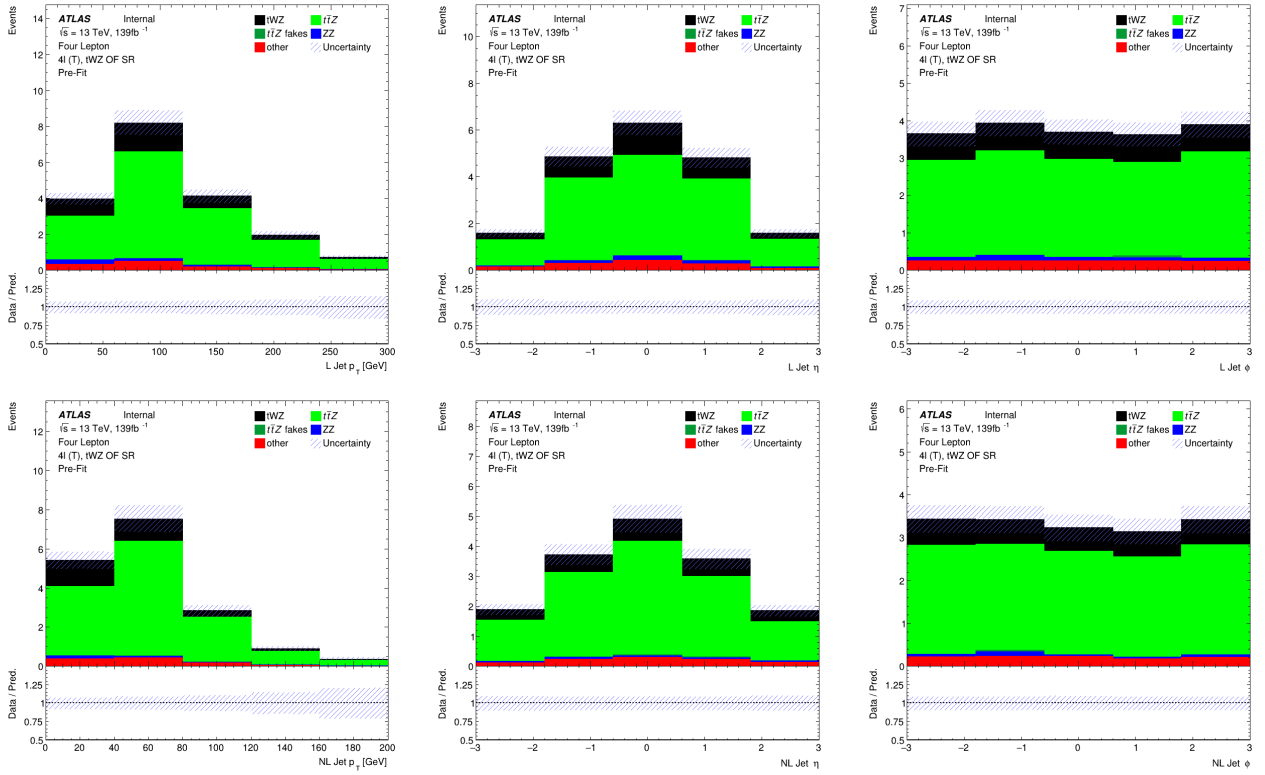


Figure 4.6: MC predictions for  $p_T$ ,  $\eta$  and  $\phi$  for leading (L) jets (top row) and next-to-leading (NL) jets (bottom row) in the  $tWZ$  OF SR region is shown.

### 4.5.3 $t\bar{t}Z$ CR

In this section, pre-fit distributions of variables in the  $t\bar{t}Z$  CR are shown. More pre-fit distributions for the  $t\bar{t}Z$  CR are shown in the appendix (Section ??).

In Figure 4.13 MC predictions for  $p_T$ ,  $\eta$  and  $\phi$  for leading (L) leptons and next-to-leading (NL) leptons in the  $t\bar{t}Z$  CR region is shown.

In Figure 4.14 MC predictions for  $p_T$ ,  $\eta$  and  $\phi$  for leading (L) jets and next-to-leading (NL) jets in the  $t\bar{t}Z$  CR region is shown.

In Figure 4.15 MC predictions for  $p_T$ ,  $\eta$  and  $\phi$  of the next-to-next-to-leading (NNL) jets,  $H_T$  (scalar sum of Jet  $p_T$ ) and the Number of jets in the  $t\bar{t}Z$  CR region is shown.

In Figure 4.16 MC predictions for  $p_T$ ,  $\eta$  and  $\phi$  of the leading b-tagged jets, the scalar sum of b-tagged jet  $p_T$  and the Number of b-tagged jets in the  $t\bar{t}Z$  CR region is shown.

### 4.5.4 $ZZb$ CR

In this section, pre-fit distributions of variables in the  $ZZb$  CR are shown. More pre-fit distributions for the  $ZZb$  CR are shown in the appendix (Section ??).

In Figure 4.17 MC predictions for  $p_T$ ,  $\eta$  and  $\phi$  for leading (L) leptons and next-to-leading (NL) leptons in the  $ZZb$  CR region is shown.

In Figure 4.18 MC predictions for  $p_T$ ,  $\eta$  and  $\phi$  for leading (L) jets and next-to-leading (NL) jets in the  $ZZb$  CR region is shown.

In Figure 4.19 MC predictions for  $p_T$ ,  $\eta$  and  $\phi$  of the next-to-next-to-leading (NNL) jets,  $H_T$  (scalar sum of Jet  $p_T$ ) and the Number of jets in the  $ZZb$  CR region is shown.

In Figure 4.20 MC predictions for  $p_T$ ,  $\eta$  and  $\phi$  of the leading b-tagged jets, the scalar sum of b-tagged jet  $p_T$  and the Number of b-tagged jets in the  $ZZb$  CR region is shown.

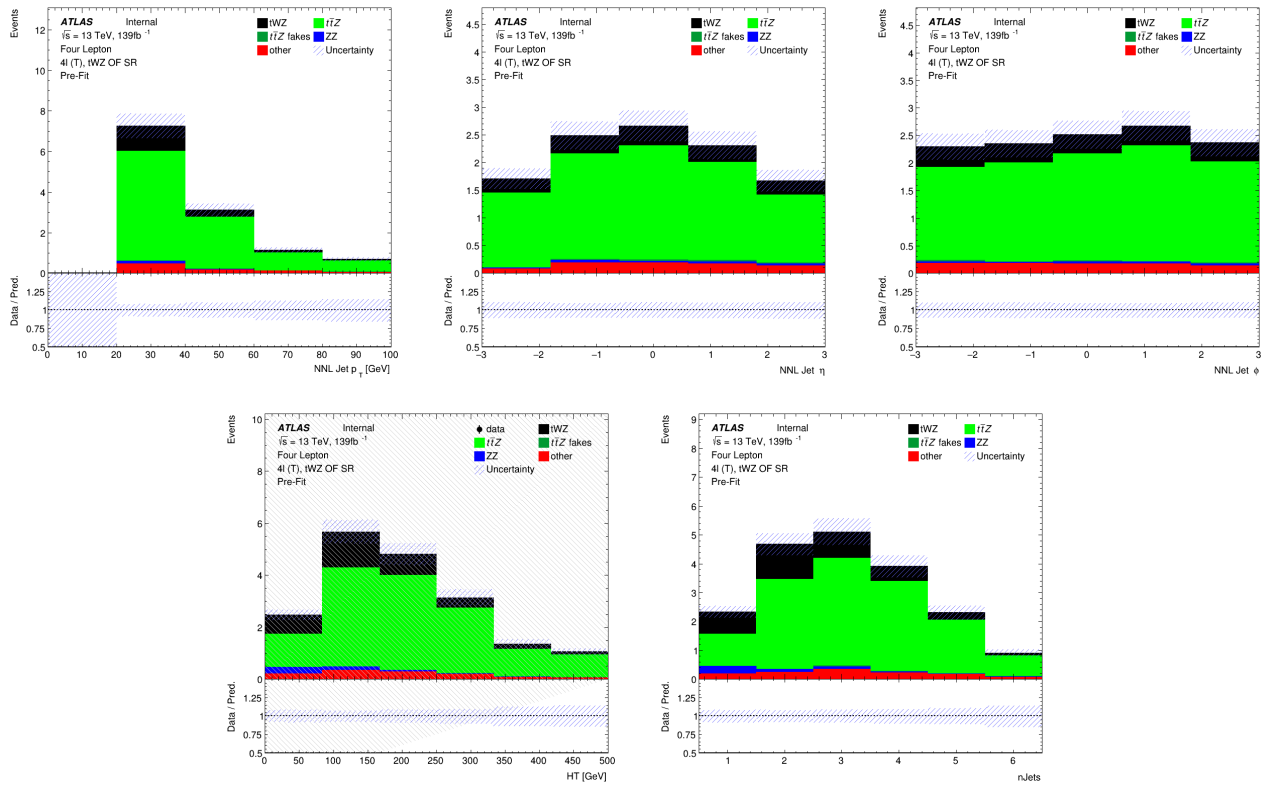


**Figure 4.7: Top row:** MC predictions for  $p_T$ ,  $\eta$  and  $\phi$  for next-to-next-to-leading (NNL) jets in the  $tWZ$  OF SR region is shown. **Bottom row:** MC predictions for  $H_T$  (scalar sum of Jet  $p_T$ ) (left) and the Number of jets (right) in the  $tWZ$  OF SR region is shown.

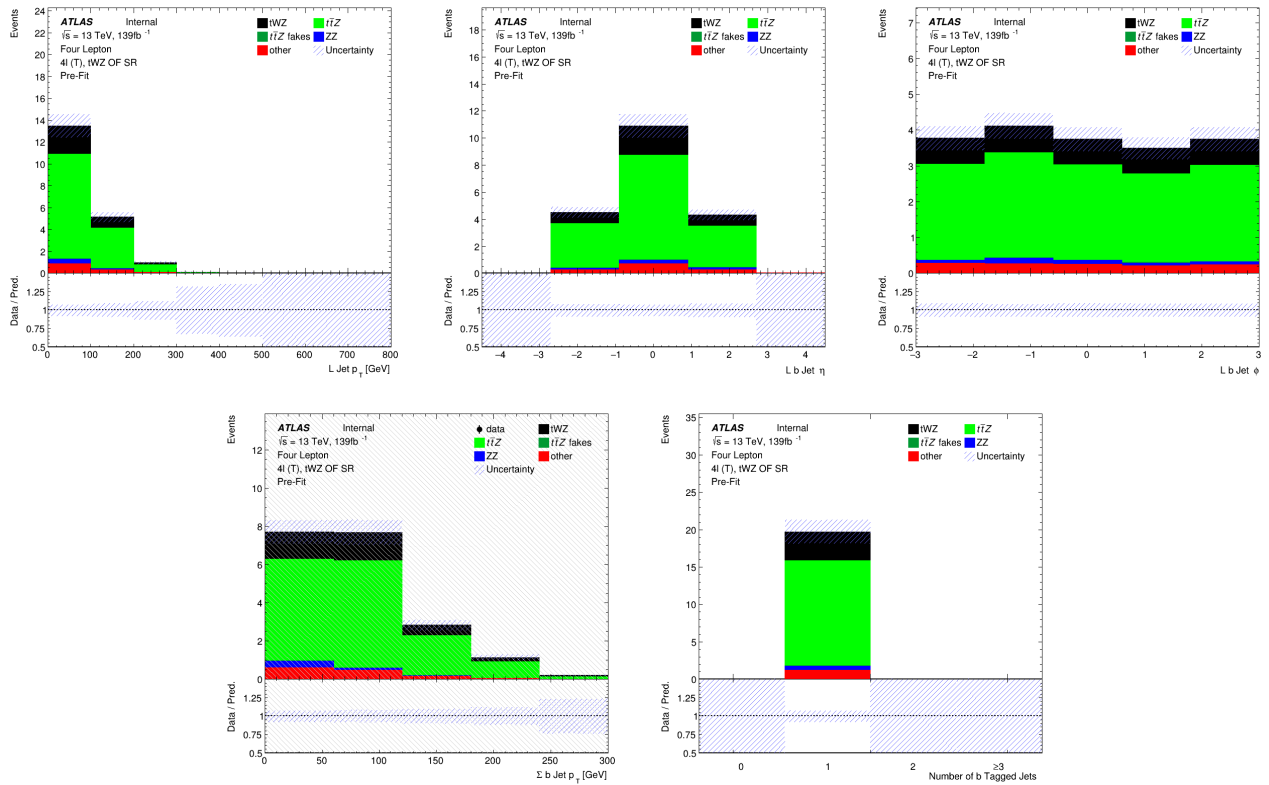


**Figure 4.8:** **Top row:** MC predictions for  $p_T$ ,  $\eta$  and  $\phi$  for leading b-tagged jets in the  $tWZ$  OF SR region is shown. **Bottom row:** MC predictions for the scalar sum of b-tagged jet  $p_T$  (left) and the Number of b-tagged jets (right) in the  $tWZ$  OF SR region is shown.

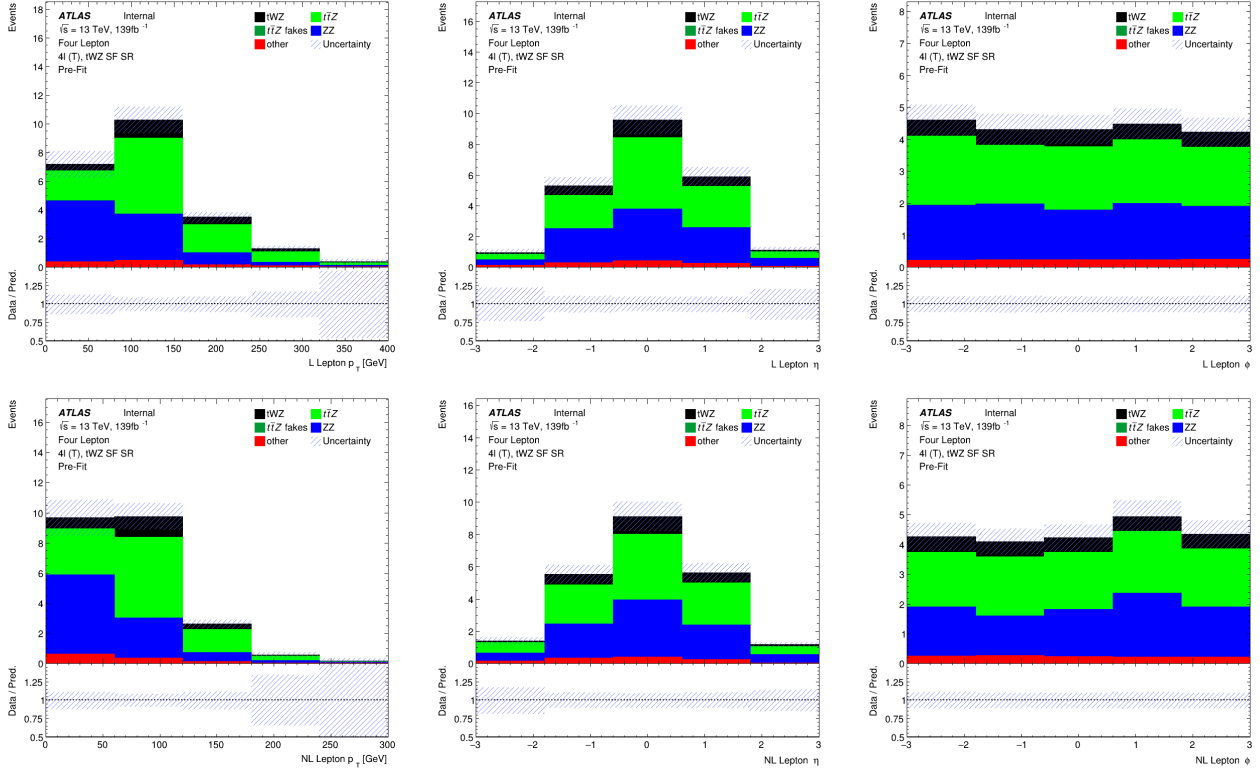


Figure 4.9: MC predictions for  $p_T$ ,  $\eta$  and  $\phi$  for leading (L) leptons (top row) and next-to-leading (NL) leptons (bottom row) in the  $tWZ$  SF SR region is shown.

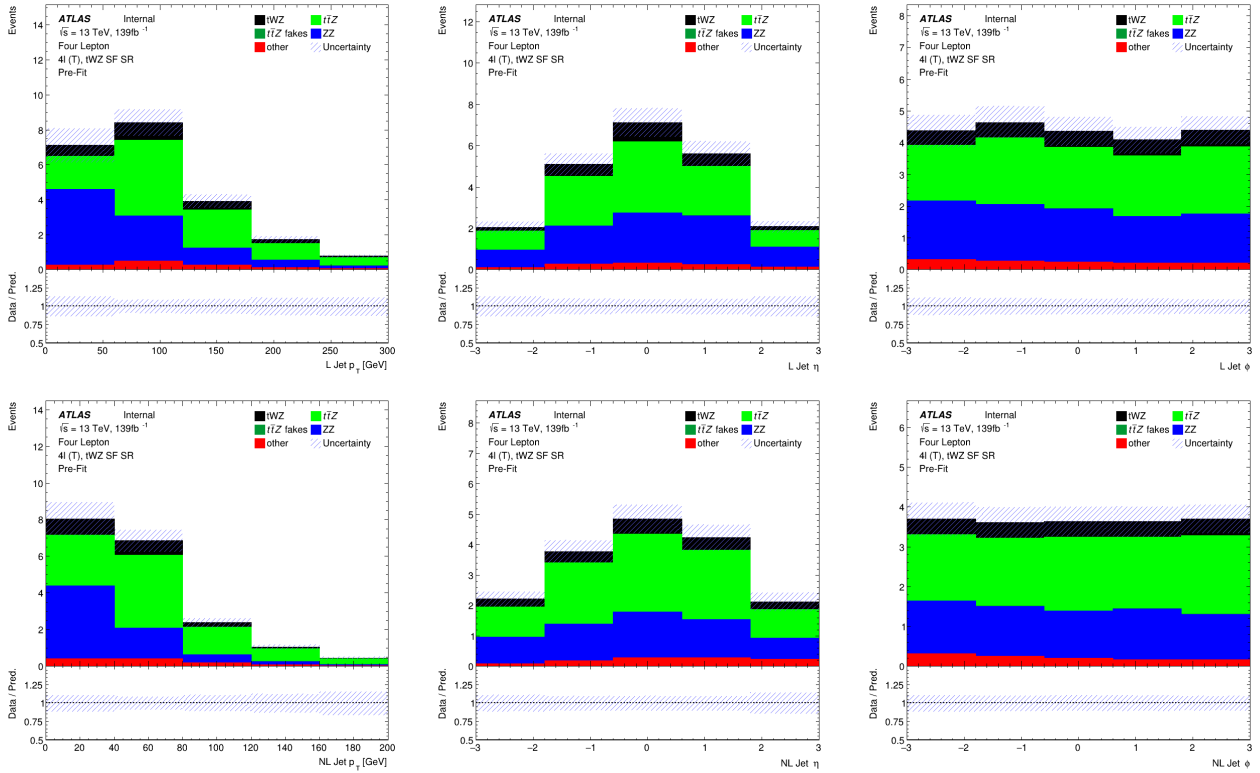
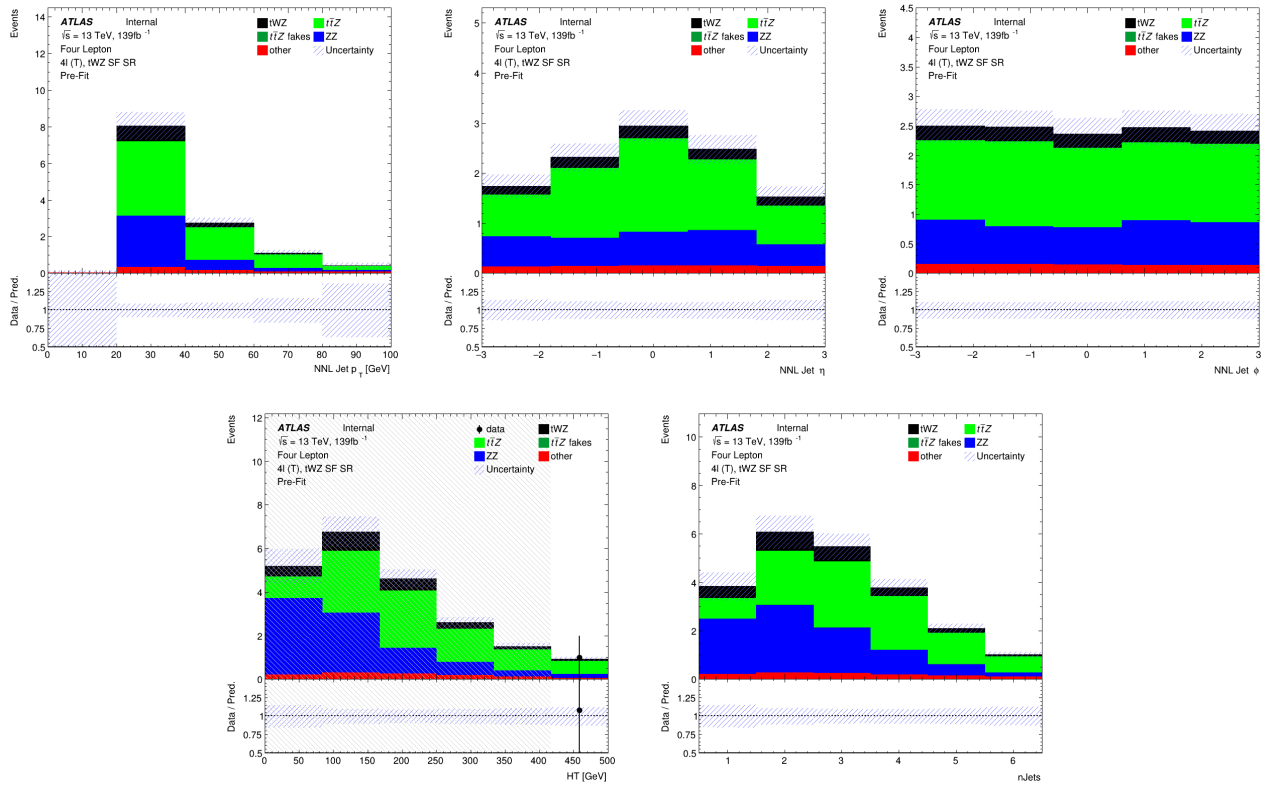


Figure 4.10: MC predictions for  $p_T$ ,  $\eta$  and  $\phi$  for leading (L) jets (top row) and next-to-leading (NL) jets (bottom row) in the  $tWZ$  SF SR region is shown.



**Figure 4.11:** **Top row:** MC predictions for  $p_T$ ,  $\eta$  and  $\phi$  for next-to-next-to-leading (NNL) jets in the  $tWZ$  SF SR region is shown. **Bottom row:** MC predictions for  $H_T$  (scalar sum of Jet  $p_T$ ) (left) and the Number of jets (right) in the  $tWZ$  SF SR region is shown.

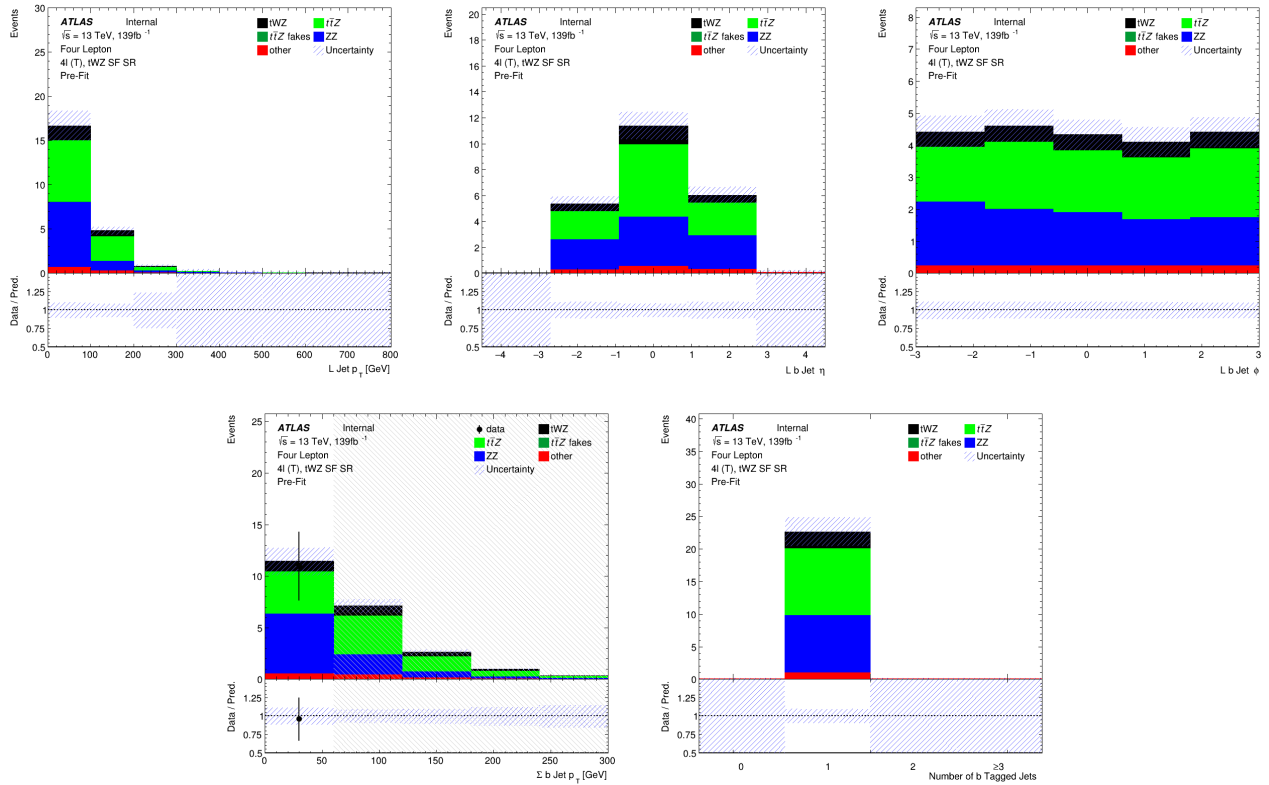


Figure 4.12: **Top row:** MC predictions for  $p_T$ ,  $\eta$  and  $\phi$  for leading b-tagged jets in the  $tWZ$  SF SR region is shown. **Bottom row:** MC predictions for the scalar sum of b-tagged jet  $p_T$  (left) and the Number of b-tagged jets (right) in the  $tWZ$  SF SR region is shown.

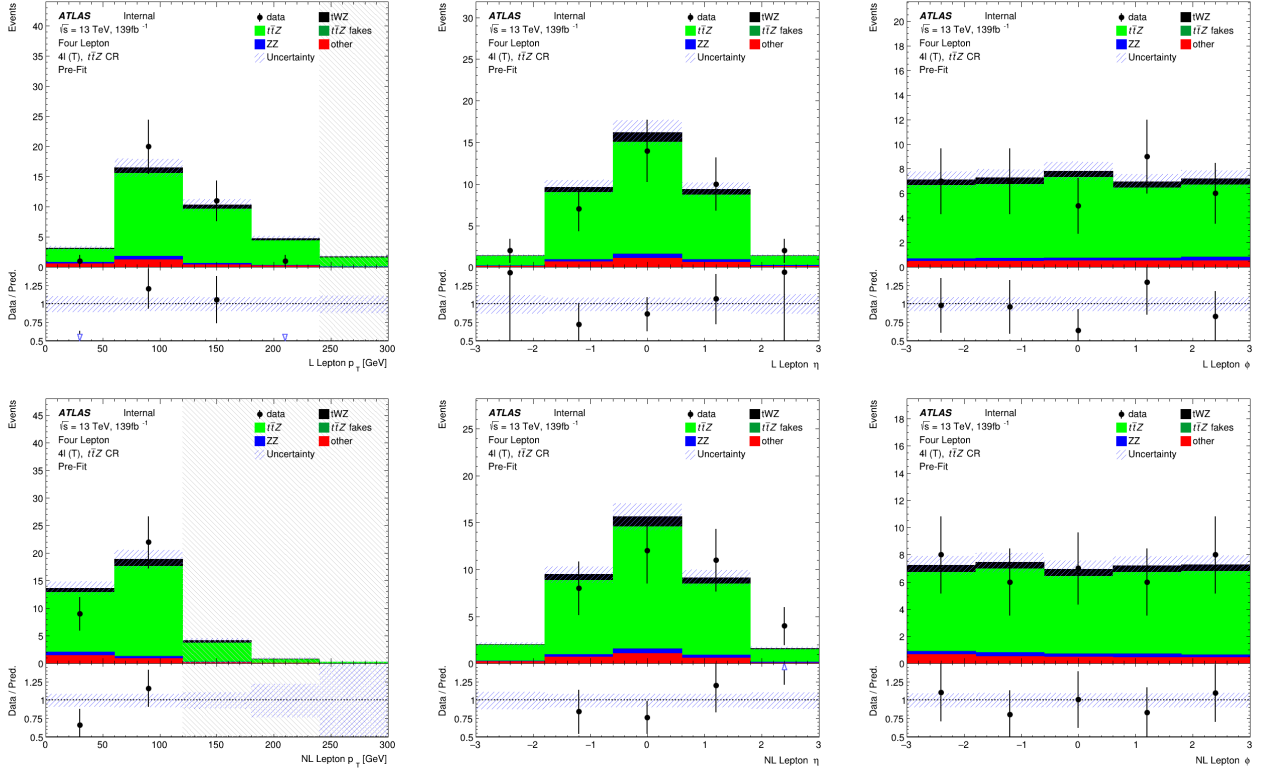


Figure 4.13: MC predictions for  $p_T$ ,  $\eta$  and  $\phi$  for leading (L) leptons (top row) and next-to-leading (NL) leptons (bottom row) in the  $t\bar{t}Z$  CR region is shown.

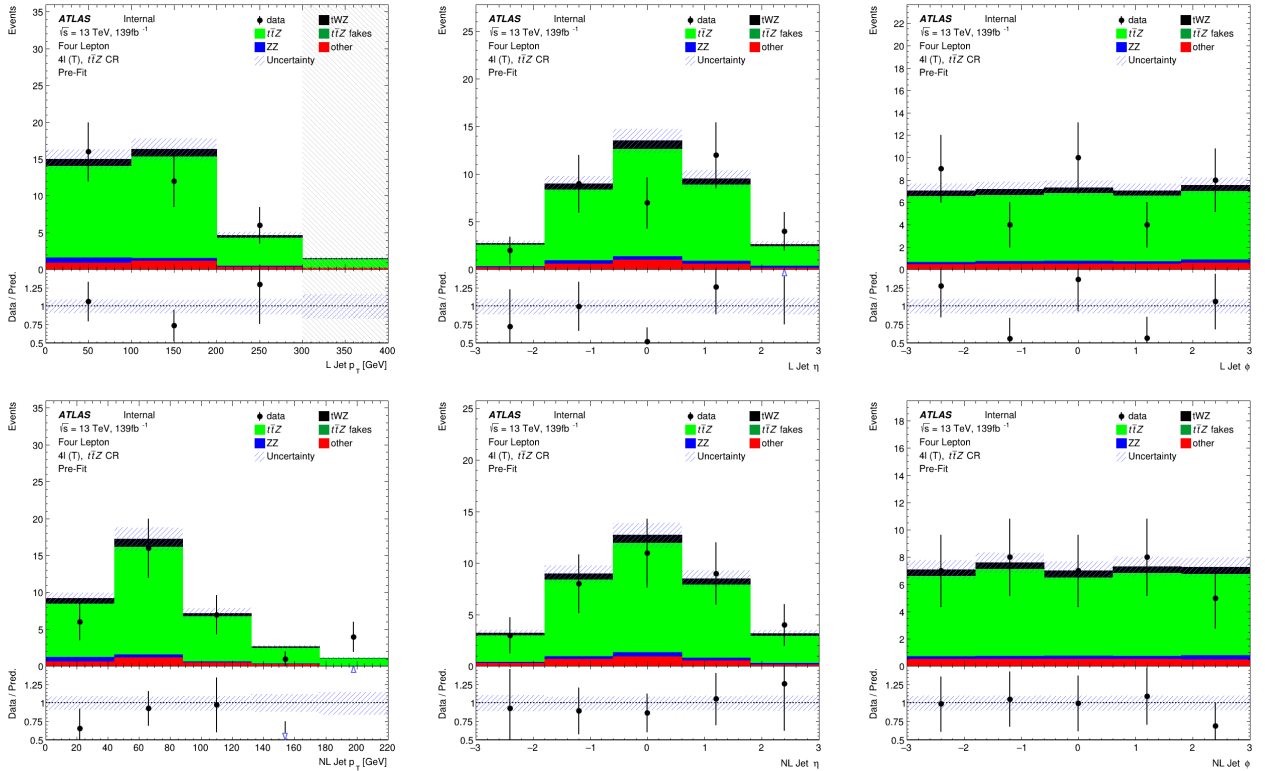


Figure 4.14: MC predictions for  $p_T$ ,  $\eta$  and  $\phi$  for leading (L) jets (top row) and next-to-leading (NL) jets (bottom row) in the  $t\bar{t}Z$  CR region is shown.

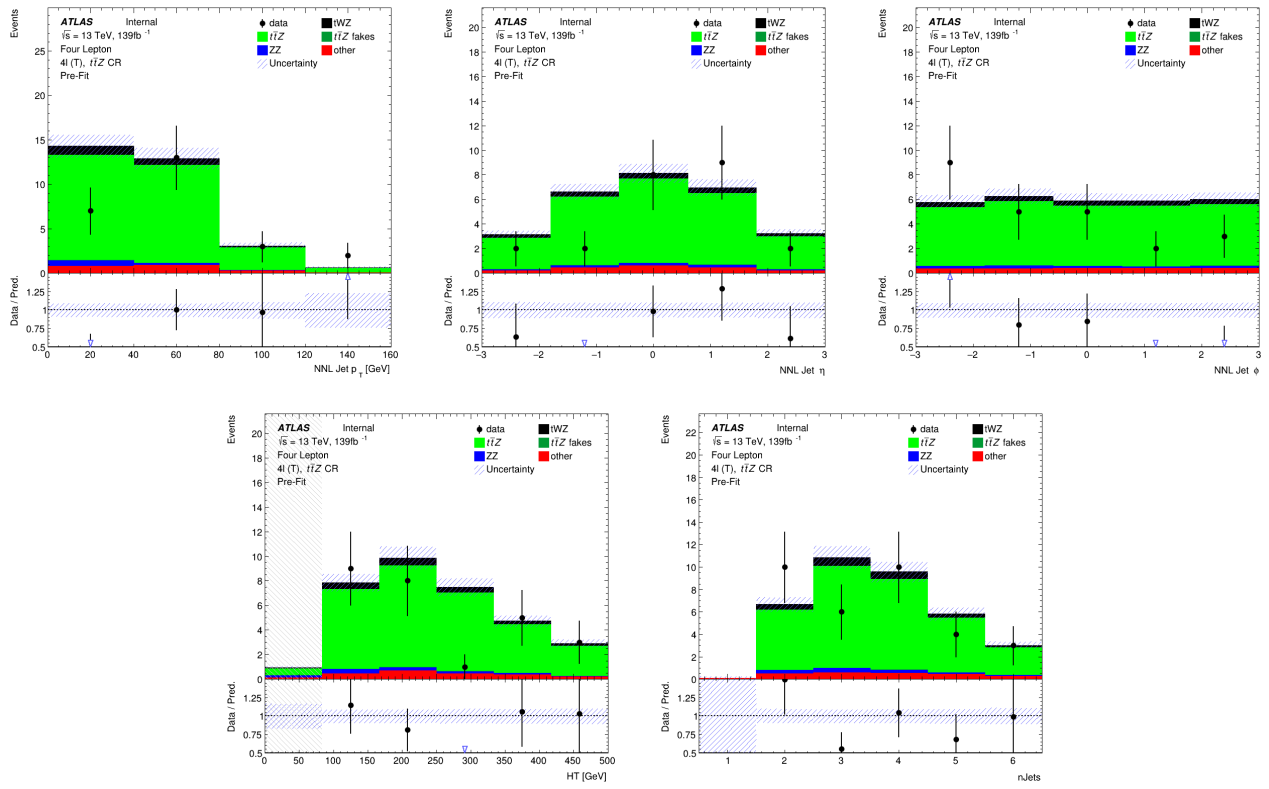
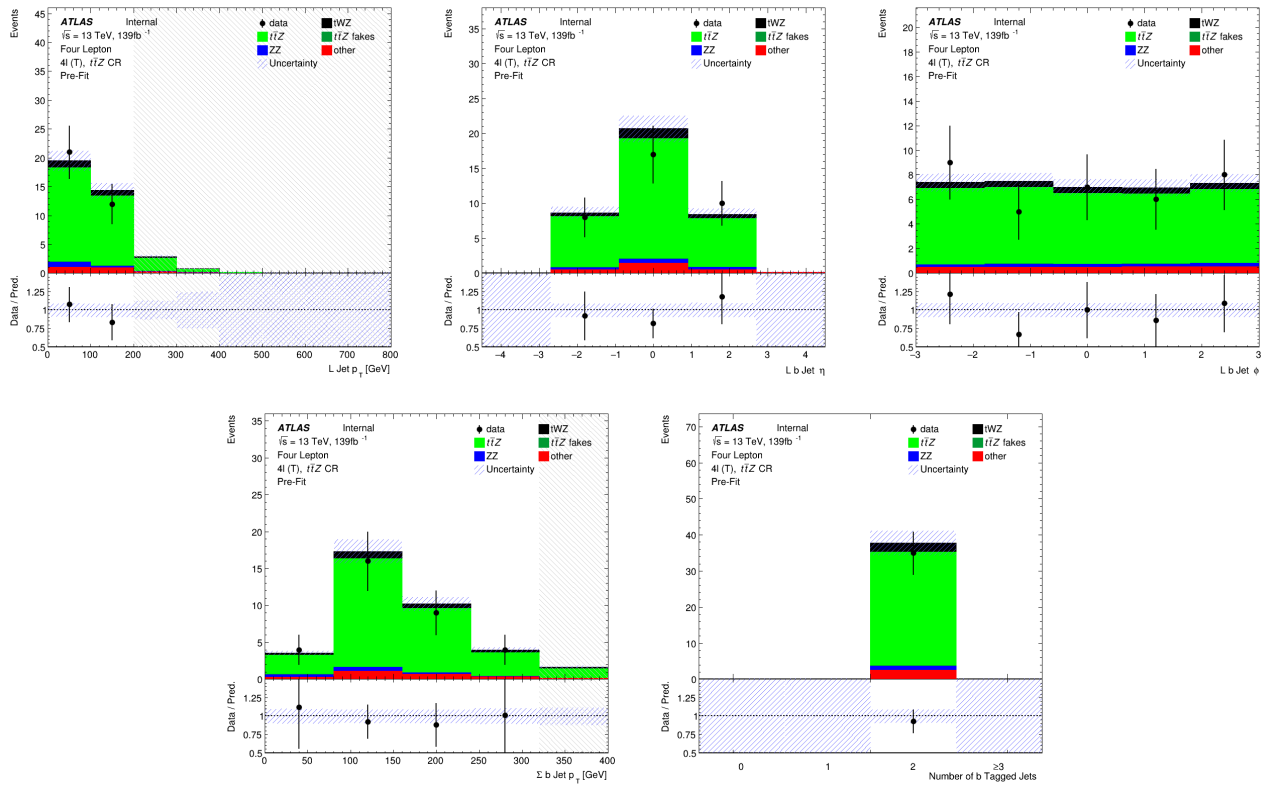


Figure 4.15: **Top row:** MC predictions for  $p_T$ ,  $\eta$  and  $\phi$  for next-to-next-to-leading (NNL) jets in the  $t\bar{t}Z$  CR region is shown. **Bottom row:** MC predictions for  $H_T$  (scalar sum of Jet  $p_T$ ) (left) and the Number of jets (right) in the  $t\bar{t}Z$  CR region is shown.



**Figure 4.16:** **Top row:** MC predictions for  $p_T$ ,  $\eta$  and  $\phi$  for leading b-tagged jets in the  $t\bar{t}Z$  CR region is shown. **Bottom row:** MC predictions for the scalar sum of b-tagged jet  $p_T$  (left) and the Number of b-tagged jets (right) in the  $t\bar{t}Z$  CR region is shown.

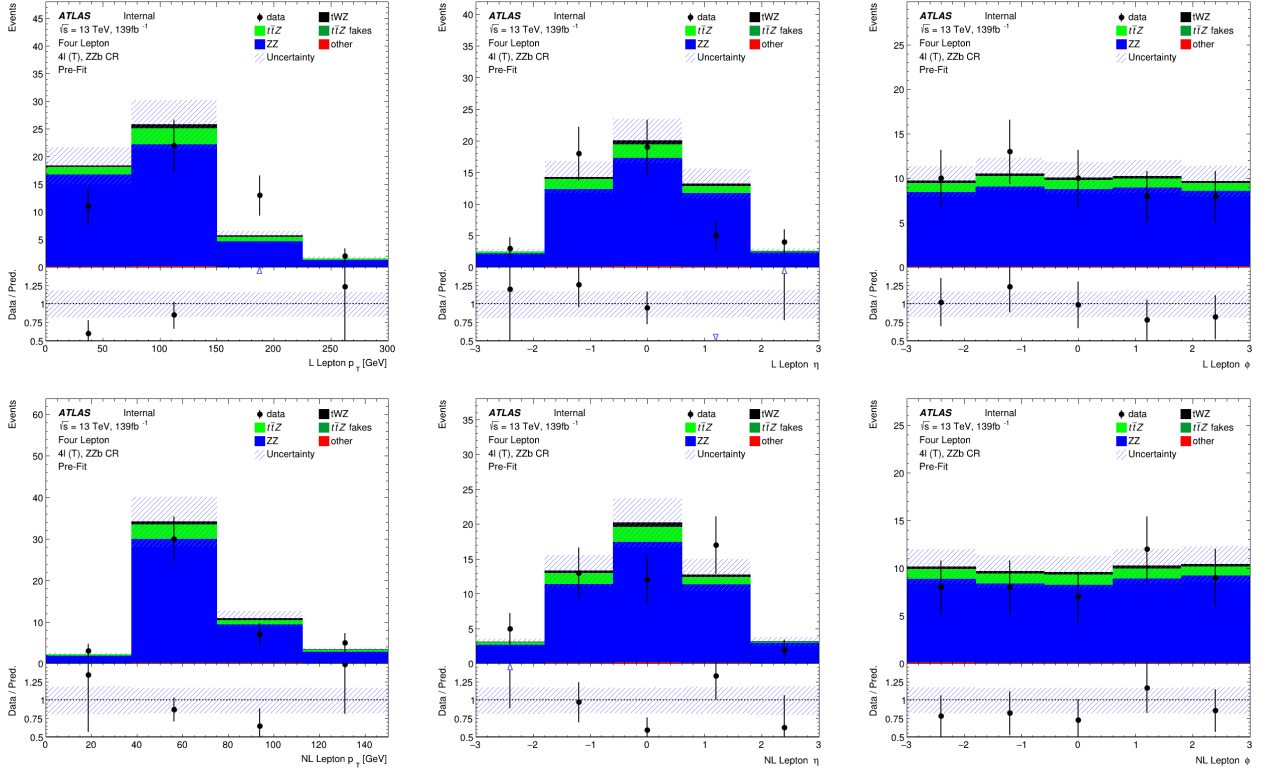


Figure 4.17: MC predictions for  $p_T$ ,  $\eta$  and  $\phi$  for leading (L) leptons (top row) and next-to-leading (NL) leptons (bottom row) in the  $ZZb$  CR region is shown.

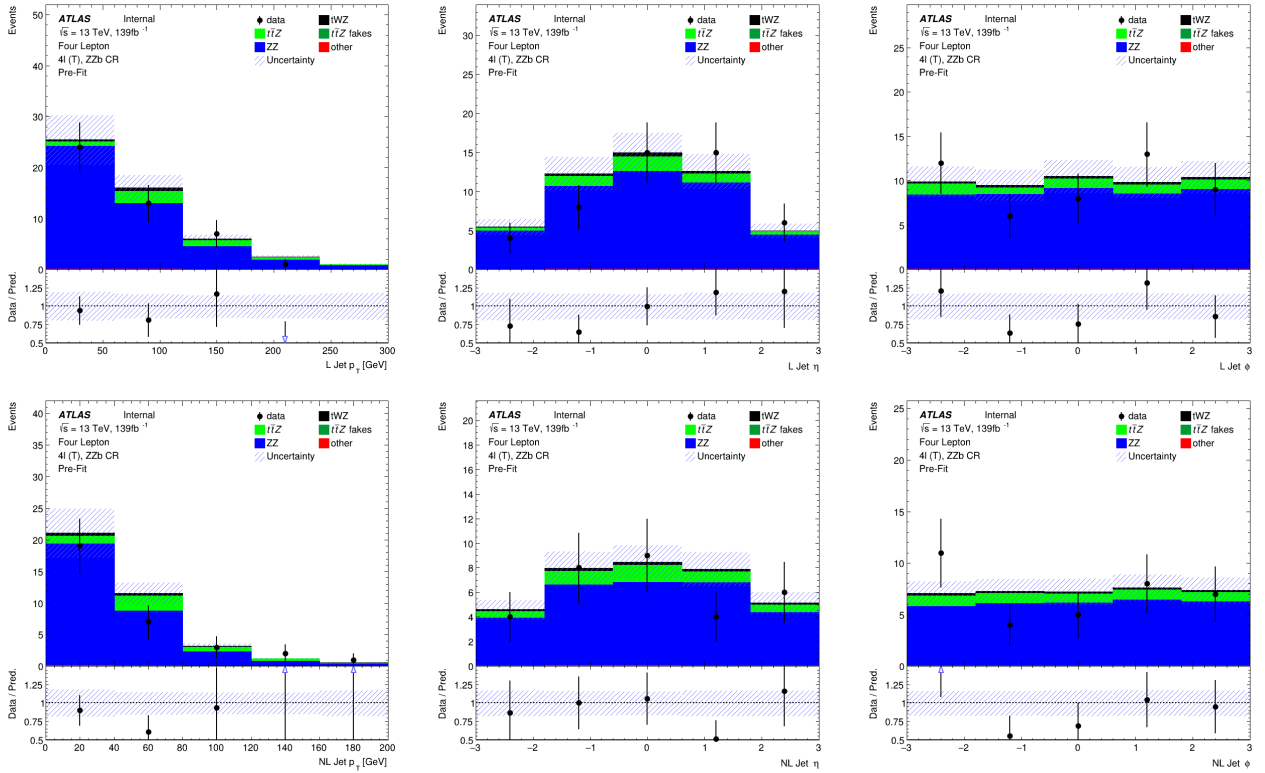


Figure 4.18: MC predictions for  $p_T$ ,  $\eta$  and  $\phi$  for leading (L) jets (top row) and next-to-leading (NL) jets (bottom row) in the  $ZZb$  CR region is shown.

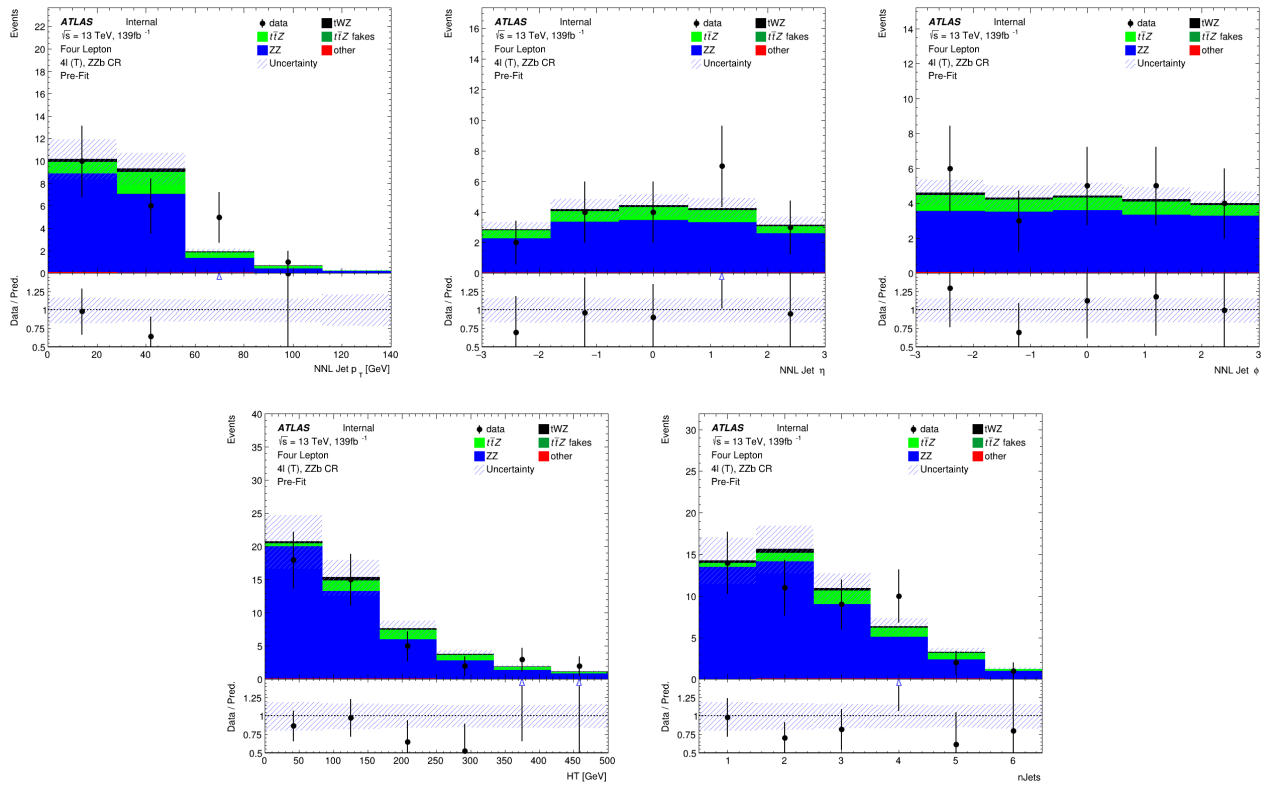
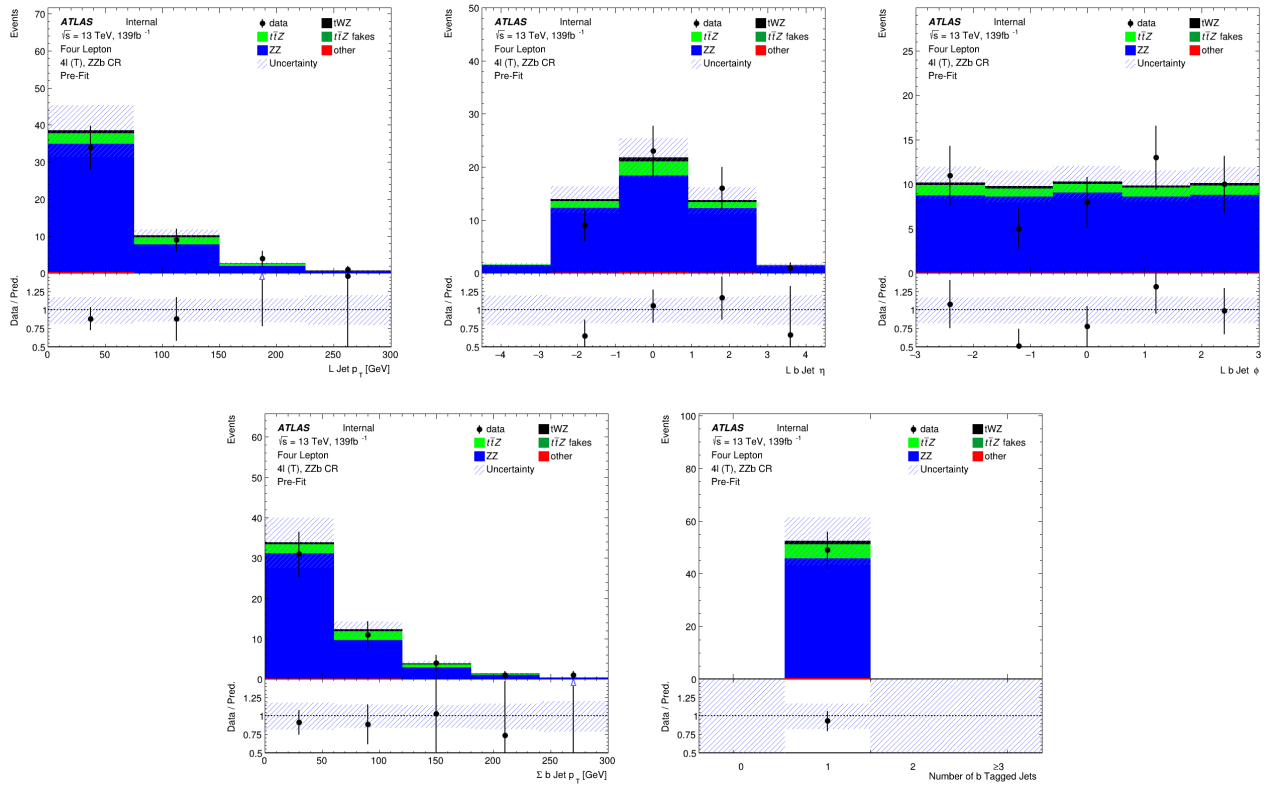


Figure 4.19: **Top row:** MC predictions for  $p_T$ ,  $\eta$  and  $\phi$  for next-to-next-to-leading (NNL) jets in the  $ZZb$  CR region is shown. **Bottom row:** MC predictions for  $H_T$  (scalar sum of Jet  $p_T$ ) (left) and the Number of jets (right) in the  $ZZb$  CR region is shown.



**Figure 4.20:** **Top row:** MC predictions for  $p_T$ ,  $\eta$  and  $\phi$  for leading b-tagged jets in the  $ZZb$  CR region is shown.  
**Bottom row:** MC predictions for the scalar sum of b-tagged jet  $p_T$  (left) and the Number of b-tagged jets (right) in the  $ZZb$  CR region is shown.

### 4.5.5 $(tWZ)_{\text{fake}}$ CR

In this section, pre-fit distributions of variables in the  $(tWZ)_{\text{fake}}$  CR are shown. More pre-fit distributions for the  $(tWZ)_{\text{fake}}$  CR are shown in the appendix (Section ??).

In Figure 4.21 MC predictions for  $p_T$ ,  $\eta$  and  $\phi$  for leading (L) leptons and next-to-leading (NL) leptons in the  $(tWZ)_{\text{fake}}$  CR region is shown.

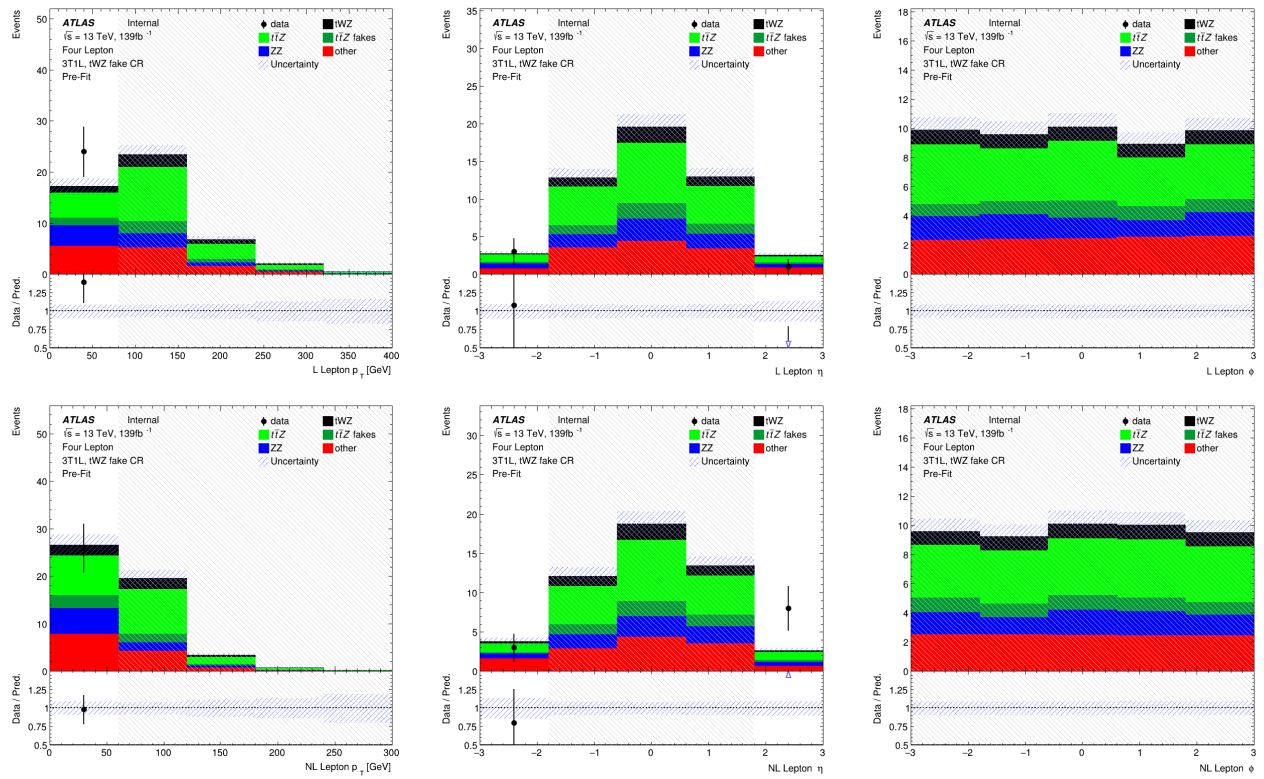


Figure 4.21: MC predictions for  $p_T$ ,  $\eta$  and  $\phi$  for leading (L) leptons (top row) and next-to-leading (NL) leptons (bottom row) in the  $(tWZ)_{\text{fake}}$  CR region is shown.

In Figure 4.22 MC predictions for  $p_T$ ,  $\eta$  and  $\phi$  for leading (L) jets and next-to-leading (NL) jets in the  $(tWZ)_{\text{fake}}$  CR region is shown.

In Figure 4.23 MC predictions for  $p_T$ ,  $\eta$  and  $\phi$  of the next-to-next-to-leading (NNL) jets,  $H_T$  (scalar sum of Jet  $p_T$ ) and the Number of jets in the  $(tWZ)_{\text{fake}}$  CR region is shown.

In Figure 4.24 MC predictions for  $p_T$ ,  $\eta$  and  $\phi$  of the leading b-tagged jets, the scalar sum of b-tagged jet  $p_T$  and the Number of b-tagged jets in the  $(tWZ)_{\text{fake}}$  CR region is shown.

Given the limited statistics which we are presented with in the tetralepton channel, we nevertheless observe relatively good agreement overall between data and MC.

## 4.6 Fake Lepton Estimation

Fake leptons are objects reconstructed as leptons, but do not correspond to the leptons which we are interested in our analysis. Fake leptons can be split up into two main categories, irreducible (prompt) fakes and reducible (non-prompt) fakes. Irreducible fakes are true leptons which do not come from the process of interest. Reducible fakes are objects which are mis-identified or incorrectly reconstructed as leptons. In the ATLAS detector, the probability for a fake to occur is very low.

We aim to estimate the fake lepton contribution in this analysis. We start off by noticing that  $t\bar{t}Z$  is our most dominant background ( $\sim 75\%$  of the total background contribution) and will therefore have the largest fake component compared to all other samples considered in the analysis. The fake lepton efficiency,  $\epsilon$ , can be written

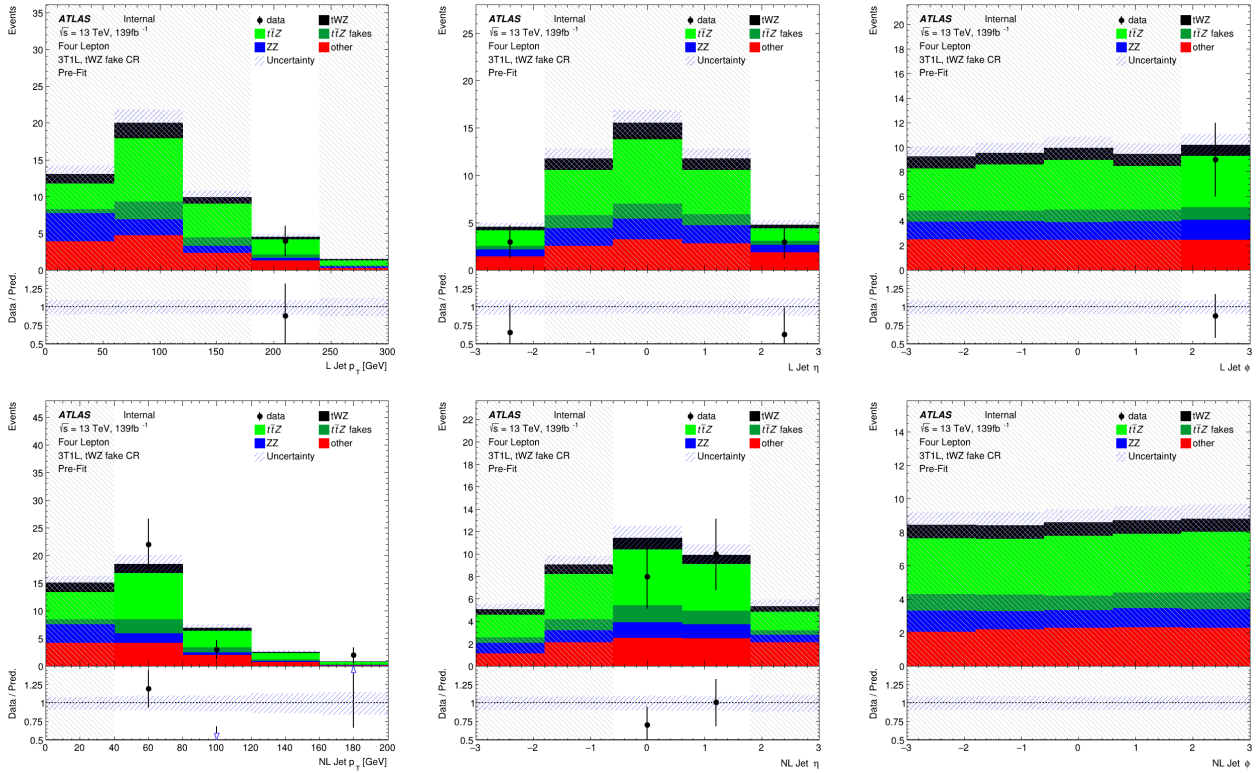


Figure 4.22: MC predictions for  $p_T$ ,  $\eta$  and  $\phi$  for leading (L) jets (top row) and next-to-leading (NL) jets (bottom row) in the  $(tWZ)_{\text{fake}}$  CR region is shown.

as  $\epsilon = \frac{N_{\text{fake}}^{\text{tight}}}{N_{\text{fake}}^{\text{loose}}}$ , where  $N_{\text{fake}}^{\text{tight}}$  is the number of fake leptons which pass the tight lepton selection (See Section 4.2.1) and  $N_{\text{fake}}^{\text{loose}}$  is the number of fake leptons which pass the loose lepton selection (See Section 4.2.1). The probability of one fake lepton to occur,  $P(\text{one fake } \ell)$ , is proportional to  $\epsilon$  and the probability for two fakes to occur is simply,  $P(\text{two fake } \ell) = (P(\text{one fake } \ell))^2 \propto \epsilon^2$ . Since  $\epsilon < 1$ , we have  $P(\text{one fake } \ell) \ll P(\text{two fake } \ell)$ . For this analysis we shall investigate the fake lepton component to the highest order and therefore we will consider the case where at least one fake lepton occurs in a  $t\bar{t}Z$  event.

Firstly, we split up the dominant  $t\bar{t}Z$  background into  $t\bar{t}Z$  and  $(t\bar{t}Z)_{\text{fake}}$  components. Secondly, we define a  $(tWZ)_{\text{fake}}$  CR (See Section 4.4) which is enhanced in fakes and aims to constrain the  $(t\bar{t}Z)_{\text{fake}}$  background in the SR.

All events which contribute to the  $(t\bar{t}Z)_{\text{fake}}$  background are determined by the IFF Truth Classifier [50]. The IFF Truth Classifier is a tool which aims to classify leptons based off their truth information. It uses the more general MCTruthClassifier [60] tool's output as input and returns one of the following lepton categories: Unknown, KnownUnknown (leptons which can (in principle) be classified, but the MCTruthClassifier fails to classify the lepton's truth type or origin), IsoElectron, ChargeFlipIsoElectron, PromptMuon, PromptPhotonConversion, ElectronFromMuon, TauDecay, BHadronDecay, CHadronDecay or LightFlavorDecay (More details [51]). Given these categories, we consider leptons classified as PromptPhotonConversion, BHadronDecay, CHadronDecay or LightFlavorDecay (i.e. a lepton originating from the decay of a  $b$ -Hadron,  $c$ -Hadron or light-flavour jet) to be fakes. We require that events which contribute to the  $(t\bar{t}Z)_{\text{fake}}$  background are those where at least one lepton from the  $t\bar{t}Z$  sample are classified by the IFF Truth Classifier with one of the four aforementioned categories.

The  $(tWZ)_{\text{fake}}$  CR aims to be as similar as possible to the  $tWZ$  SRs, but enhanced in fakes. This CR can then be used to constrain the normalisation of the  $(t\bar{t}Z)_{\text{fake}}$  template. To ensure that this region is enhanced in fakes, we require that it contains 3 tight leptons and 1 loose lepton, since loose leptons are more likely to be fakes. By using the  $p_T$  of the loose lepton ( $p_T(\text{Loose Lepton})$ ) in this region as the variable used in the fit, the shape (and normalisation) of the  $(t\bar{t}Z)_{\text{fake}}$  template can be constrained.

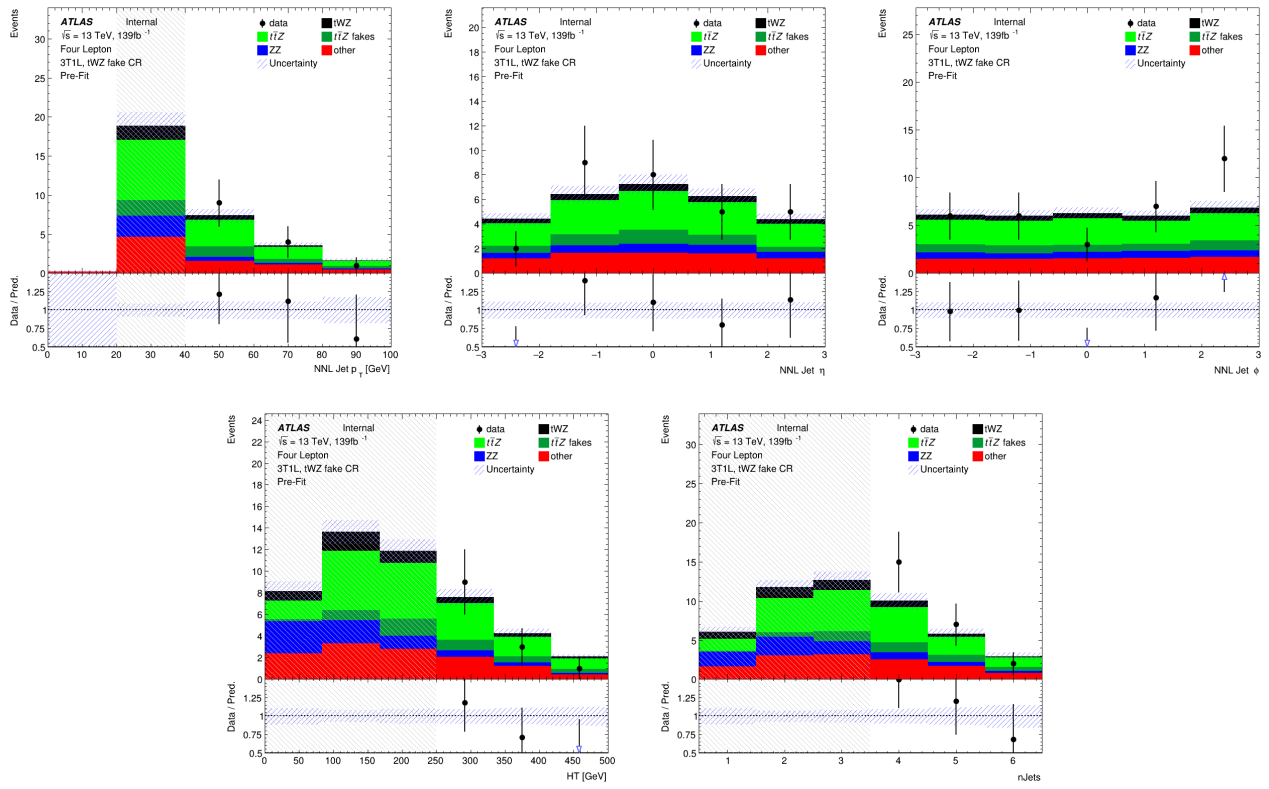


Figure 4.23: **Top row:** MC predictions for  $p_T$ ,  $\eta$  and  $\phi$  for next-to-next-to-leading (NNL) jets in the  $(tWZ)_{\text{fake}}$  CR region is shown. **Bottom row:** MC predictions for  $H_T$  (scalar sum of Jet  $p_T$ ) (left) and the Number of jets (right) in the  $(tWZ)_{\text{fake}}$  CR region is shown.

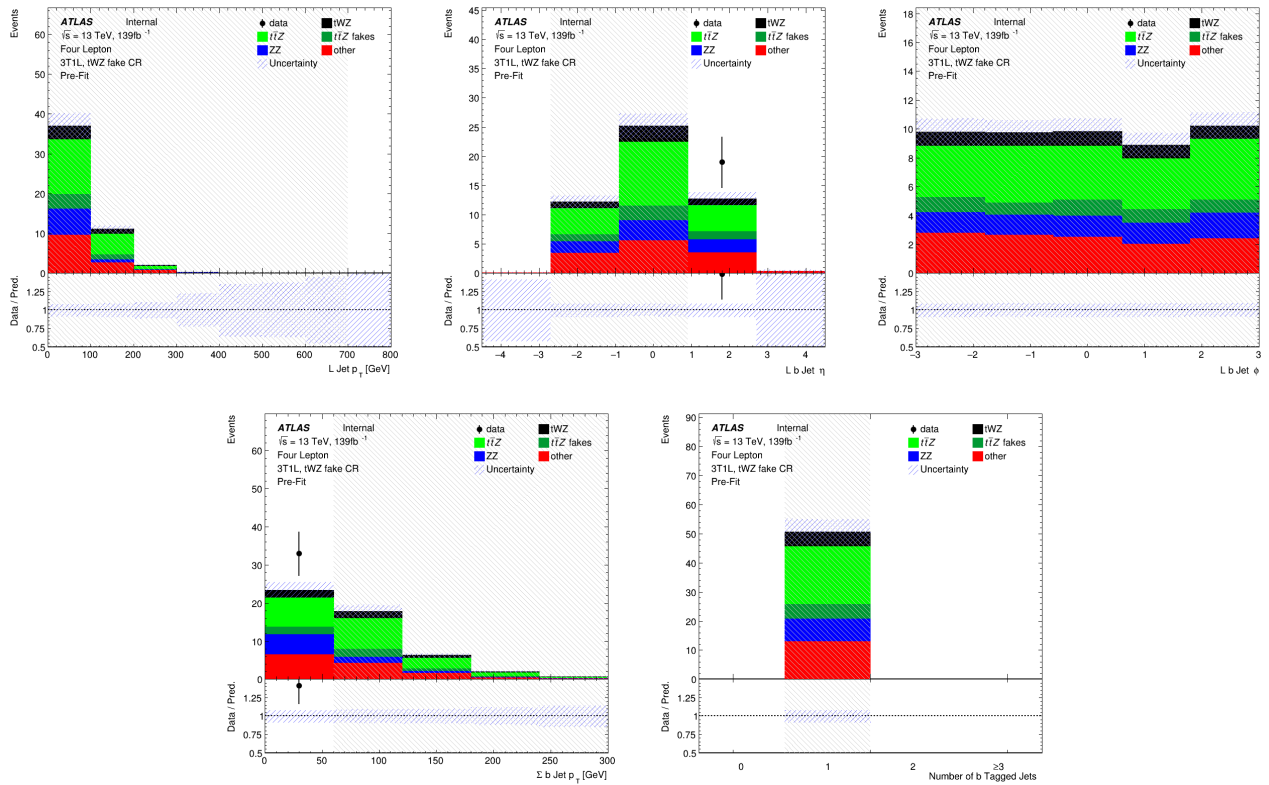


Figure 4.24: **Top row:** MC predictions for  $p_T$ ,  $\eta$  and  $\phi$  for leading b-tagged jets in the  $(tWZ)_{\text{fake}}$  CR region is shown. **Bottom row:** MC predictions for the scalar sum of b-tagged jet  $p_T$  (left) and the Number of b-tagged jets (right) in the  $(tWZ)_{\text{fake}}$  CR region is shown.

772

773 In Figure 4.25, the number of leptons classified as fake, split up by their IFF Truth classification, in each region is  
 774 shown.

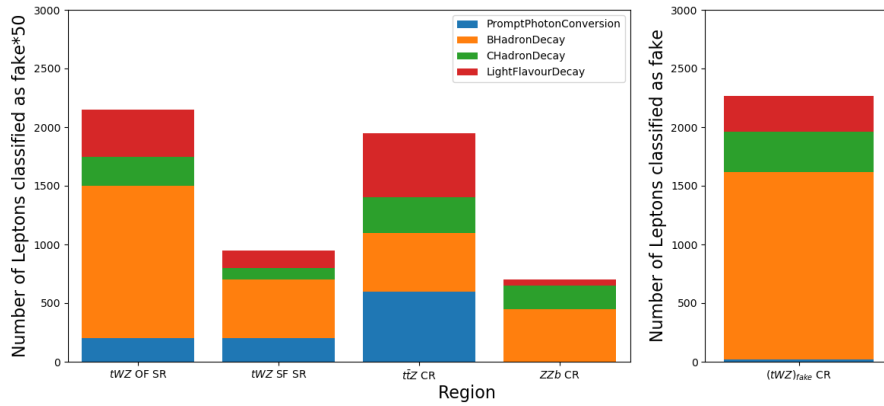


Figure 4.25: The number of leptons classified as fake, split up by their IFF Truth classification, in each region is shown. The left panel shows the number of leptons classified as fakes, scaled by a factor of 50, on the y-axis. The right panel shows the number of leptons classified as fakes (unscaled), on the y-axis. The different signal and control regions are shown on the x-axes of the left and right panels. The IFF truth classification of the leptons are shown in the legend and correspond to the different coloured stacked histograms.

775 Around 50 times more fake leptons pass our selection criteria for the  $(tWZ)_{\text{fake}}$  CR, compared to remaining four  
 776 regions. This relative abundance of fake leptons present in the  $(tWZ)_{\text{fake}}$  CR further justifies our use of this region  
 777 to constrain the fake lepton component.

778 In Figure 4.26, the relative dominance of the different classifications for fake leptons (classified by the IFF truth  
 779 classified) in each region, is shown.

780 The majority of fake leptons which pass our selection criteria originate from the decay of  $b$ -hadrons, in all regions  
 781 but the  $t\bar{t}Z$  CR. The smaller proportion of fake leptons originating from  $b$ -hadron decays in the  $t\bar{t}Z$  CR could  
 782 possibly be due to statistical fluctuations resulting from the low number of fake leptons which pass our selection  
 783 criteria in this region ( $\sim 40$  fake leptons).

784 In Figure 4.27, the amount of fake and real  $t\bar{t}Z$  events which pass our selection criteria, in each region, is shown.  
 785 Around 20% of all  $t\bar{t}Z$  events are classified as fake events (having one or more of its leptons being classified as fake)  
 786 in the  $(tWZ)_{\text{fake}}$  CR. The  $tWZ$  OF SR,  $tWZ$  SF SR,  $t\bar{t}Z$  CR and  $ZZb$  CR have less than 1% of their total  $t\bar{t}Z$   
 787 events being fake. The non-negligible amount of fake  $t\bar{t}Z$  events present in the  $(tWZ)_{\text{fake}}$  CR, allows the  $t\bar{t}Z$  fake  
 788 background to be constrained by the  $(tWZ)_{\text{fake}}$  CR.

## 791 4.7 Machine Learning Techniques

792 Now that we have our baseline selections applied and our regions defined, we implement two Boosted Decision Trees  
 793 (BDT) in order to discriminate between  $tWZ$  and our most prominent background process,  $t\bar{t}Z$  and  $ZZ$ . We chose  
 794 to use a BDT, as opposed to another ML algorithm, since they are very stable and perform well with minimal/no  
 795 optimisation or tweaking of the hyper parameters. A multi-layered sequential neural network was tried, how-  
 796 ever, it was out-performed by a BDT. More specifically, Scikit-Learn’s `GradientBoostingClassifier` [70] was used.

797 Two different BDTs were used, the first aims to discriminate between  $tWZ$  events and its major backgrounds,  
 798  $t\bar{t}Z$  and  $ZZ$ . The second aims to discriminate between  $\ell b$  systems which originate from the decay of a top quark  
 799 ( $t \rightarrow W(\rightarrow \ell\nu)b$ ) and those which do not. We refer to these two BDTs as an **event-level** and an **object-level**  
 800 classifier respectively. The discriminator output from the object-level BDT can be converted to a variable which  
 801 can then be used as input to the event-level BDT.

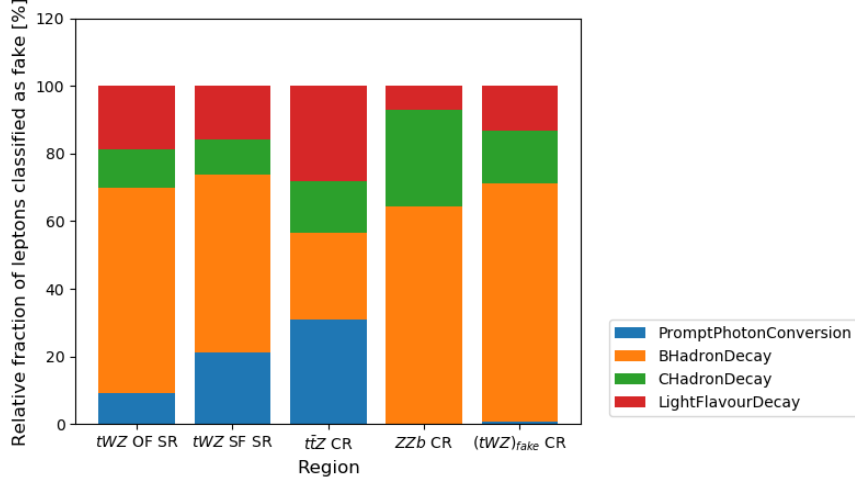


Figure 4.26: The relative dominance of the different classifications for fake leptons (classified by the IFF truth classified) in each region, is shown. The relative dominance of leptons classified as fakes, as a fraction of the total number of fake leptons (in each region), is shown on the y-axis. The different signal and control regions are shown on the x-axis. The IFF truth classification of the leptons are shown in the legend and correspond to the different coloured stacked histograms.

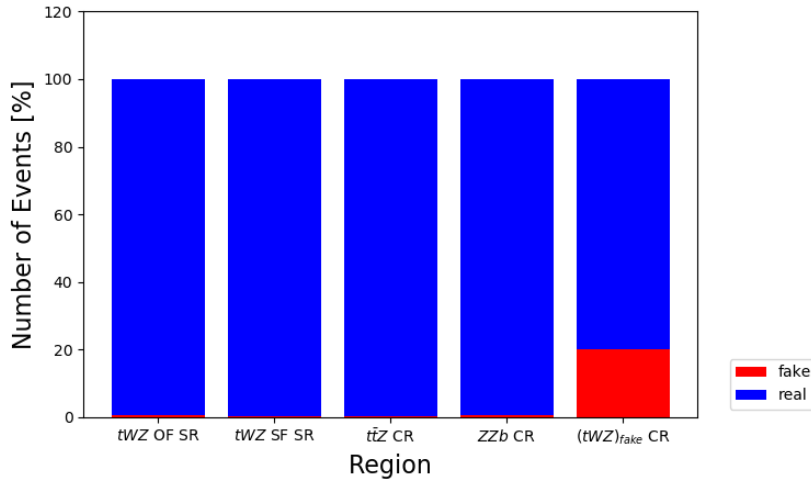


Figure 4.27: The percentage of fake and real  $t\bar{t}Z$  events which pass our selection criteria, in each region, is shown. The relative number of fake and real events (in % of the total number of events in the nominal and fake  $t\bar{t}Z$  background samples) is shown on the y-axis. The different signal and control regions are shown on the x-axis. The blue and red histograms represent the percentage of real and fake events (out of the total number of events in the nominal and fake  $t\bar{t}Z$  background samples), respectively.

### 4.7.1 Object-level BDT

The object-level BDT was trained on a  $t\bar{t}$  sample with a baseline selection of exactly 1 tight lepton with  $p_T > 28$  GeV. Additionally, jets in this sample are required to have  $p_T > 20$  GeV.  $b$ -tagged jets are identified by the 77% DL1r working point. These baseline selections were chosen to mimic those used in the event selection of the analysis (outlined in Table 4.3). We opted to use this disjoint  $t\bar{t}$  sample as to avoid resorting to use our MC samples used in the rest of the analysis which is heavily limited on statistics, therefore maximizing the amount of MC statistics used in the fitting procedure and the training of the event-level BDT.

The signal class is defined to consist of reconstructed  $\ell b$  systems (defined as the sum of the 4-vectors of the lepton and  $b$ -jet) coming from top quarks which are well matched to their truth counterparts. In particular, we require that  $\Delta R$  between the reconstructed and truth  $\ell b$  system is less than 0.05. We additionally require that the reconstructed lepton and the truth top have charges with the same sign (since  $t \rightarrow b\ell^+\bar{\nu}_\ell$  and  $\bar{t} \rightarrow \bar{b}\ell^-\nu_\ell$ ). The background class is defined to consist of all reconstructed  $\ell b$  systems which fail to pass the criteria for  $\ell b$  systems which are labelled as signal. These definitions for the signal and background classes ensure that the signal class consists of mostly  $\ell b$  systems originating from tops and the background class consists of mostly  $\ell b$  systems which do not originate from a top decay.

Different observables corresponding to an  $\ell b$  system were used as input to training. The optimum values for the hyper-parameters used were determined by training the BDT with a range of different values for the hyper-parameters and choosing the set of values which maximized the mean accuracy (based off 5 fold kfold cross-validation). This method is more commonly referred to as hyper-parameter optimisation or tuning. After hyper-parameter optimisation, the mean accuracy of each fold increased from 0.76 to 0.77 ( $\sim 1\%$  increase). Input features can be assigned a score called *variable importance*, based on their usefulness on predicting a target variable (in this case, a signal or background event). The variable importance for any given variable was obtained by computing the mean accuracy of the model, removing the variable from training, retraining the model and computing the mean accuracy of this new model. The difference between mean accuracies of the unaltered model and the retrained model (after removal of the variable) gives us the variable importance of the variable of interest. This method returns positive values for variables which increase the mean accuracy of the model and negative values for variables which decrease the mean accuracy of the model. Variables with negative variable importances were completely removed from training.

In Table 4.6, the variables used in training the object-level BDT are shown.

Observable	Description
$m(\ell b)$	Invariant mass of the $\ell b$ system
$p_T(\ell b)$	$p_T$ of the $\ell b$ system
$\Delta\eta(\ell, b)$	$\Delta\eta$ between the $\ell$ and $b$ -tagged jet
$\Delta\phi(\ell, b)$	$\Delta\phi$ between the $\ell$ and $b$ -tagged jet
$\Delta R(\ell, b)$	$\Delta R$ between the $\ell$ and $b$ -tagged jet

Table 4.6: A list of the observables used in the object-level BDT, ordered by importance (descending, top to bottom) is shown.

In Figure 4.28, normalised distributions of the signal and background classes for the training set of all variables used in the object-level BDT are shown.

Overall the BDT input variables show a large amount of discrimination.

We can check the modelling of the input variables to the object-level BDT by studying the agreement between data and simulation in the  $t\bar{t}Z$  CR. In Figure 4.29, MC predictions for the input variables to the object-level BDT in the  $t\bar{t}Z$  CR are shown.

Overall, there is good agreement between data and simulation for the input variables to the object-level BDT in the  $t\bar{t}Z$  CR. This suggests that the input variables to the object-level BDT are well-modelled and are reasonable to include as inputs to the object-level BDT.

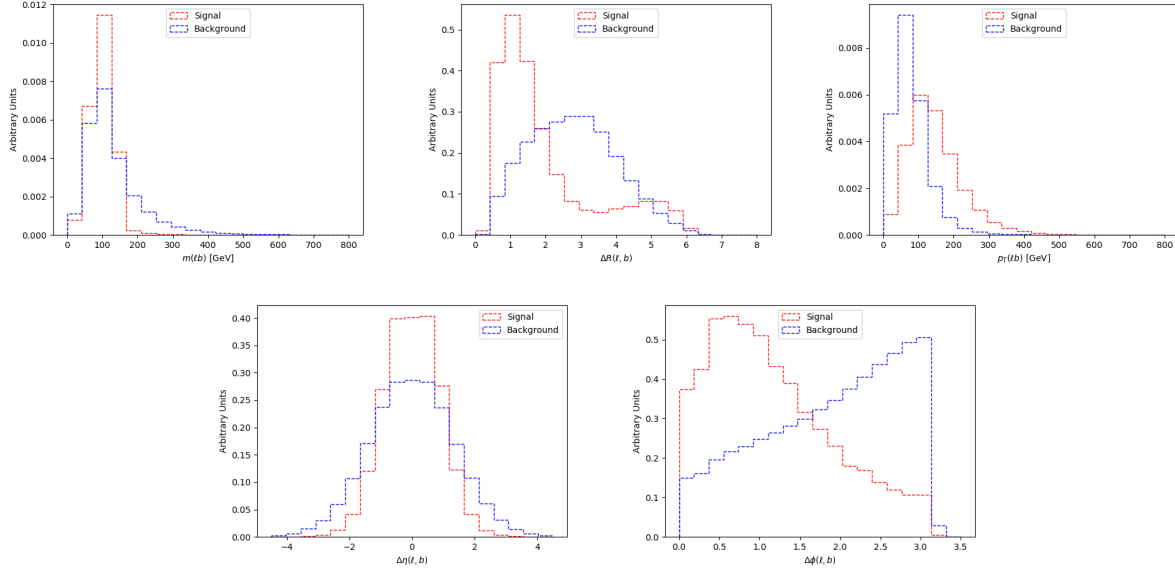


Figure 4.28: Normalised distributions of the signal and background classes for the training set of all variables used in the object-level BDT (ordered from top left to bottom right via decreasing importance) are shown. The red and blue dotted lined histograms represent the signal and background classes events (normalised to an area of 1), respectively. The variable used in training is shown on the x-axis. The y-axis shows the relative number of events for the signal and background classes (in arbitrary units). **From top left to bottom right:** Invariant mass of the  $lb$  system.  $\Delta R$  between the  $l$  and  $b$ -tagged jet. The  $p_T$  of the  $lb$  system.  $\Delta\eta$  between the  $l$  and  $b$ -tagged jet.  $\Delta\phi$  between the  $l$  and  $b$ -tagged jet.

846 A final check can be done to study the similarity of the  $lb$  systems present in the alternative  $t\bar{t}$  sample which we use  
 847 for training the object-level BDT, and the  $lb$  systems which we aim to identify using the object-level BDT. More  
 848 specifically, we want to ensure that the  $lb$  systems in the alternative  $t\bar{t}$  sample are similar enough to those in the  
 849  $tWZ$  and  $t\bar{t}Z$  samples (see Table 4.1). In Figure 4.30, normalised distributions of input variables to the object-level  
 850 BDT in the alternative  $t\bar{t}$ ,  $tWZ$  and  $t\bar{t}Z$  samples, are shown.  
 851 The distributions of the input variables to the object-level classifier, for the three samples, are similar and show no  
 852 large deviations between one another. This tells us that the  $lb$  systems which we use in training are similar enough  
 853 to those we aim to identify using the classifier. The use of the alternative  $t\bar{t}$  sample for training the object-level  
 854 classifier is therefore sufficient for this analysis.

855

In Table 4.7, the hyper-parameters used in the object-level BDT is shown.

Hyper-parameter	Value	Description
loss	deviance	The loss function to be optimised
criterion	friedman_mse	The function used to measure the quality of a split
n_estimators	200	The number of boosting stages to perform
learning_rate	0.1	The step size at each iteration during optimisation
max_depth	6	The maximum depth of the individual regression estimators
min_samples_split	2	The minimum number of samples (events) required to split an internal node
min_samples_leaf	1	The minimum number of samples (events) required to be at a leaf node
validation_fraction	0.1	The proportion of training data to set aside as validation set for early stopping
n_iter_no_change	20	Training terminates when the validation score (determined by the validation set) does not improve in all of the previous

Table 4.7: A list of the hyper-parameters used in the object-level BDT is shown. Hyperparameters not listed in this table use the default values as stated in the Scikit-learn Documentation[71].

856

857 The number of events used in training for the signal and background classes were 49871 and 384152 respectively.  
 858 Imbalanced datasets can cause ML classifiers to ignore small classes while concentrating on classifying large classes  
 859 more accurately, which may result in the trained classifier performing sub-optimally. In order to correct this dataset  
 860 imbalance, we ensure that the relative weighting of each event is such that the sum of the signal weights is equal  
 861 to the sum of the background weights. In Figure 4.31 the normalised histograms of the training and test sets

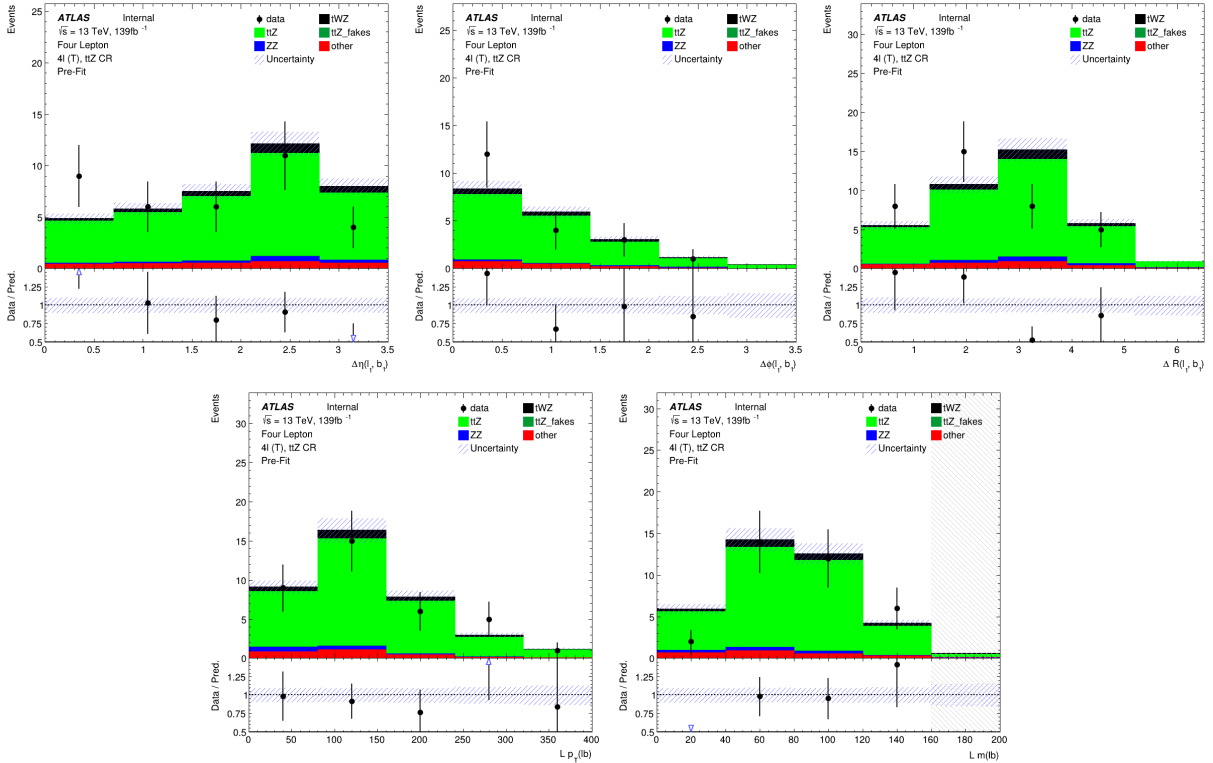


Figure 4.29: Pre-fit distributions of variables used as input to the object-level BDT (ordered from top left to bottom right via decreasing importance), in the  $t\bar{t}Z$  CR, are shown. The data is given by the black points and the MC predictions for each process are given by the histograms. The vertical lines on the data points represent the total uncertainty in the data and the blue diagonal lined bands represent the total MC uncertainty. The lower panel in each plot shows the ratios of the data to the theoretical predictions. Bins with a  $\frac{\text{signal}}{\text{background}}$  yield greater than 0.1 are kept blinded. Blinded bins are shaded with black diagonal lines and their data points are omitted. **From top left to bottom right:**  $\Delta\eta$  between the lepton and  $b$ -jet of the leading  $\ell b$  system.  $\Delta\phi$  between the lepton and  $b$ -jet of the leading  $\ell b$  system.  $\Delta R$  between the lepton and  $b$ -jet of the leading  $\ell b$  system.  $p_T$  of the leading  $\ell b$  system. Mass of the leading  $\ell b$  system.

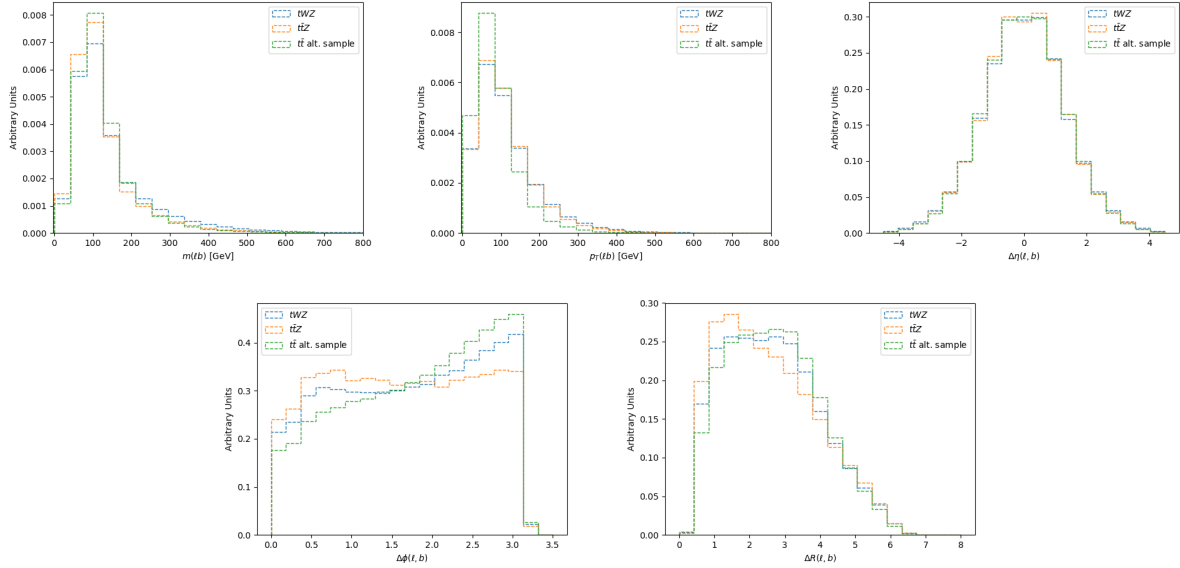


Figure 4.30: Normalised distributions of input variables (ordered from top left to bottom right via decreasing importance) to the object-level BDT in the alternative  $t\bar{t}$ ,  $tWZ$  and  $t\bar{t}Z$  samples, are shown. The green, blue and orange dotted lined histograms represent events from the alternative  $t\bar{t}$ ,  $tWZ$  and  $t\bar{t}Z$  samples (normalised to an area of 1), respectively. The variable used in training is shown on the x-axis. The y-axis shows the relative number of events (in arbitrary units). **From top left to bottom right:** Invariant mass of the  $\ell b$  system.  $\Delta R$  between the  $\ell$  and  $b$ -tagged jet. The  $p_T$  of the  $\ell b$  system.  $\Delta\eta$  between the  $\ell$  and  $b$ -tagged jet.  $\Delta\phi$  between the  $\ell$  and  $b$ -tagged jet.

862 (extracted from fold 5 from a 5 fold kfold cross validation) for signal and background is shown.

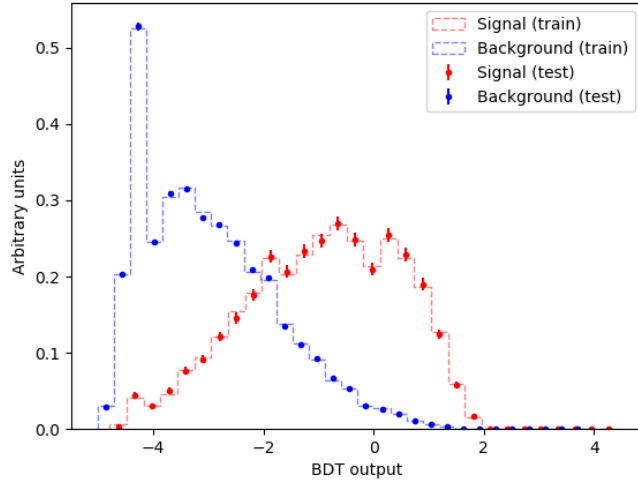


Figure 4.31: Normalised histograms of the object-level BDT discriminator output from the signal and background classes for the training and test sets from the 5th fold in a 5 fold kfold cross validation is shown. The output of the object-level BDT is shown on the x-axis and the relative number of events (in arbitrary units) is shown on the y-axis. The training set for the signal class is shown by the red dotted histogram. The test set for the signal class is shown by the red points, with the total uncertainty represented by the vertical error bars. The training set for the background class is shown by the blue dotted histogram. The test set for the background class is shown by the blue points, with the total uncertainty represented by the vertical error bars.

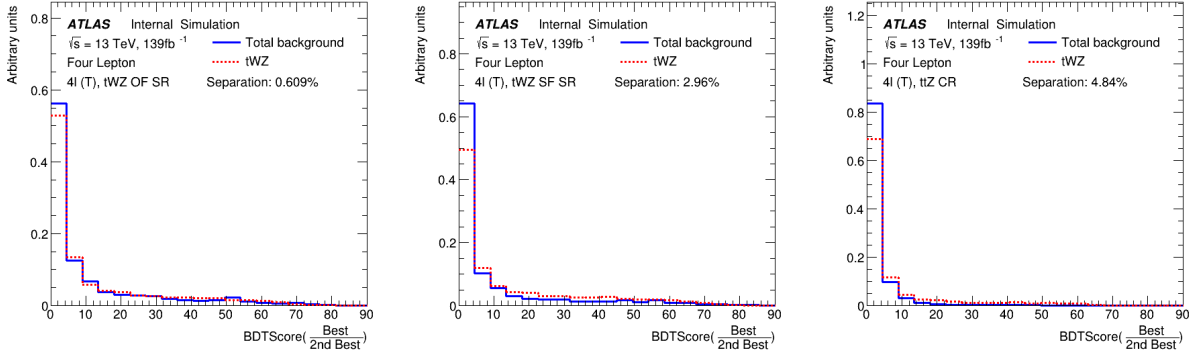


Figure 4.32: Normalised distributions of the signal and total background of the  $\text{BDTScore}(\frac{\text{Best}}{\text{2nd Best}})$  variable in the  $tWZ$  OF SR,  $tWZ$  SF SR and  $t\bar{t}Z$  CR are shown (left to right). The dotted red and solid blue lines represent the distributions (normalised to an area of 1) of the signal and total background events respectively. The x-axis shows the  $\text{BDTScore}(\frac{\text{Best}}{\text{2nd Best}})$  and the y-axis show the relative number of events (in arbitrary units).

We can see that the shapes of the training and test sets for both signal and background are very similar. This is a good indicator that no over-training occurred. Another over-training check is performed using 5 fold kfold cross validation. We ensure that the variance of the mean accuracy of each folds' test set in cross validation is substantially small. This indicates that fluctuations in features from different training sets are not learnt by the classifier. For the object-level classifier, a variance of  $3.24 \times 10^{-7}$  was calculated for the mean accuracies of each folds' test set in cross validation, providing further evidence that no over-training occurred.

The output from the object-level BDT was used to construct a variable to be used as input to the event-level BDT. The event-level BDT aims to discriminate between  $tWZ$  and our most prominent background,  $t\bar{t}Z$ . We therefore aim to construct a variable from the output of the object-level BDT which discriminates well between  $tWZ$  and  $t\bar{t}Z$ . Since  $tWZ$  events contain one top quark and  $t\bar{t}Z$  events contain two top quarks, we expect that  $tWZ$  events have one  $\ell b$  combination which scores well and we expect that  $t\bar{t}Z$  events have two  $\ell b$  combinations which score well. We construct a variable,  $\text{BDTScore}(\frac{\text{Best}}{\text{2nd Best}})$ , which takes the ratio of the scores of the top scoring  $\ell b$  system to the 2nd best scoring  $\ell b$  system. We expect this variable to be large for  $tWZ$  events and closer to one for  $t\bar{t}Z$  events, therefore providing discrimination between  $tWZ$  and  $t\bar{t}Z$ .

In Figure 4.32, normalised distributions of the signal and total background of the  $\text{BDTScore}(\frac{\text{Best}}{\text{2nd Best}})$  variable in the  $tWZ$  OF SR,  $tWZ$  SF SR and  $t\bar{t}Z$  CR are shown.

There doesn't seem to be a large amount of discrimination between signal and background for  $\text{BDTScore}(\frac{\text{Best}}{\text{2nd Best}})$  in either of the above regions. We do however see some discrimination in bins near a value of 1, where the number of background events exceed the number of signal events, which is what we expect. This effect is slightly more exaggerated in the  $t\bar{t}Z$  CR than the  $tWZ$  SRs. This can be explained since we expect to have a larger proportion of  $t\bar{t}Z$  events (events with two  $\ell b$  systems) in the  $t\bar{t}Z$  CR. An excess of signal events (compared to background) are observed at larger values. This is to be expected, since these events correspond to a lower score by the  $\ell b$  classifier on the 2nd best scoring  $\ell b$  system in the event. The 2nd best scoring  $\ell b$  system in a  $tWZ$  event is expected to be low, since there is only one  $\ell b$  system originating from a top. Despite the apparent lack of discrimination between signal and background events from this variable, when used as input to training in the event-level BDT (see Section 4.7.2), improves the mean accuracy of the classifier. This tells us that the event-level BDT is taking advantage of the discrimination between signal and background present in the  $\text{BDTScore}(\frac{\text{Best}}{\text{2nd Best}})$  variable.

In an attempt to optimise the performance of the object-level BDT, we aim to train on signal events which are as pure in  $\ell b$  systems originating from top quarks, as possible. Similarly, we aim to train on background events which are as pure in  $\ell b$  systems not originating from top quarks, as possible. This is done by studying the distribution of  $\Delta R$  between the reconstructed  $\ell b$  system and the truth  $\ell b$  system ( $\Delta R((lb)_{reco}, (lb)_{truth})$ ), and excluding  $\ell b$  systems from training which are moderately matched in  $\Delta R$  to their truth counterparts, leaving well matched  $\ell b$  systems being labelled as signal and badly matched  $\ell b$  systems labelled as background. We call the  $\Delta R$  range where  $\ell b$  systems are excluded from training, the exclusion region. In Figure 4.33, the distribution of  $\Delta R$  between the reconstructed  $\ell b$  system and the truth  $\ell b$  system ( $\Delta R((lb)_{reco}, (lb)_{truth})$ ) in the alternative  $t\bar{t}$  sample, along with

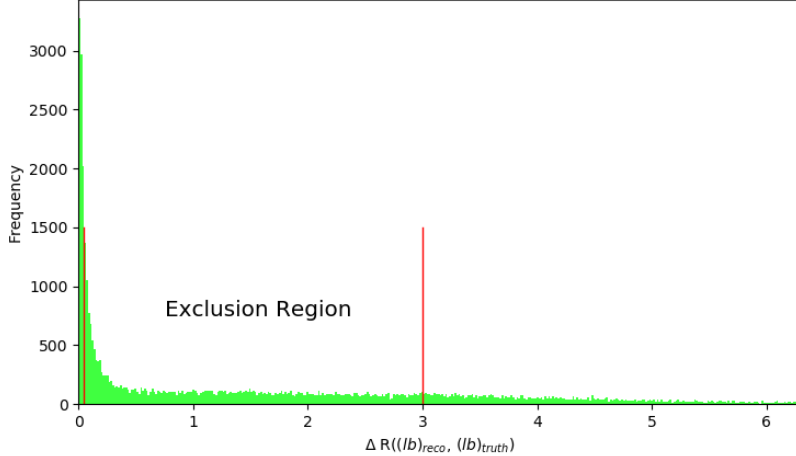


Figure 4.33: The distribution of  $\Delta R$  between the reconstructed  $\ell b$  system and the truth  $\ell b$  system ( $\Delta R((lb)_{reco}, (lb)_{truth})$ ) in the alternative  $t\bar{t}$  sample, along with the exclusion region, is shown. The  $\Delta R$  distribution is shown in green.  $\Delta R$  between the reconstructed  $\ell b$  system and the truth  $\ell b$  system ( $\Delta R((lb)_{reco}, (lb)_{truth})$ ) is shown on the x-axis. The bin frequency is shown on the y-axis. The exclusion region is shown between the vertical red lines situated at  $\Delta R((lb)_{reco}, (lb)_{truth}) = 0.05$  and  $\Delta R((lb)_{reco}, (lb)_{truth}) = 3.0$ . Reconstructed  $\ell b$  systems with  $\Delta R((lb)_{reco}, (lb)_{truth}) \leq 0.05$  are labelled as signal and reconstructed  $\ell b$  systems with  $\Delta R((lb)_{reco}, (lb)_{truth}) \geq 3.0$  are labelled as background.

901 the exclusion region, is shown.  
 902 A large number of reconstructed  $\ell b$  systems have  $\Delta R((lb)_{reco}, (lb)_{truth})$  at values near 0. These are matched (in  
 903  $\Delta R$ ) extremely well to truth  $\ell b$  systems originating from top quarks. We therefore define our exclusion region  
 904 to be between  $0.05 < \Delta R((lb)_{reco}, (lb)_{truth}) < 3.0$ , such that all reconstructed  $\ell b$  systems with  $\Delta R((lb)_{reco}, (lb)_{truth}) \leq 0.05$  are labelled as signal and reconstructed  $\ell b$  systems with  $\Delta R((lb)_{reco}, (lb)_{truth}) \geq 3.0$  are labelled as background. All reconstructed  $\ell b$  systems with  $0.05 < \Delta R((lb)_{reco}, (lb)_{truth}) < 3.0$  are excluded from training.  
 907  
 908 The performance of the object-level BDT with and without the exclusion region can be compared by studying  
 909 the discrimination between signal and background events in the  $BDTScore(\frac{\text{Best}}{2nd \text{ Best}})$  variable (object-level output  
 910 converted to an event-level variable to be used in the event-level BDT) for both object-level BDTs. In Figure 4.34,  
 911 normalised distributions of  $BDTScore(\frac{\text{Best}}{2nd \text{ Best}})$  using the object-level BDT without the exclusion region (see Fig-  
 912 ure 4.33) for the  $tWZ$  OF SR,  $tWZ$  SF SR and  $t\bar{t}Z$  CR are shown.  
 913 The amount of discrimination can be quantified by the separation metric, which gives the percentage of the total  
 914 area of the distributions which do not overlap. A value of 1 indicates that the distributions are fully separated (no  
 915 overlap) and a value of 0 indicates that the distributions have no separation (fully overlapped). We can compare  
 916 the separation metrics between the  $BDTScore(\frac{\text{Best}}{2nd \text{ Best}})$  variable in the  $tWZ$  OF SR,  $tWZ$  SF SR and  $t\bar{t}Z$  CR for  
 917 the  $\ell b$  classifier with (Figure 4.32) and without (Figure 4.34) the exclusion region by taking the absolute difference  
 918 between the two values in each region. The differences are 0.31%, 0.37% and 0.36% for the  $tWZ$  OF SR,  $tWZ$  SF  
 919 SR and  $t\bar{t}Z$  CR, respectively. These differences are minimal and the object-level BDT with the exclusion region  
 920 outperforms the object-level BDT without the exclusion region in the  $tWZ$  SF SR. Due to the small differences in  
 921 performance between the two BDTs, for simplicity, we ultimately chose to keep the BDT with the exclusion region.

## 922 4.7.2 Event-level BDT

923 The event-level BDT was trained on 50% of the  $tWZ$  MC sample's events for the signal class and similarly,  
 924 50% of the  $t\bar{t}Z$  and  $ZZ$  MC sample's events were used for the background class. The samples we train on are  
 925 individual events, with the features being carefully chosen observables. These observables are chosen on the basis  
 926 that they are somewhat uncorrelated from one another and show a relatively large amount of separation power  
 927 between  $tWZ$  and  $t\bar{t}Z$ . Similarly to the object-level BDT, the optimum values for the hyper-parameters used  
 928 were determined via hyper-parameter optimisation. After hyperparameter optimisation, the mean accuracy of  
 929 each fold (determined from 5 fold kfold cross validation) increased from 0.72 to 0.74 ( $\sim 3\%$  increase). The variable

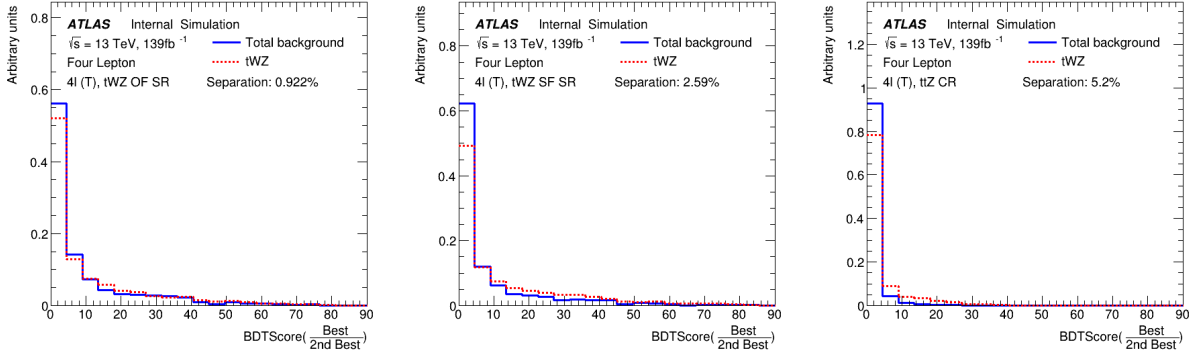


Figure 4.34: Normalised distributions of  $\text{BDTScore}(\frac{\text{Best}}{\text{2nd Best}})$  using the object-level BDT without the exclusion region (see Figure 4.33) for the  $tWZ$  OF SR,  $tWZ$  SF SR and  $t\bar{Z}$  CR are shown (left to right). The dotted red and solid blue lines represent the distributions (normalised to an area of 1) of the signal and total background events respectively. The x-axis shows the  $\text{BDTScore}(\frac{\text{Best}}{\text{2nd Best}})$  and the y-axis show the relative number of events (in arbitrary units).

importance of each variable was computed in the same way as described for the object-level BDT (See Section 4.7.1).

930

In Table 4.8, the variables used in training the event-level BDT are shown.

Observable	Description
$2\nu\text{SM}$	Maximum weight from the $2\nu\text{SM}$ algorithm (See Section 4.8)
$HT$	Scalar sum of jet $p_T$
$LT$	Scalar sum of lepton $p_T$
$\sum p_T(b - \text{jet})$	Scalar sum of $b$ -tagged jet $p_T$
$\text{BDTScore}(\frac{\text{Best}}{\text{2nd Best}})$	Ratio of the top scoring $\ell b$ system to the 2nd best scoring $\ell b$ system from the output of the object-level BDT ( $\ell b$ classifier)
$\Delta\eta(\ell_{1,\text{Non-}Z}, \ell_{2,\text{Non-}Z})$	$\Delta\eta$ between the two leptons, not coming from a $Z$ candidate

Table 4.8: A list of the observables used in the event-level BDT, ordered by importance (descending, top to bottom) is shown.

932

In Figure 4.35, normalised distributions of the signal and background classes for the training set of all variables used in the event-level BDT are shown.

933

Overall the BDT input variables show a reasonable amount of discrimination. In particular the output weight from the  $2\nu\text{SM}$  algorithm shows the most discrimination. When determining which variables to use in training the event-level BDT, the output weight from  $2\nu\text{SM}$  was shown to provide the most sizeable boost in performance of the BDT. Surprisingly, the least important variable,  $\Delta\phi$  between the non- $Z$  lepton system (leptons not originating from a  $Z$ -candidate) and the leading  $b$ -tagged jet, seem to discriminate well between signal and background. A possible explanation for its low ranking importance is due to it being relatively highly correlated with many of the other input variables.

942

We can check the modelling of the input variables to the event-level BDT by referring to the pre-fit distributions of data and simulation in the control regions. Note that certain variables which are ill-defined in certain regions (e.g.  $\Delta\eta(\ell_{1,\text{Non-}Z}, \ell_{2,\text{Non-}Z})$ ) in the  $ZZb$  CR, as all leptons originate from a  $b$ -jet in this region) will not be shown.

946

In Figure 4.36, MC predictions for the input variables to the event-level BDT in the  $t\bar{Z}$  CR are shown.

948

In Figure 4.37, MC predictions for the input variables to the event-level BDT in the  $ZZb$  CR are shown.

949

In Figure 4.38, MC predictions for the input variables to the event-level BDT in the  $(tWZ)_{\text{fake}}$  CR are shown.

950

Overall, the agreement between data and simulation for the input variables to the event-level BDT is good.

951

Therefore, these variables are well-modelled and reasonable to include as inputs to the event-level BDT.

952

In Table 4.9, the hyper-parameters used in the event-level BDT are shown.

954

Since we are training on  $t\bar{Z}$  and  $ZZ$  events for the background class, we ensure that the relative weighting of these

955

events are such that they mimic the amount of  $t\bar{Z}$  and  $ZZ$  expected to be present in the regions where we aim to

956

use the BDT discriminator ( $tWZ$  SRs and  $t\bar{Z}$  CR). This is done by applying normalization weights to each event,

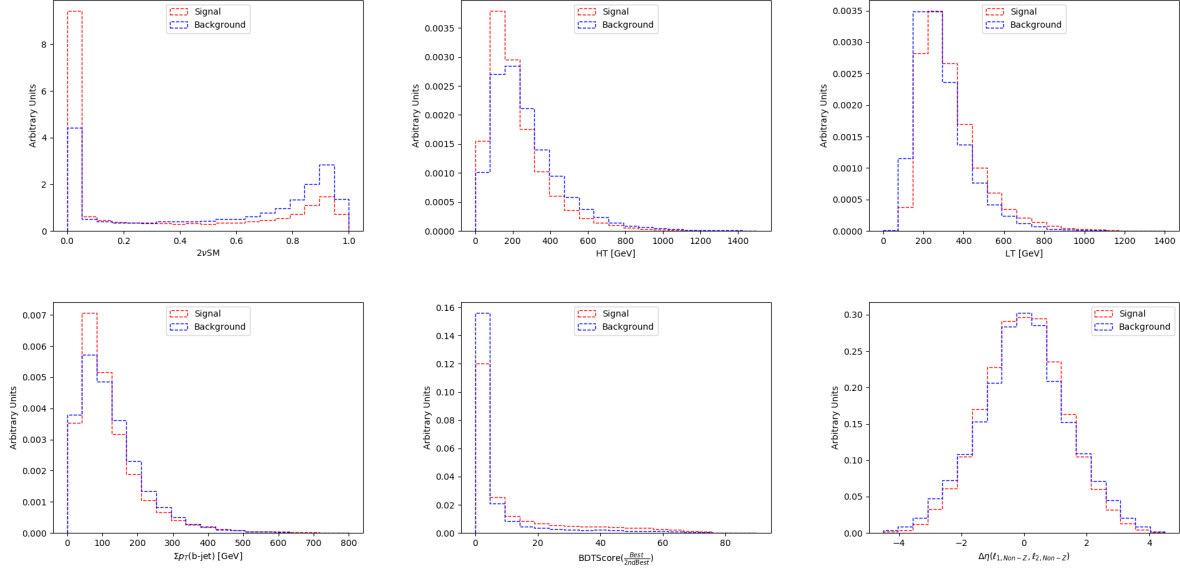


Figure 4.35: Normalised distributions of the signal and background classes for the training set of all variables used in the event-level BDT (ordered from top left to bottom right via decreasing importance) are shown. The red and blue dotted lined histograms represent the signal and background classes events (normalised to an area of 1), respectively. The variable used in training is shown on the x-axis. The y-axis shows the relative number of events for the signal and background classes (in arbitrary units). **From top left to bottom right:** Output weight from the  $2\nu\text{SM}$  algorithm (See Section 4.8). Scalar sum of jet  $p_T$ . Scalar sum of lepton  $p_T$ . Sum of  $b$ -tagged jet  $p_T$ . Ratio of the top scoring  $\ell b$  system to the 2nd best scoring  $\ell b$  system from the output of the object-level BDT (See Section 4.7.1).  $\Delta\eta$  between the two leptons, not coming from a  $Z$  candidate.

Hyper-parameter	Value	Description
loss	deviance	The loss function to be optimised
criterion	friedman_mse	The function used to measure the quality of a split
n_estimators	200	The number of boosting stages to perform
learning_rate	0.1	The step size at each iteration during optimisation
max_depth	6	The maximum depth of the individual regression estimators
min_samples_split	2	The minimum number of samples (events) required to split an internal node
min_samples_leaf	1	The minimum number of samples (events) required to be at a leaf node
validation_fraction	0.1	The proportion of training data to set aside as validation set for early stopping
n_iter_no_change	20	Training terminates when the validation score (determined by the validation set) does not improve in all of the previous

Table 4.9: A list of the hyper-parameters used in the event-level BDT is shown. Hyperparameters not listed in this table use the default values as stated in the Scikit-learn Documentation[71].

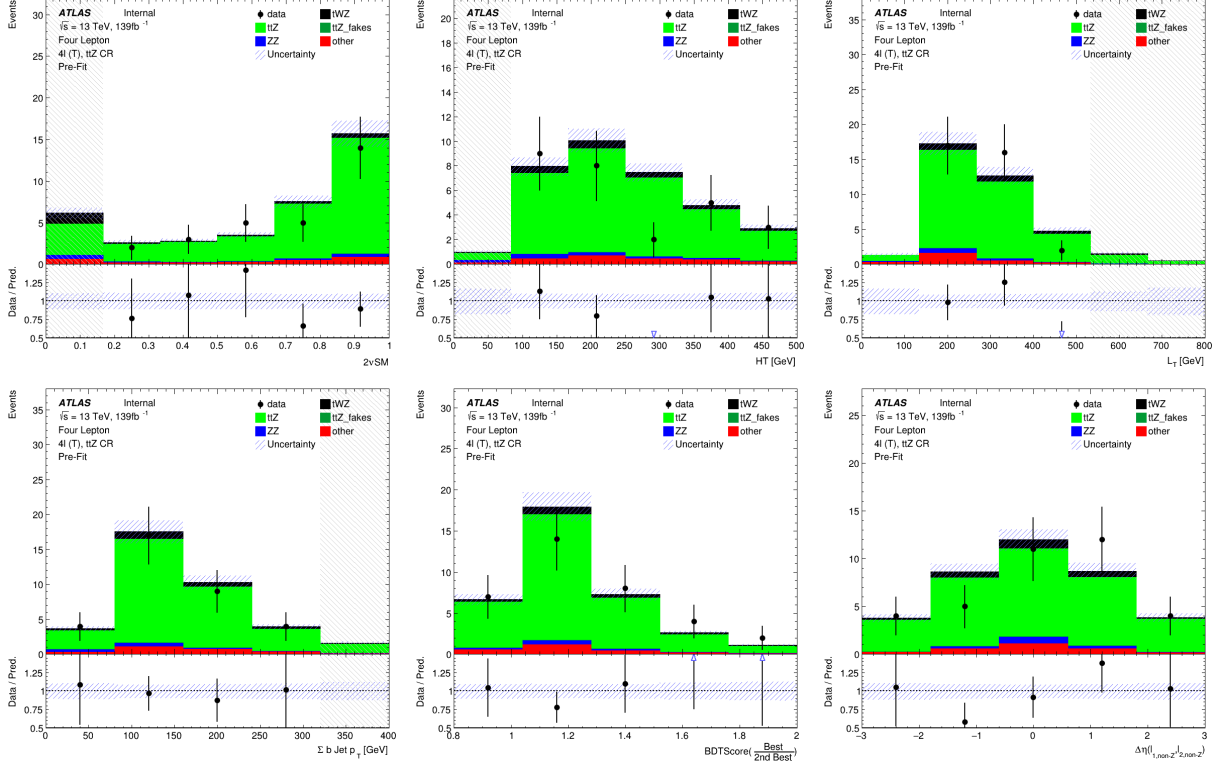


Figure 4.36: Pre-fit distributions of variables used as input to the event-level BDT (ordered from top left to bottom right via decreasing importance), in the  $t\bar{t}Z$  CR, are shown. The data is given by the black points and the MC predictions for each process are given by the histograms. The vertical lines on the data points represent the total uncertainty in the data and the blue diagonal lined bands represent the total MC uncertainty. The lower panel in each plot shows the ratios of the data to the theoretical predictions. Bins with a  $\frac{\text{signal}}{\text{background}}$  yield greater than 0.1 are kept blinded. Blinded bins are shaded with black diagonal lines and their data points are omitted. **From top left to bottom right:** Output weight from the  $2\nu\text{SM}$  algorithm (See Section 4.8). Scalar sum of jet  $p_T$ . Scalar sum of lepton  $p_T$ . Sum of  $b$ -tagged jet  $p_T$ . Ratio of the top scoring  $\ell b$  system to the 2nd best scoring  $\ell b$  system from the output of the object-level BDT (See Section 4.7.1).  $\Delta\eta$  between the two leptons, not coming from a  $Z$  candidate.

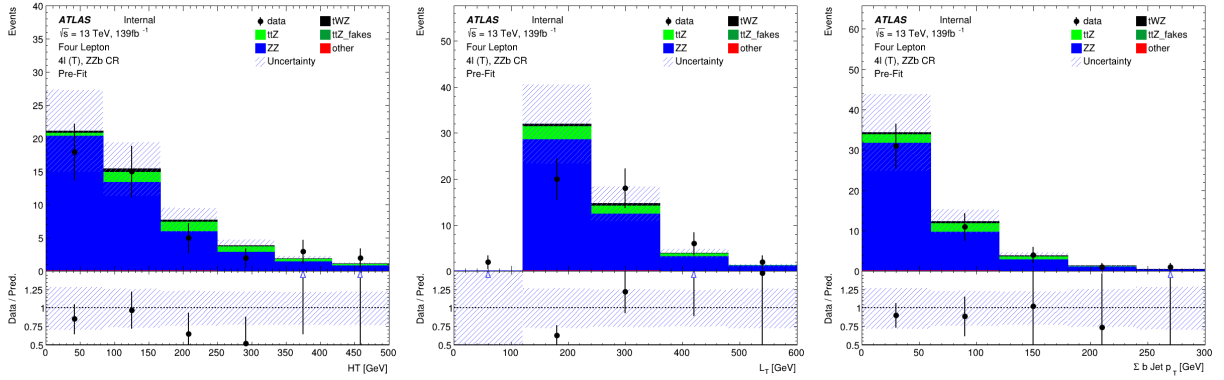


Figure 4.37: Pre-fit distributions of variables used as input to the event-level BDT (ordered from top left to bottom right via decreasing importance), in the  $ZZb$  CR, are shown. The data is given by the black points and the MC predictions for each process are given by the histograms. The vertical lines on the data points represent the total uncertainty in the data and the blue diagonal lined bands represent the total MC uncertainty. The lower panel in each plot shows the ratios of the data to the theoretical predictions. Bins with a  $\frac{\text{signal}}{\text{background}}$  yield greater than 0.1 are kept blinded. Blinded bins are shaded with black diagonal lines and their data points are omitted. **From left to right:** Scalar sum of jet  $p_T$ . Scalar sum of lepton  $p_T$ . Sum of  $b$ -tagged jet  $p_T$ .

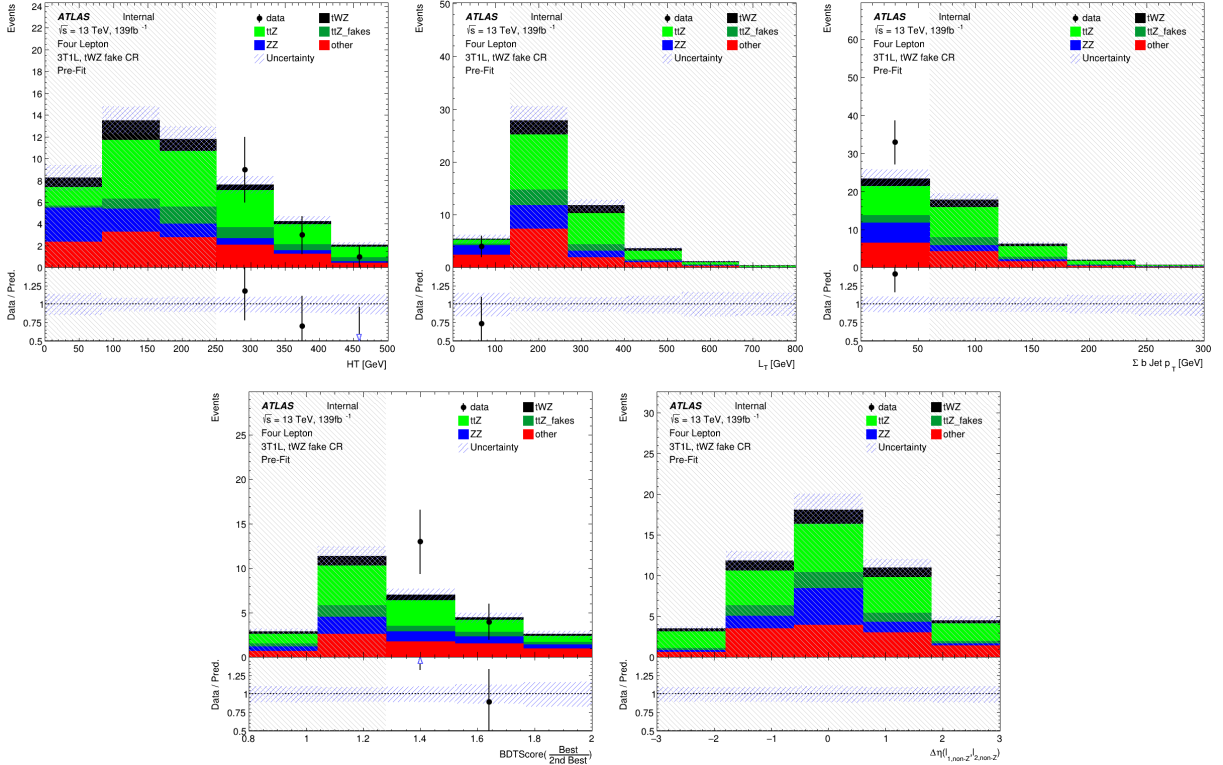


Figure 4.38: Pre-fit distributions of variables used as input to the event-level BDT (ordered from top left to bottom right via decreasing importance), in the  $(tWZ)_{\text{fake}}$  CR, are shown. The data is given by the black points and the MC predictions for each process are given by the histograms. The vertical lines on the data points represent the total uncertainty in the data and the blue diagonal lined bands represent the total MC uncertainty. The lower panel in each plot shows the ratios of the data to the theoretical predictions. Bins with a  $\frac{\text{signal}}{\text{background}}$  yield greater than 0.1 are kept blinded. Blinded bins are shaded with black diagonal lines and their data points are omitted. **From top left to bottom right:** Output weight from the  $2\nu\text{SM}$  algorithm (See Section 4.8). Scalar sum of jet  $p_T$ . Scalar sum of lepton  $p_T$ . Sum of  $b$ -tagged jet  $p_T$ . Ratio of the top scoring  $\ell b$  system to the 2nd best scoring  $\ell b$  system from the output of the object-level BDT (See Section 4.7.1).  $\Delta\eta$  between the two leptons, not coming from a  $Z$  candidate.

957 defined as,

$$W = \frac{\sigma \mathcal{L} \text{weight(MC)}}{\text{totalWeight(MC)}} \quad (4.2)$$

958 where  $\sigma$  is the cross section of the process,  $\mathcal{L}$  is the integrated luminosity,  $\text{weight(MC)}$  is the weight assigned to  
959 the event by the MC generator and  $\text{totalWeight(MC)}$  is the sum of those weights for all the generated events.

960 The number of events used in training for the signal and background classes were 41066 and 22608 respectively.  
961 Similarly to the object-level BDT, there is a dataset imbalance. We correct this imbalance (in the same way as  
962 before with the object-level BDT) by ensuring that the relative weighting of each event is such that the sum of the  
963 signal weights is equal to the sum of the background weights.

964 In Figure 4.40 the normalised histograms of the training and test sets (extracted from fold 5 from a 5 fold kfold  
965 cross validation) for signal and background is shown.

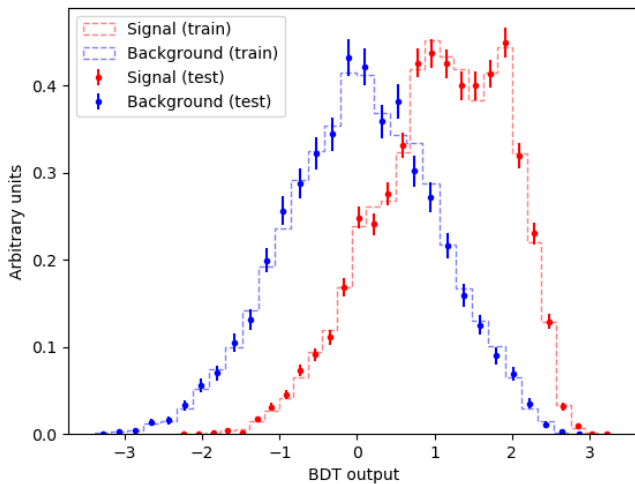


Figure 4.39: Normalised histograms of the event-level BDT discriminator output from the signal and background classes for the training and test sets from the 5th fold in a 5 fold kfold cross validation are shown. The output of the event-level BDT is shown on the x-axis and the relative number of events (normalised to have an area of 1, in arbitrary units) is shown on the y-axis. The training set for the signal class is shown by the red dotted histogram. The test set for the signal class is shown by the red points, with the total uncertainty represented by the vertical error bars. The training set for the background class is shown by the blue dotted histogram. The test set for the background class is shown by the blue points, with the total uncertainty represented by the vertical error bars.

967 We can see that the shapes of the training and test sets for both signal and background are very similar. This is  
968 a good indicator that no over-training occurred. As with the object-level BDT, we perform another over-training  
969 check, by ensuring that the variance of the mean accuracy of each folds' test set in a 5 fold kfold cross validation  
970 is substantially small. This indicates that fluctuations in features from different training sets are not learnt by the  
971 classifier. For the event-level classifier, a variance of 0.00026 was calculated for the mean accuracies of each folds'  
972 test set in cross validation, providing further evidence that no over-training occurred.

973 In Figure ??, normalised distributions of the signal and total background of the event-level BDT discriminator  
974 output in the  $tWZ$  OF SR,  $tWZ$  SF SR and  $t\bar{t}Z$  CR, are shown.

975 The event-level BDT discriminates well between signal and background events in the  $tWZ$  OF SR,  $tWZ$  SF SR  
976 and  $t\bar{t}Z$  CR, with separations of 8.98%, 10.6% and 20.6%, respectively.

## 978 4.8 Two Neutrino Scanning Method ( $2\nu\text{SM}$ ) Algorithm

979 The Two Neutrino Scanning Method ( $2\nu\text{SM}$ ) algorithm<sup>1</sup> [59, 58] aims to reconstruct  $t\bar{t}$  systems in the  $2\ell$ ,  $3\ell$  and  
980  $4\ell$  final states (e.g.  $2\ell$  case:  $t\bar{t} \rightarrow \ell^+ \nu_\ell b\ell^- \bar{\nu}_\ell \bar{b}$ ). This was initially designed to suppress the  $t\bar{t}$  background in the  $t\bar{t}Z$

<sup>1</sup>software tool and weights provided by Thomas McCarthy ( $t\bar{t}Z$  analysis group - Max Planck Institute)

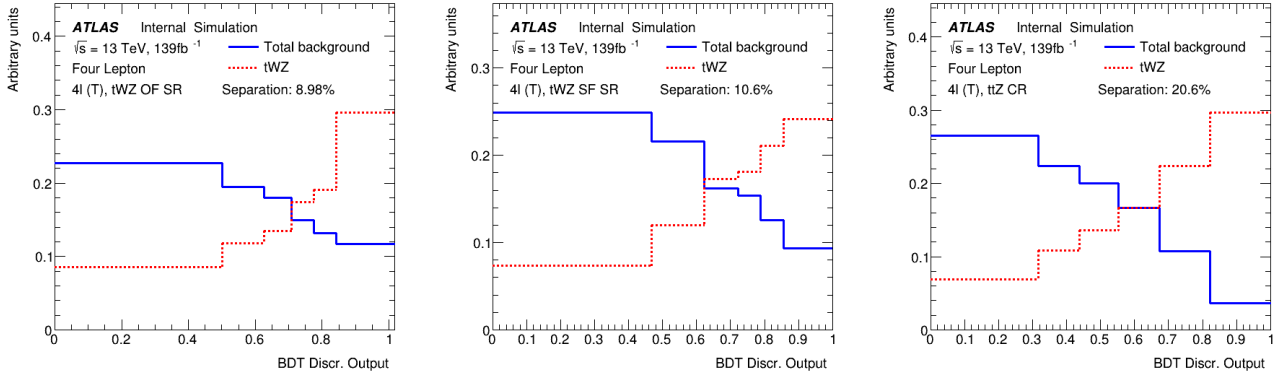


Figure 4.40: Normalised distributions of the signal and total background of the event-level BDT discriminator output in the  $tWZ$  OF SR,  $tWZ$  SF SR and  $t\bar{t}Z$  CR are shown (left to right). The dotted red and solid blue lines represent the distributions (normalised to an area of 1) of the signal and total background events respectively. The x-axis shows the event-level BDT discriminator output and the y-axis shows the relative number of events (in arbitrary units).

analysis. We can re-purpose this algorithm to distinguish between  $tWZ$  and  $t\bar{t}Z$  by removing the easily-identifiable  $Z$  boson.

The  $2\nu$ SM algorithm reconstructs a  $t\bar{t}$  system by scanning through the components of two possible neutrino 4-vectors ( $\nu_1$  and  $\nu_2$ ). It then aims to determine which  $\nu_1$  and  $\nu_2$  correspond to the two neutrinos which originate from the decay of a  $t\bar{t}$  system the best (quantified by an output weight,  $w_{2\nu,SM}$ ).  $w_{2\nu,SM}$  is the likelihood under the  $t\bar{t}$  dilipeton final state hypothesis. We are able to use this algorithm in our analysis to discriminate between  $tWZ$  and  $t\bar{t}Z$  since we can easily reconstruct the OSSF leptons which decay from the  $Z$  boson and remove it before inputting the event into the algorithm. We would then expect that the  $2\nu$ SM algorithm returns a higher score from a  $t\bar{t}Z$  event ( $\sim 1$ , i.e. it looks like a  $t\bar{t}$  event after removal of the  $Z$  boson) and a lower score from a  $tWZ$  event ( $\sim 0$ , i.e. it does not look like a  $t\bar{t}$  event after removal of the  $Z$  boson).

### 4.8.1 The algorithm

The  $2\nu$ SM algorithm starts off by writing down four equations which correspond to the invariant masses of the top quark ( $m(t)$ ) and  $W$  boson ( $m(W)$ ) for the two top decays (i.e.  $t \rightarrow W^+ b \rightarrow \ell^+ \nu_\ell$ ) in a dileptonic  $t\bar{t}$  event. These can be written as,

$$(\ell_1 + \nu_1)^2 = m(W)^2 = (80.385 \text{ GeV})^2 \quad (4.3)$$

$$(\ell_1 + \nu_1 + b_{1,2})^2 = m(t)^2 = (172.5 \text{ GeV})^2 \quad (4.4)$$

$$(\ell_2 + \nu_2)^2 = m(W)^2 = (80.385 \text{ GeV})^2 \quad (4.5)$$

$$(\ell_2 + \nu_2 + b_{2,1})^2 = m(t)^2 = (172.5 \text{ GeV})^2 \quad (4.6)$$

where the subscripts indicate that these particles originate from the decay of two different top quarks in a  $t\bar{t}$  system. We assume that the mass of the neutrinos ( $\nu_1$  and  $\nu_2$ ) are close to zero, which leaves us with 6 unknowns,  $p_{T,\nu_1}$ ,  $\phi_{\nu_1}$ ,  $\eta_{\nu_1}$ ,  $p_{T,\nu_2}$ ,  $\phi_{\nu_2}$  and  $\eta_{\nu_2}$  (components of the two neutrino's 4-vectors).

The  $2\nu$ SM algorithm takes the 4-vectors of the two reconstructed leptons (not from the  $Z$  boson) and the two jets with the highest DL1r  $b$ -tagger score as input. For each neutrino ( $\nu_1$  and  $\nu_2$ ), we scan over a range of possible  $\eta$  and  $\phi$  values. These values were chosen to be  $\phi_{\nu_1}, \phi_{\nu_2} \in [-\pi, \pi]$  with a step size of  $\approx 0.25$  and  $\eta_{\nu_1}, \eta_{\nu_2} \in [-5, 5]$  with a step size of  $\approx 0.31$ . These ranges were chosen to maximize accuracy and minimize computation time. For each of these possible  $\eta$  and  $\phi$  values, we calculate the corresponding  $p_T$  for each neutrino. The transverse momentum of a neutrino,  $p_{T,\nu}$ , can be calculated via (\*\*\*\*\*referecne somewhere here\*\*\*\*\*),

$$p_{T,\nu} = \frac{\frac{1}{2}(m(W)^2 - m(\ell)^2)}{E_\ell \cosh \eta_\nu - p_{\ell,z} \sinh \eta_\nu - p_{\ell,x} \cos \phi_\nu - p_{\ell,y} \sin \phi_\nu} \quad (4.7)$$

1006 where  $E_\ell$  is the energy of the lepton and  $p_{\ell,z}$ ,  $p_{\ell,x}$ ,  $p_{\ell,y}$  are the  $z$ ,  $x$  and  $y$  components of lepton's momentum. At  
 1007 this stage, we have possible 4-vectors for  $\nu_1$  and  $\nu_2$ . Using these possible neutrino 4-vectors, we reconstruct the two  
 1008 possible  $t\bar{t}$  systems,

$$t_1 = \ell_1 + b_1 + \nu_1 \text{ and } t_2 = \ell_2 + b_2 + \nu_2 \quad (4.8)$$

**OR**

$$t_1 = \ell_1 + b_2 + \nu_1 \text{ and } t_2 = \ell_2 + b_1 + \nu_2 \quad (4.9)$$

1009 These reconstructed  $t\bar{t}$  systems are then used to calculate a weight,  $w_{2\nu SM}$ . The  $w_{2\nu SM}$  weight (a value ranging  
 1010 from 0 to 1) is defined as a product of four probabilities (described below) and can be written as,

$$w_{2\nu SM} = P_{m_{t_1}} \times P_{m_{t_2}} \times P_{\Delta E_x} \times P_{\Delta E_y} \quad (4.10)$$

1011 The  $w_{2\nu SM}$  is calculated for each pair of reconstructed neutrinos (or reconstructed  $t\bar{t}$  systems), with the maximum  
 1012 value being chosen as the final value for the event.

### 1013 4.8.2 Calculating $w_{2\nu SM}$

1014 We use distributions of well modelled observables ( $m_{b\ell\nu}$  and  $\Delta E_x$ ) from simulated  $t\bar{t}$  events in order to determine  
 1015 how well our reconstructed neutrinos (and in turn top quarks) resemble neutrinos (and top quarks) present in a  $t\bar{t}$   
 1016 event.

#### 1017 4.8.2.1 $P_{m_{t_1}}$ and $P_{m_{t_2}}$

1018 A normalised distribution of the mass of reconstructed top quarks ( $m_{b\ell\nu}$ ) from a  $t\bar{t}$  sample is generated to  
 1019 determine the probabilities  $P_{m_{t_1}}$  and  $P_{m_{t_2}}$ . The distribution is generated from reco-level leptons, generator-level  
 1020 neutrinos and reoc-level jets matched in  $\Delta R$  to generator-level  $b$ -quarks, therefore only filling the distribution with  
 1021 correct detector-level objects. We then use the distribution to interpolate our two reconstructed top quarks, which  
 1022 returns a weight value from 0 to 1, with higher values corresponding to a reconstructed top quark which has a  
 1023 mass close to that of a top quark from a  $t\bar{t}$  system. This interpolation is done for both reconstructed tops,  $t_1$  and  
 1024  $t_2$ , corresponding to probabilities  $P_{m_{t_1}}$  and  $P_{m_{t_2}}$ . The distribution used is shown in Figure 4.41.

1025  
 1026 In Figure 4.41, the  $m_{b\ell\nu}$  distribution (generated from simulated  $t\bar{t}$  events), used to calculate  $P_{m_{t_1}}$  and  $P_{m_{t_2}}$  is  
 1027 shown.

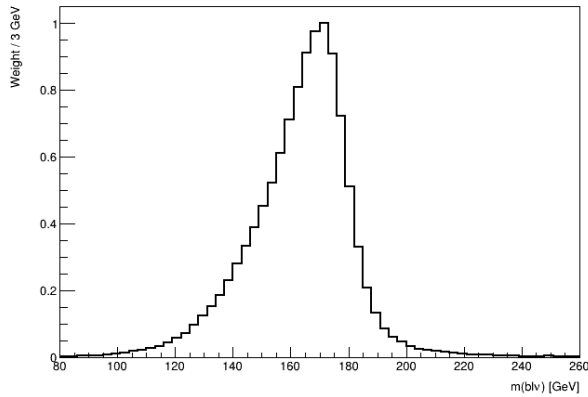


Figure 4.41:  $m_{b\ell\nu}$  distribution generated from simulated  $t\bar{t}$  events, used to calculate  $P_{m_{t_1}}$  and  $P_{m_{t_2}}$  is shown. The  
 $m_{b\ell\nu}$  distribution is shown by the black lined histogram. The mass of the  $b\ell\nu$  system is shown on the x-axis. The  
 corresponding weight of the  $m_{b\ell\nu}$  distribution is shown on the y-axis.

#### 1028 4.8.2.2 $P_{\Delta E_x}$ and $P_{\Delta E_y}$

1029 A similar method is used to determine  $P_{\Delta E_x}$  and  $P_{\Delta E_y}$ . In this case we generate a weight distribution of  $\Delta E_x =$   
 1030  $(p_{T,\nu_1})_x + (p_{T,\nu_2})_x - (E_T^{\text{miss}})_x$  based off simulated  $t\bar{t}$  events. In particular, this distribution is generated using reco-  
 1031 level  $E_T^{\text{miss}}$  and generator-level neutrinos. The use of this distribution lies under the assumption that neutrinos are

the dominant source of  $E_T^{\text{miss}}$ , and therefore,  $(E_T^{\text{miss}})_x \approx (p_{T,\nu_1})_x + (p_{T,\nu_2})_x$  and  $(E_T^{\text{miss}})_y \approx (p_{T,\nu_1})_y + (p_{T,\nu_2})_y$ . We then use the distribution to interpolate the value of  $\Delta E_x$  and  $\Delta E_y$  from our reconstructed neutrinos. This returns a weight value from 0 to 1, with higher values corresponding to  $\Delta E_x$  and  $\Delta E_y$  (and in turn our reconstructed neutrino's  $p_T$ ) closer to those observed in a  $t\bar{t}$  event. We expect the  $\Delta E_x$  and  $\Delta E_y$  distributions to have the same shapes, therefore we only need to generate one (we have chosen  $\Delta E_x$ ). In Figure 4.42, the  $m_{b\ell\nu}$  distribution (generated from simulated  $t\bar{t}$  events), used to calculate  $P_{m_{t_1}}$  and  $P_{m_{t_2}}$  is shown.

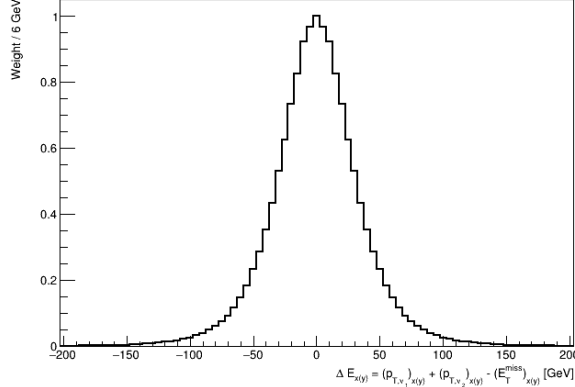


Figure 4.42:  $\Delta E_x$  distribution generated from simulated  $t\bar{t}$  events, used to calculate  $P_{\Delta E_x}$  and  $P_{\Delta E_y}$  is shown. The  $\Delta E_x$  distribution is shown by the black lined histogram.  $\Delta E_x$  is shown on the x-axis. The corresponding weight of  $\Delta E_x$  distribution is shown on the y-axis.

### 4.8.3 Kinematic Veto

The  $2\nu$ SM algorithm is extremely computationally intensive. The computation time depends on the number step size of the  $\phi$  and  $\eta$  ranges which we scan over to reconstruct the neutrinos. For example, consider the step sizes chosen in this analysis,  $\Delta\eta \approx 0.31$  and  $\Delta\phi \approx 0.25$  which corresponds to 32 values for  $\eta$  and 25 values for  $\phi$ . There will be  $(32)(32)(25) = 640\,000$  possible pairs of neutrinos ( $\nu_1$  and  $\nu_2$ ) to consider **per event**. Since we have to consider two possible  $t\bar{t}$  systems (See Equations 4.8 and 4.9), this number effectively increases to  $(2)(640\,000) = 128\,000$  iterations **per event**. In order to reduce the number of  $t\bar{t}$  systems we need to consider, therefore decreasing computation time, we look at distributions of well modelled observables from  $t\bar{t}$  events and veto (discard) a possible reconstructed  $t\bar{t}$  system if the observable in question is improbable or unlikely to be observed in a  $t\bar{t}$  event. To achieve this, we define a threshold range for these observables (See Figure 4.45 and Figure 4.47), and if the possible reconstructed  $t\bar{t}$  system's corresponding value for this observable lies outside this range, it is vetoed and the algorithm continues with the next iteration.

#### 4.8.3.1 $\Delta\langle m(\ell b) \rangle$

The first observable which we consider is the difference between average mass of the two possible  $\ell b$  system combinations,  $\Delta\langle m(\ell b) \rangle$ . The two possible  $\ell b$  system combinations are,

$$(\ell b)_1 = \ell_1 + b_1 \text{ and } (\ell b)_2 = \ell_2 + b_2 \quad (4.11)$$

**OR**

$$(\ell b)_1 = \ell_1 + b_2 \text{ and } (\ell b)_2 = \ell_2 + b_1 \quad (4.12)$$

$$(4.13)$$

$\Delta\langle m(\ell b) \rangle$  is therefore defined as,

$$\Delta\langle m(\ell b) \rangle = \frac{1}{2} |[(m(\ell_1 b_1) + m(\ell_1 b_1)) - (m(\ell_2 b_2) + m(\ell_2 b_1))]| \quad (4.14)$$

The idea here is that, if  $\Delta\langle m(\ell b) \rangle$  is large, it's more likely that we can simply select the  $\ell b$  combination with the smaller (minimum) average mass. To illustrate this, we look at the distribution (constructed from  $t\bar{t}$  events) of  $P(\text{Correct combination of } \ell b \text{ systems} | \text{minimum}\langle m(\ell b) \rangle)$  vs  $\Delta\langle m(\ell b) \rangle$  for  $b$ -tagged jets in the same ( $\eta(b_1) \times \eta(b_2) \geq 0$ )

1057 and opposite hemispheres ( $\eta(b_1) \times \eta(b_2) < 0$ ).

1058 In Figure 4.43 the  $P(\text{Correct combination of } \ell b \text{ systems} | \text{minimum}\langle m(\ell b) \rangle)$  vs  $\Delta\langle m(\ell b) \rangle$ , for  $b$ -tagged jets in the same and opposite hemispheres, constructed from  $t\bar{t}$  events is shown.

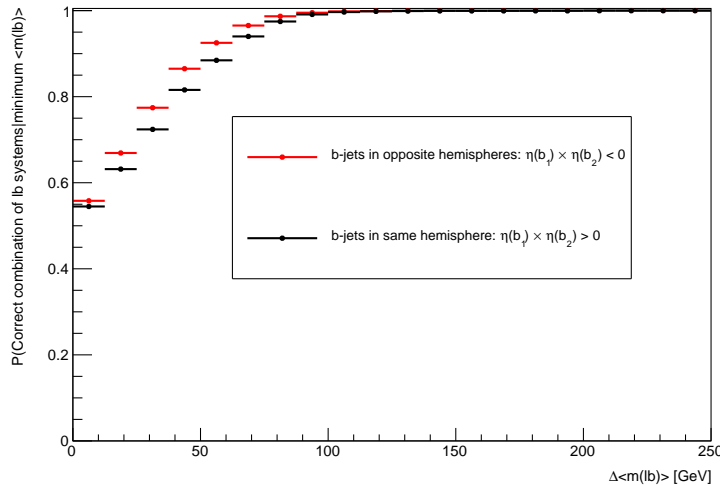


Figure 4.43:  $P(\text{Correct combination of } \ell b \text{ systems} | \text{minimum}\langle m(\ell b) \rangle)$  vs  $\Delta\langle m(\ell b) \rangle$ , for  $b$ -tagged jets in the same and opposite hemispheres, constructed from  $t\bar{t}$  events is shown. The horizontal red lines represent the distribution in the case when the two  $b$ -jets are in opposite hemispheres. The dot in the middle of the line represents the midpoint of the line. The horizontal black lines represent the distribution in the case when the two  $b$ -jets are in the same hemispheres. The dot in the middle of the line represents the midpoint of the line. The average  $m(\ell b)$  is shown on the x-axis. The  $P(\text{Correct combination of } \ell b \text{ systems} | \text{minimum}\langle m(\ell b) \rangle)$  is shown on the y-axis.

1059 From Figure 4.43, for both cases where the  $b$ -tagged jets are in the same and opposite hemispheres, the  
 1060 probability for a correct  $\ell b$  system being chosen given that we are considering the  $\ell b$  system with min-  
 1061 imum average mass is an increasing function which plateaus to 1 at  $\sim 90$  GeV. We use these two distribu-  
 1062 tions to interpolate the  $P(\text{Correct combination of } \ell b \text{ systems} | \text{minimum}\langle m(\ell b) \rangle)$  from  $\Delta\langle m(\ell b) \rangle$ . We require that  
 1063  $P(\text{Correct combination of } \ell b \text{ systems} | \text{minimum}\langle m(\ell b) \rangle) > 0.8$ , before vetoing any  $\ell b$  combination, such that we  
 1064 have are at least 80% certain that we know the correct  $\ell b$  combination. In this case, the  $\ell b$  combination with the  
 1065 maximum  $\Delta\langle m(\ell b) \rangle$  is vetoed. If  $P(\text{Correct combination of } \ell b \text{ systems} | \text{minimum}\langle m(\ell b) \rangle) < 0.8$  we need to consider  
 1066 both possible  $\ell b$  system combinations.  
 1067

#### 1068 4.8.3.2 $\eta(b\bar{b}\ell\ell)$

1069 We consider  $\eta$  of the  $b\bar{b}\ell\ell$  system,  $\eta(b\bar{b}\ell\ell)$  to veto improbable  $\eta(\nu_1)$  and  $\eta(\nu_2)$  values.

1070  
 1071 In the same way as for  $\Delta\langle m(\ell b) \rangle$ , we generate a distribution to determine values  $\eta(\nu)$  which are improbable for a  $t\bar{t}$   
 1072 event. In this case, we generate a 2D histogram from simulated  $t\bar{t}$  events (dileptonic final state) at generator-level  
 1073 of  $\eta(\nu)$  vs  $\eta(b\bar{b}\ell\ell)$ .

1074 In Figure 4.44, a heatmap of occupancy for  $\eta(\nu)$  vs  $\eta(b\bar{b}\ell\ell)$  (produced from simulated  $t\bar{t}$  events) is shown.  
 1075 Using the above heatmap, we define a veto region (where a  $t\bar{t}$  event is extremely unlikely to occur) based off  
 1076 double-sided 95% limits (\*\*something here on confidence limit??\*\*). We apply a veto if either possible neutrino  
 1077 lies within this region. The veto region is shown in Figure 4.45.

1078 In Figure 4.45, the veto region (extracted from Figure 4.44) for vetoing improbable neutrinos is shown.

#### 1081 4.8.3.3 $L_T$

1082 The final kinematic constraint which we consider is the scalar sum of lepton  $p_T$ ,  $L_T = p_T(\ell_1) + p_T(\ell_2)$  which we  
 1083 use to veto certain possible neutrinos,  $\nu_1$  and  $\nu_2$ .

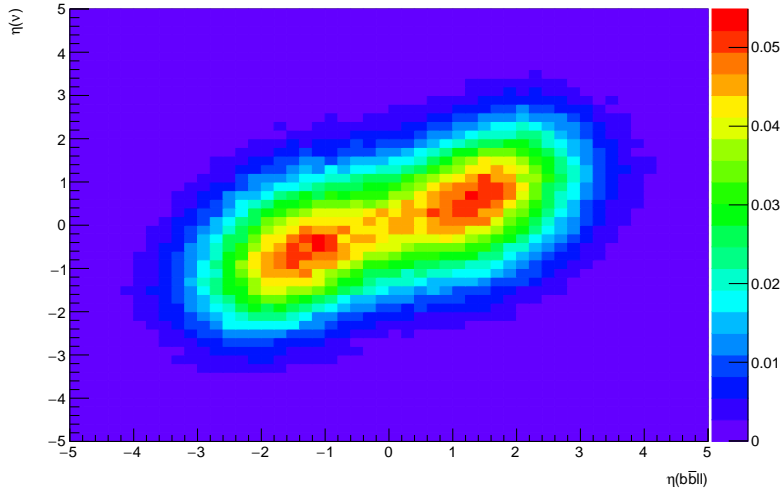


Figure 4.44: Heatmap of occupancy for  $\eta(\nu)$  vs  $\eta(b\bar{b}\ell\ell)$  produced from simulated  $t\bar{t}$  events (dileptonic final state) at generator-level is shown.  $\eta$  of the  $b\bar{b}\ell\ell$  system is shown on the x-axis.  $\eta$  of the neutrino is shown on the y-axis. The colorbar on the right represents the occupancy (normalised) in the phase space.

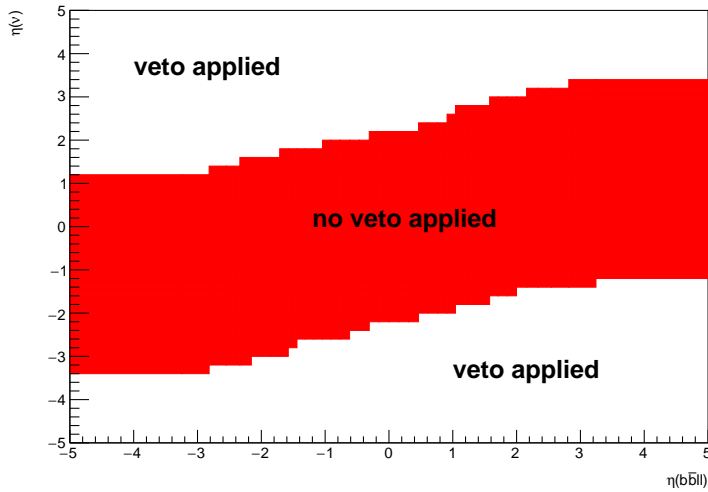


Figure 4.45: The regions where vetoes are applied for the  $\eta(b_1 b_2 \ell_1 \ell_2)$  constraint is shown.  $\eta$  of the  $b\bar{b}\ell\ell$  system is shown on the x-axis.  $\eta$  of the neutrino is shown on the y-axis. The red band shows the region where the neutrino would not be vetoed. The white areas (above and below the red band) are regions where the neutrino is vetoed.

Again, we generate a distribution to determine (and veto) improbable possible neutrinos in simulated  $t\bar{t}$  events (dilepton final state).

In Figure 4.46, a heatmap of occupancy for  $\Delta R(\ell, \nu)$  vs  $L_T$  (produced from simulated  $t\bar{t}$  events) is shown.

Using the same method as described in Section 4.8.3.2, we define a veto region where a veto is applied if either possible neutrino lies within this region. In Figure 4.45, the veto region (extracted from Figure 4.46) for vetoing improbable neutrinos values is shown.

## 4.9 Systematics

The systematic uncertainties can be separated into experimental (detector) systematics, which are related to the reconstruction of physics objects in the detector and theoretical uncertainties related to the modelling of the different processes background.

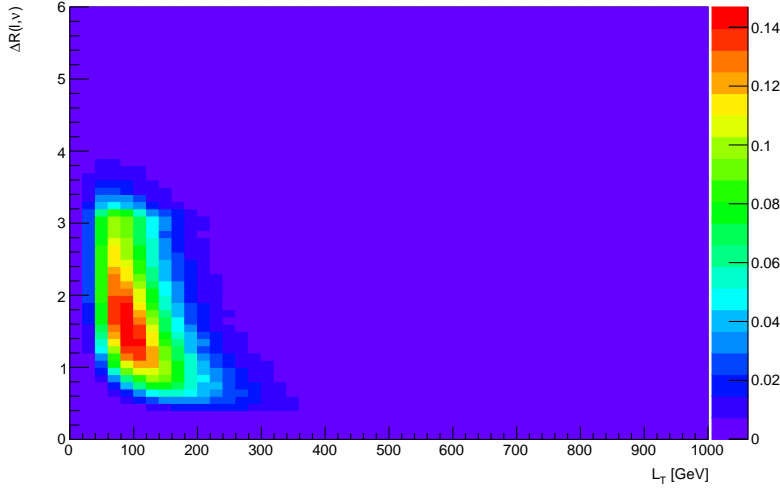


Figure 4.46: A heatmap of occupancy for  $\Delta R(\ell, \nu)$  vs  $L_T$  produced from simulated  $t\bar{t}$  events (dileptonic final state) at generator-level is shown.  $\Delta R$  between leptons and neutrinos is shown on the x-axis.  $L_T$  (scalar sum of lepton  $p_T$ ) is shown on the y-axis. The colorbar on the right represents the occupancy (normalised) in the phase space.

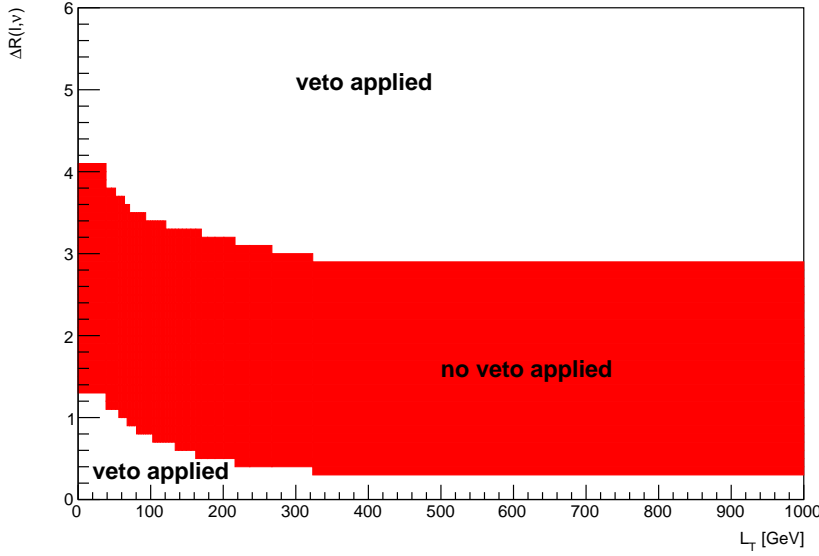


Figure 4.47: The regions where vetoes are applied for the  $L_T$  constraint is shown.  $\Delta R$  between leptons and neutrinos is shown on the x-axis.  $L_T$  (scalar sum of lepton  $p_T$ ) is shown on the y-axis. The red band shows the region where the neutrino would not be vetoed. The white areas (above and below the red band) are regions where the neutrino is vetoed.

#### 1095 4.9.1 Experimental uncertainties

1096 In this section, the experimental systematics are outlined.

- 1097 • **Luminosity:**

1098 The 2015–2018 luminosity estimate of  $139\text{fb}^{-1}$  has a relative uncertainty of 3%. This uncertainty is obtained  
1099 using the LUCID-2 detector [22] for the primary luminosity measurements. This systematic uncertainty affects  
1100 all processes modelled using MC simulations.

- 1101 • **Pile-up reweighting:**

An uncertainty related to the SFs used for MC to account for differences in pile-up distributions between MC and data is applied. This uncertainty is obtained by re-scaling the  $\langle \mu \rangle$  value in data by 1.00 and 1/1.18 corrections are only applied to MC.

- **Jet vertex tagger:**

Uncertainties associated to the *JVT* are applied via the `JetJvtEfficiency` package [20] which account for the residual contamination from pile-up jets after pile-up suppression and the MC generator choice [13].

- **Heavy- and light-flavor tagging:**

The efficiency of the flavour-tagging algorithm is measured for each jet flavour using control samples in data and in simulation. From these measurements, correction factors are derived to correct the tagging rates in the simulation. In the case of  $b$ -tagged jets, the correction factors and their uncertainties are estimated from data using dileptonic  $t\bar{t}$  events [15, 10]. In the case of  $c$ -jets, they are derived from jets arising from  $W$  boson decays in  $t\bar{t}$  events [14]. In the case of light-flavour jets, the correction factors are derived using dijet events [11]. Sources of uncertainty affecting the  $b$ - and  $c$ -tagging efficiencies are evaluated as a function of jet  $p_T$ , including bin-to-bin correlations. The uncertainties in the efficiency for tagging light-flavour jets depend on the jet  $p_T$  and on  $\eta$ . An additional uncertainty is assigned to account for the extrapolation of the  $b$ -tagging efficiency measurement from the  $p_T$  region used to determine the correction factors to regions with higher  $p_T$ .

- **Electron efficiency:**

Uncertainties associated with the electron efficiency SFs are provided by the egamma CP group [18] and arise from the reconstruction, ID, isolation and trigger efficiencies. They correct for the efficiency difference between data and MC [12] and are measured with a “tag-and-probe” method in  $Z \rightarrow e^+e^-$  and  $J/\psi \rightarrow e^+e^-$  events. The information on the correlation of the different components of the systematic uncertainties are provided for all efficiency measurements. The default correlation model for the uncertainties is used, which provides one up/down variation for each of the SF components separately [18, 19].

- **Muon efficiency:**

As for electrons, SFs obtained from  $Z \rightarrow \mu^+\mu^-$  and  $J/\psi \rightarrow \mu^+\mu^-$  events are applied to correct for the differences between data and MC in the muon ID, isolation and trigger efficiencies [16]. Uncertainties on these SFs are provided by the muon CP group [21] and applied as up/down variations of the nominal SFs for each component.

### 4.9.2 Theoretical uncertainties

In this section, the theoretical systematics are outlined.

- **$t\bar{t}Z$  background:**

An overall normalization uncertainty of 10% is considered for the  $t\bar{t}Z$  background. Two generic shape systematics are considered for the  $t\bar{t}Z$  background. They are constructed (see Section 4.9.3) by either applying a linear or triangular interpolation to up and down variations which are defined to be  $\pm 20\%$  from the nominal  $t\bar{t}Z$  background.

- **$ZZ$  background:**

An overall normalization uncertainty of 30% is considered for the  $ZZ$  background.

- **$t\bar{t}H$  background:**

An overall normalization uncertainty of 20% is considered for the  $t\bar{t}H$  background.

- **$tZq$  background:**

An overall normalization uncertainty of 14% is considered for the  $tZq$  background.

- **$t\bar{t}Z$  fake background:**

An overall normalization uncertainty of 50% is considered for the  $t\bar{t}Z$  fake background.

1145 • **other background processes:**

1146 The 'other' background consists of many processes which have minimal but non-negligible contribution in  
 1147 the signal regions (See Table 4.4). An overall normalization uncertainty of 30% is considered for the 'other'  
 1148 background processes.

1149 •  **$tWZ$ :** A modelling uncertainty on  $tWZ$  is considered by comparing the nominal sample (using the DR1  
 1150 scheme) and a minimal DR2 sample.

1151 Two generic shape systematics are considered for the  $tWZ$  background. They are constructed (see Sec-  
 1152 tion 4.9.3) by either applying a linear or triangular interpolation to up and down variations which are defined  
 1153 to be  $\pm 20\%$  from the nominal  $tWZ$  background.

1154 **4.9.3 Generic shape systematics**

1155 It is evident that the tetralepton channel is statistically limited. We therefore expect that the uncertainty on  $u_{tWZ}$   
 1156 is dominated by statistical uncertainty and that the impact of shape systematics will be negligible in comparison.

1157 In order to include shape uncertainties related to the modelling of our samples, we construct generic shape  
 1158 systematics for any given sample process. Given that we choose a sufficiently large set of values for which the  
 1159 systematics can take in the fit, the constructed systematics could represent many shape systematics which we have  
 1160 not yet considered to include in the fitting procedure.

1162 We start by constructing an envelope (error bars) consisting of two MC templates. One with the nominal MC  
 1163 template increased by 20% on its normalisation and the other with the nominal MC template decreased by 20% on  
 1164 its normalisation. The templates are then modified from their original shape either by doing linear interpolation  
 1165 (from the leftmost-up variation to the rightmost-down variation) or triangular interpolation (shape is set to zero at  
 1166 the rightmost and leftmost parts and reaches the envelope in the middle). The linear and triangular interpolation is  
 1167 done using TRF's ForceShape option [67], which alters the original templates (as described above). This envelope  
 1168 now represents the bounds which the systematic can vary in the fit.

1169 In Figure 4.48 the envelope before and after the shape change, for both the linear and triangular interpolations, for  
 1170 the  $t\bar{t}Z$  background in the  $t\bar{t}Z$  CR is shown.

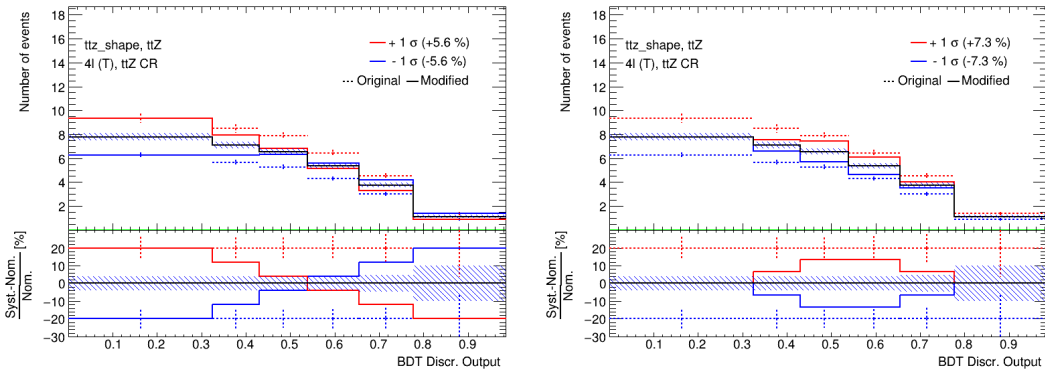


Figure 4.48:  $t\bar{t}Z$  generic shape systematic before (original) and after (modified) linear (left) and triangular (right) interpolation in the  $t\bar{t}Z$  CR is shown. The output from the event-level BDT shown on the x-axis. In the upper panel, the number of events is shown on the y-axis. In the lower panel, the difference between the systematic variation (the envelope's templates) and the nominal template, divided by the nominal template, is shown on the y-axis. The nominal  $t\bar{t}Z$  template is shown by the solid black lined histogram, with the diagonal lined bands representing its total uncertainty. The templates of the upper and lower envelopes (before modification) is given by the dotted red and blue lined histograms respectively. The templates of the upper and lower envelopes (after modification) is given by the solid red and blue lined histograms respectively, with the vertical dotted lines representing its total uncertainty.

1173 We consider two shape systematics (linear and triangular shapes) for  $tWZ$  and the most dominant background  
 1174 processes across both channels. In particular, we consider these shape systematics for  $t\bar{t}Z$  for both the tri- and

1175 tetralepton channels. Additionally, we consider these shape systematics for the  $WZ + b$  and  $WZ + c$  backgrounds  
 1176 in the trilepton channel.

## 1177 4.10 Analysis Pipeline and **TRExFitter**

1178 We make use of industry standard **ROOT**<sup>2</sup> wrappers in this analysis, namely, **PyROOT** and **TRExFitter**.

1179  
 1180 **Python** is used extensively in many fields of science (not limited to physics and data science) due to its simplicity  
 1181 and ongoing support by the communities which utilize it. **PyROOT** allows users to access the full **ROOT** functionality  
 1182 within **Python**. More specifically, **PyROOT** provides **Python** bindings for **ROOT**.

1183  
 1184 **TRExFitter** is a framework for binned template profile likelihood fits[78]. In this analysis, we used **TRExFitter**  
 1185 (tag: **TRExFitter-00-04-13**) to produce all pre-fit and post-fit plots (including fit statistics, e.g. limit, significance,  
 1186  $\mu_{best-fit}$ ).

1187  
 1188 The analysis pipeline starts with sample derivations (derived dataset) being submitted to the grid for ntuple  
 1189 production. This applies cuts and selections to the already reduced derivations and produces ntuples with trees  
 1190 containing variables (e.g. scale factors, observables, MC truth flags) that will be used at future stages in the analysis.  
 1191 These ntuples are then read by **PyROOT** where the events are looped over, before being written to **ROOT** files as input  
 1192 to **TRExFitter**. The **Python** scripts are used to define the different regions and apply the final cuts and selections  
 1193 outlined in Table 4.3. In addition to this purpose, they are used to train the two BDTs and to produce the output  
 1194 from these trained BDTs. As each event is looped over, the cuts and selection criteria are checked for the given  
 1195 event and is either thrown away (if the event does not pass the selection criteria), or gets written to a **ROOT** file (if  
 1196 the event passes the selection criteria) corresponding to the MC sample and Run 2 data-set (mc16a, mc16d, mc16e)  
 1197 which it belongs to. These **ROOT** files contain all observables, weights and scale factors (corresponding to an event)  
 1198 which we wish to use in **TRExFitter**. **TRExFitter** then takes these files as input, runs a maximum likelihood fit  
 1199 and produces relevant plots (e.g. pre-fit, post-fit, pull plots) and statistical parameters (e.g. limit, significance,  
 1200  $\mu_{best-fit}$ ).

### 1201 4.10.1 Fitting Procedure

1202 Using the **TRExFitter** framework, binned profile-likelihood fits are performed to determine the signal strength,  
 1203  $\mu_{tWZ} = \frac{\sigma_{obs}(tWZ)}{\sigma_{SM}(tWZ)}$ , of  $tWZ$  production. A fit across all regions in the tetralepton channel is performed to determine  
 1204 the sensitivity  $tWZ$  in this channel. In Section 4.11.2, a combined fit is performed across all regions in the trilepton  
 1205 and tetralepton channels to take advantage of the sensitivity of  $tWZ$  in both channels in order to further boost  
 1206 the sensitivity of  $tWZ$ .

1207  
 1208 To characterise the sensitivity and associated uncertainty of our measurement of  $\mu(tWZ)$ , we compute two metrics:  
 1209 the expected significance ( $Z_\mu^{exp}$ ) and the expected upper limit ( $\mu_{up}^{exp}$ ). In this context, the expected significance  
 1210 can be interpreted as, the probability that the measured signal is due to a background fluctuation. Larger values  
 1211 indicate lower probabilities and smaller values indicate higher probabilities. Particle physicists have adopted a  
 1212 standard to define the sensitivity necessary for evidence and discovery of a particular particle or phenomena. A  
 1213  $3\sigma$  (corresponding to a background fluctuation probability of  $\approx 10^{-3}$ ) significance is considered to be evidence  
 1214 for observation and a  $5\sigma$  (corresponding to a background fluctuation probability of  $\approx 10^{-7}$ ) is considered to be  
 1215 a discovery. The expected upper limit is a single-sided interval test statistic, associated with the POI in the  
 1216 maximum-likelihood fit ( $\mu(tWZ)$ , in our case). In this context, the expected upper limit can be understood in the  
 1217 following way: consider running an ensemble of MC toy experiments, each with their own confidence interval (a  
 1218 range of possible values for  $\mu(tWZ)$ ). An expected upper limit, at some fixed percentage  $x\%$  (or *confidence level*),  
 1219 can be determined from this ensemble. The expected upper limit tells us that,  $x\%$  of the toy MC experiment's  
 1220 confidence intervals will contain the true value of  $\mu(tWZ)$ . A commonly used percentage in particle physics is  
 1221 95%, which we adopt for this analysis. In particle physics, this is referred to as the *CLs Method* [38]. The CLs  
 1222 test statistic can be calculated 'brute force' by running these MC toy experiments, however this is very CPU  
 1223 intensive. Asymptotic formulae are able to describe the underlining CLs test statistic distributions under certain  
 1224 approximations [8]. Instead of running toy MC experiments, we use asymptotic formulae to perform the CLs

<sup>2</sup>CERN's HEP data analysis framework (written in C++)

method, which reduces computation time from several millions of CPU hours to several CPU minutes. The significance and upper limits which are calculated in this analysis are given a prefix of 'expected' to indicate that these are results from a blinded analysis.

In the separate and combined fits, the *mixed data and MC* fit setup [79] is used. This is done to obtain the most accurate prediction of the expected results while keeping the signal regions blinded. For this setup, first a background-only fit to the control regions using real data is done to determine estimates of the nuisance parameters. Then these estimates are used to construct a modified ASIMOV dataset in the signal regions. Finally, the fit is performed using real data in the control regions and the aforementioned modified ASIMOV data-set in the signal regions.

In these fits, the parameter of interest (POI) is  $\mu_{tWZ}$ . The POI is ultimately the quantity which we wish to measure and is set as a free parameter (unconstrained; can take any value in the fit). The nuisance parameters are assigned to the systematic uncertainties outlined in Section 4.9. Furthermore, a gamma ( $\gamma$ ) nuisance parameter for a bin is added to the likelihood function if the statistical uncertainty in the bin exceeds 0.1% of its nominal value.

Pruning is done per sample and per region on the shape and normalisation uncertainties for samples. A sample's shape and normalisation nuisance parameter is pruned (removed from the limit/fit) if the fraction of signal yield to the total yield (signal + background) is less than 0.01.

An auto-binning algorithm, `TransfoD` [28], was used to define the binning. This aims to maximise  $\frac{\text{signal}}{\text{background}}$  in each bin. Furthermore, it aims to avoid defining bins with a low number of events.

## 4.11 Results

In the section, an expected upper limit and an expected significance are set on the cross section of  $tWZ$ . This is performed for the current analysis in the tetralepton channel as well as for a combined analysis across the trilepton and tetralepton channels. The trilepton analysis was performed as an independent study by Benjamin Warren (UCT) [80]. Note that throughout this section, all signal regions remain blinded.

### 4.11.1 Tetralepton Channel

In Figure 4.49 pre-fit distributions for the variables used in the likelihood fit in each region are shown.

In Figure 4.50 pre-fit distributions for the variables used in the likelihood fit in each region are shown.

In Table 4.10, the post-fit yields for each sample in each region is shown.

	$tWZ$ OF SR	$tWZ$ SF SR	$ttZ$ CR	$ZZb$ CR	$(tWZ)_{\text{fake}}$ CR
$t\bar{t}Z$	$13.2379 \pm 1.52295$	$9.62061 \pm 1.12291$	$29.9054 \pm 3.60908$	$5.08899 \pm 0.620121$	$18.5393 \pm 2.23036$
$t\bar{t}Z$ fakes	$0.0702522 \pm 0.0468691$	$0.0334067 \pm 0.0256903$	$0.0723509 \pm 0.0418526$	$0.0485273 \pm 0.029133$	$5.04378 \pm 2.34732$
$tWZ$	$7.83414 \pm 3.31679$	$5.33547 \pm 2.24801$	$5.69373 \pm 2.58041$	$2.89889 \pm 1.23837$	$10.278 \pm 4.3345$
$ZZ$	$0.481776 \pm 0.119774$	$7.72372 \pm 1.2351$	$1.07955 \pm 0.182461$	$40.6067 \pm 6.26078$	$6.86097 \pm 1.11443$
$t\bar{t}$	$6.00553e-06 \pm 3.02819e-06$	$0.252557 \pm 0.442116$	$0.273507 \pm 0.223201$	$6.00553e-06 \pm 3.02819e-06$	$2.35427 \pm 0.917112$
$tZq$	$0.0827905 \pm 0.0398773$	$0.0756107 \pm 0.0354584$	$0.063585 \pm 0.0293325$	$0.05884 \pm 0.0244084$	$4.90963 \pm 0.745354$
$t\bar{t}W$	$0.00668643 \pm 0.00792217$	$0.00279748 \pm 0.00287361$	$6.00553e-06 \pm 3.02819e-06$	$0.002306 \pm 0.00564349$	$0.943182 \pm 0.292148$
$WZ$	$0.0442934 \pm 0.024156$	$0.0396511 \pm 0.0154282$	$0.0133471 \pm 0.0128199$	$0.0472562 \pm 0.0330315$	$1.83567 \pm 0.392459$
other					
$t\bar{t}$	$0.000987164 \pm 0.000766266$	$0.00247481 \pm 0.00136945$	$0.0140869 \pm 0.00479496$	$6.00553e-06 \pm 3.02819e-06$	$0.0100558 \pm 0.00363157$
$t\bar{t}\bar{t}$	$0.00934035 \pm 0.0080554$	$0.0107458 \pm 0.00849984$	$0.0571373 \pm 0.0204011$	$6.00553e-06 \pm 3.02819e-06$	$0.0216809 \pm 0.00992819$
$t\bar{t}WW$	$0.0294618 \pm 0.0263174$	$0.029771 \pm 0.0195582$	$0.264364 \pm 0.0926252$	$0.0129431 \pm 0.0323803$	$0.152448 \pm 0.058965$
$VVV(V = W/Z)$	$0.280643 \pm 0.0853411$	$0.191433 \pm 0.0586778$	$0.0697266 \pm 0.0225059$	$0.171142 \pm 0.0518102$	$0.266502 \pm 0.0810194$
$t\bar{t}H$	$0.846054 \pm 0.175495$	$0.669375 \pm 0.140107$	$1.96662 \pm 0.401199$	$0.150025 \pm 0.0353826$	$2.21264 \pm 0.451623$
Total	$22.9243 \pm 2.96284$	$23.9876 \pm 2.11249$	$39.4734 \pm 3.44937$	$49.0856 \pm 6.04162$	$53.4282 \pm 4.31683$
data	-	-	36	49	57

Table 4.10: The post-fit yields for each sample in each region is shown.

The expected upper limit of  $tWZ$  in the tetralepton channel is measured as,

$$\mu_{up}^{exp} = 1.61^{+2.35}_{-1.16} \quad (4.15)$$

The expected significance of  $tWZ$  in the tetralepton channel is measured as,

$$Z_\mu^{exp} = 1.44\sigma \quad (4.16)$$

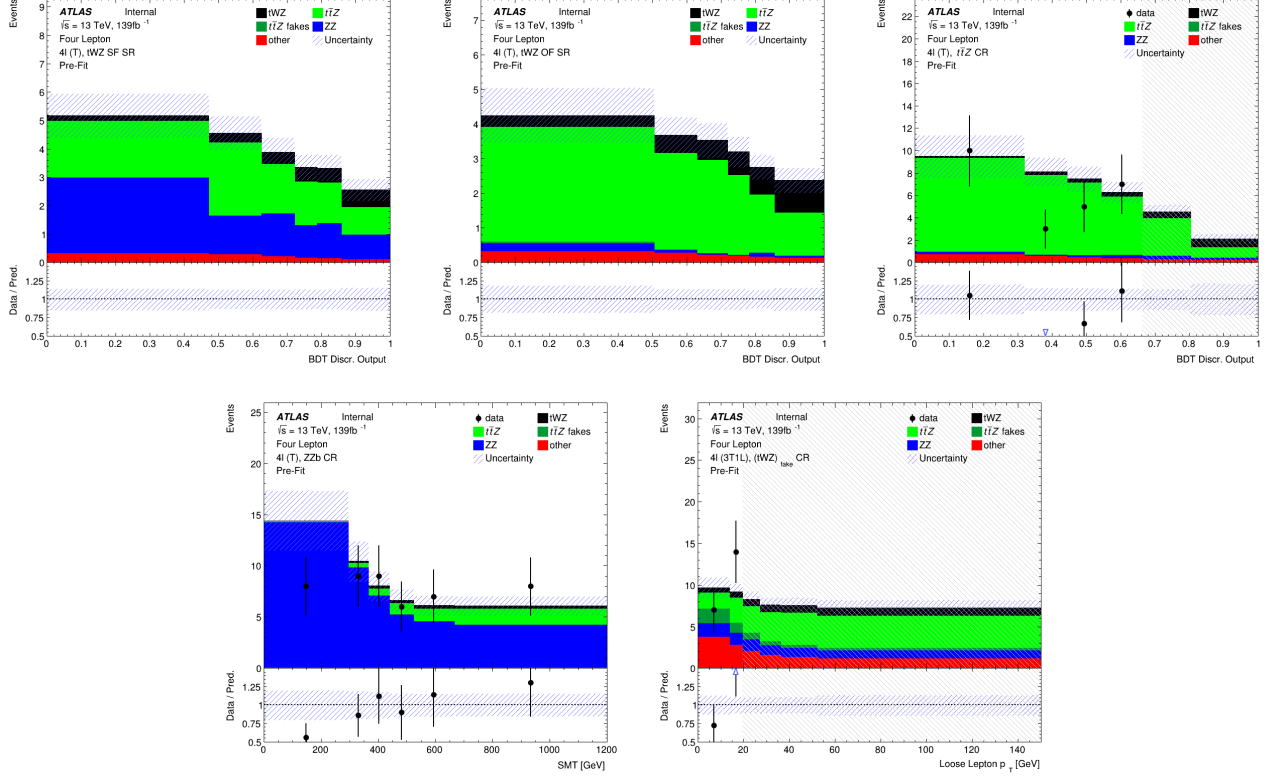


Figure 4.49: Pre-fit distributions (blinded) of variables used in the fit are shown. The data is given by the black points and the MC predictions for each process are given by the histograms. The vertical lines on the data points represent the total uncertainty in the data and the diagonal lined bands represent the total MC uncertainty. The lower panel in each plot shows the ratios of the data to the theoretical predictions. The plots in the  $tWZ$  OF SR and  $tWZ$  SF SR are kept blinded by omitting the data points. **Top left:** The event-level BDT Disc. Output in the  $tWZ$  SF (4T) SR region is shown. **Middle Top:** The event-level BDT Disc. Output in the  $tWZ$  SF (4T) SR region is shown. **Top right:** The event-level BDT Disc. Output in the  $t\bar{t}Z$  CR region is shown. **Bottom left:**  $SMT = \sum p_T(\ell) + \sum p_T(jet) + E_T^{\text{miss}}$  in the  $ZZb$  CR is shown. **Bottom right:**  $p_T(\text{loose lepton})$  in the  $(tWZ)_{\text{fake}}$  (3T1L) CR is shown.

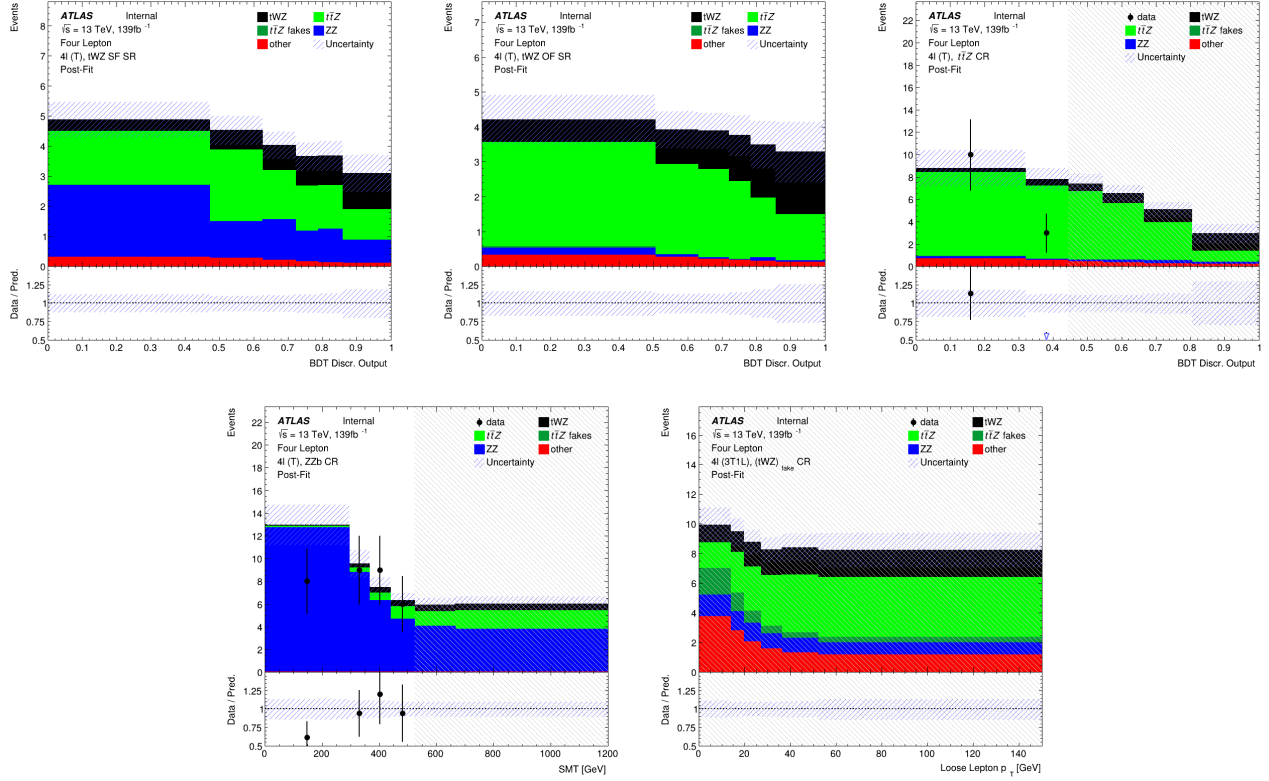


Figure 4.50: Post-fit distributions (blinded) of variables used in the fit are shown. The data is given by the black points and the MC predictions for each process are given by the histograms. The vertical lines on the data points represent the total uncertainty in the data and the diagonal lined bands represent the total MC uncertainty. The lower panel in each plot shows the ratios of the data to the theoretical predictions. The plots in the  $tWZ$  OF SR and  $tWZ$  SF SR are kept blinded by omitting the data points. **Top left:** The event-level BDT Disc. Output in the  $tWZ$  SF (4T) SR region is shown. **Middle Top:** The event-level BDT Disc. Output in the  $tWZ$  SF (4T) SR region is shown. **Top right:** The event-level BDT Disc. Output in the  $t\bar{t}Z$  CR region is shown. **Bottom left:**  $SMT = \sum p_T(\ell) + \sum p_T(jet) + E_T^{\text{miss}}$  in the  $ZZb$  CR is shown. **Bottom right:**  $p_T$ (loose lepton) in the  $(tWZ)_{\text{fake}}$  (3T1L) CR is shown.

1258 The best-fit value of the signal strength,  $\mu(tWZ) = \frac{\sigma(tWZ)}{\sigma(tWZ)_{SM}}$ , from the likelihood fit is measured as,

$$\mu(tWZ) = 1.91^{+0.95}_{-0.82} \quad (4.17)$$

1259 The expected upper limit is in agreement with the extracted best-fit value on the signal strength, therefore no  
 1260 deviations from the SM cross section of  $tWZ$  is observed. Neither the  $3\sigma$  evidence nor the  $5\sigma$  discovery standards  
 1261 are reached for the expected significance. This is not surprising, given the low amount of events present in the  
 1262 tetralepton channel.

1263  
 1264 In Figure 4.51, a ranking plot showing the impact of the systematic uncertainties on the POI,  $\mu(tWZ)$  is shown.

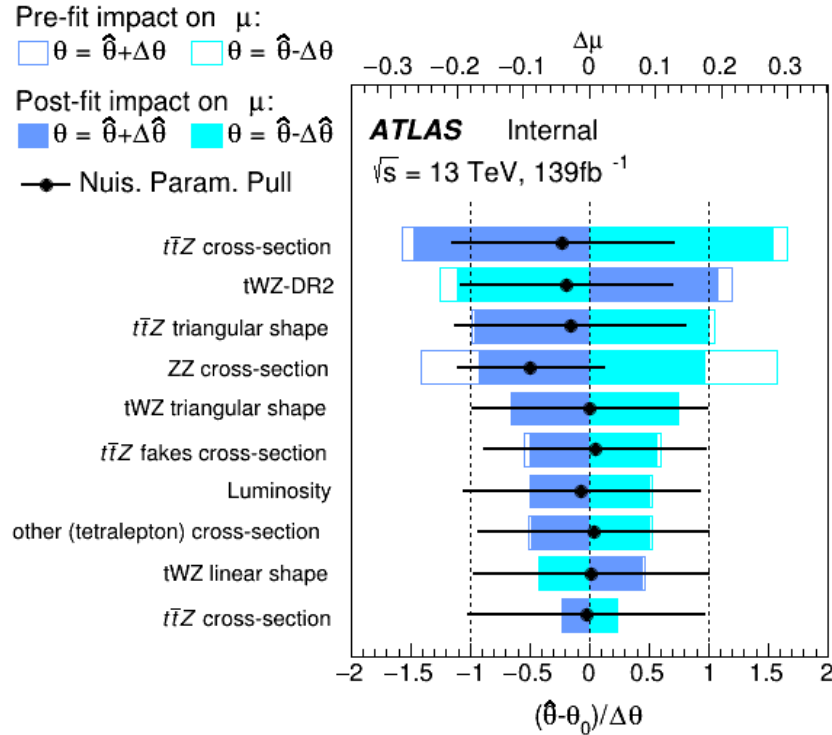


Figure 4.51: A ranking plot showing the impact (ordered from top to bottom via decreasing impact) of the systematic uncertainties (top 10) on the POI,  $\mu(tWZ)$ , in the tetralepton channel is shown.  $\hat{\theta}$  is the best-fit value of the nuisance parameter.  $\Delta\hat{\theta}$  and  $\Delta\theta$  are the post-fit and pre-fit uncertainties respectively. The post-fit and pre-fit impact of each nuisance parameter on  $\mu(tWZ)$  are shown with the solid and lined rectangles respectively. The empty and solid blue rectangles correspond to the pre-fit and post-fit impacts on  $\mu(tWZ)$  respectively. These impacts are shown on the upper axis ( $\Delta\mu$ ). On the lower axis, the nuisance parameter pull,  $\frac{\hat{\theta} - \theta_0}{\Delta\theta}$ , is shown ( $\theta_0$  is the nominal pre-fit value of the nuisance parameter). The nuisance parameter pull is indicated by the black points, with their relative post-fit errors ( $\frac{\Delta\hat{\theta}}{\Delta\theta}$ ) shown by the black horizontal error bars.

1265 The most important systematics are the cross sections of  $t\bar{t}Z$  and  $ZZ$ , and shape modelling on  $t\bar{t}Z$  ( $t\bar{t}Z$  triangular  
 1266 shape) and  $tWZ$  ( $tWZ$ -DR2 and  $tWZ$  triangular shape). The cross section of  $ZZ$  is significantly shifted down  
 1267 in the fit from its nominal value. The  $t\bar{t}Z$  cross section,  $tWZ$ -DR2 and  $t\bar{t}Z$  triangular shape nuisance parameters  
 1268 are similarly shifted down in the fit from their nominal values, but to a much lesser degree than the cross section  
 1269 of  $ZZ$ . These pulls are all within  $1\sigma$  uncertainty and are thus relatively small. It is expected that the modelling  
 1270 uncertainties (shape and normalisations) of the most dominant backgrounds (e.g.  $t\bar{t}Z$ ,  $ZZ$ ) have relatively large  
 1271 impacts on  $\mu(tWZ)$ , since the uncertainty of the analysis is dominated by statistical uncertainty.

#### 1272 4.11.2 Trilepton and Tetralepton Channels

1273 In the section, an expected upper limit and an expected significance are set on the cross section of  $tWZ$  from the  
 1274 combined fit across all regions of  $tWZ$  in the tetralepton and trilepton channels.

1275

Nuisance Parameter	Channel Affected	
	trilepton	tetralepton
$\sigma(t\bar{t}H)$	✓	✓
$\sigma(t\bar{t}Z)$	✓	✓
$\sigma(WZ)$	✓	✓
$\sigma(tZq)$	✓	✓
$\sigma(ZZ)$	✓	✓
$\sigma(\text{other(trilepton)})$	✓	✗
$\sigma(\text{other(tetralepton)})$	✗	✓
$\sigma(t\bar{t}Z)_{\text{fakes}}$	✗	✓
$\sigma(t\bar{t})_{\text{fakes}}$	✓	✗
$\sigma(Z + \text{jets})_{\text{fakes}}$	✓	✗
Luminosity	✓	✓
$jvt$	✓	✓
pileup	✓	✓
DL1r SF (b jets)	✓	✓
DL1r SF (light jets)	✓	✓
$\sigma(tWZ - DR2)$	✗	✓
lepton SF	✓	✓
$t\bar{t}Z$ triangular shape	✓	✓
$t\bar{t}Z$ linear shape	✓	✓
$WZ + b$ triangular shape	✓	✗
$WZ + b$ linear shape	✓	✗
$WZ + c$ triangular shape	✓	✗
$WZ + c$ linear shape	✓	✗

Table 4.11: A summary of the nuisance parameters used in the combined fit is shown. The channels which are affected by each nuisance parameter are indicated with a ✓ (is affected) or a ✗ (is not affected).

The trilepton analysis follows a similar analysis strategy to that of the tetralepton analysis. It includes an event-level BDT which aims to discriminate between the  $tWZ$  and all background as well as an object-level BDT which aims to identify hadronically decaying  $W$  bosons to discriminate between  $tWZ$  and the large  $WZ$  background. One  $tWZ$  SR is defined and five CRs are defined.  $WZ$  and  $t\bar{t}Z$  CRs are defined to constrain the dominant  $WZ$  and  $t\bar{t}Z$  backgrounds. Three CRs which require that one of the three selected leptons are loose, are defined for  $WZ$ ,  $t\bar{t}Z$  and  $tWZ$  in order to constraint the fake lepton component (using the MC template method - similar to the method used in Section 4.6 to estimate the fake lepton component).

The expected upper limit of  $tWZ$  in the trilepton channel is measured as,

$$\mu_{up}^{exp} = 2.65^{+3.67}_{-1.91} \quad (4.18)$$

The expected significance of  $tWZ$  in the trilepton channel is measured as,

$$Z_\mu^{exp} = 0.75\sigma \quad (4.19)$$

The best-fit value of the signal strength,  $\mu(tWZ) = \frac{\sigma(tWZ)}{\sigma(tWZ)_{SM}}$ , from the likelihood fit is measured as,

$$\mu(tWZ) = 1.16^{+1.33}_{-1.30} \quad (4.20)$$

The expected upper limit is in agreement with the extracted best-fit value on the signal strength, therefore no deviations from the SM cross section of  $tWZ$  is observed.

In Table 4.11, the nuisance parameters used in the fit, including which channel's regions are affected by each, are shown.

The expected upper limit of  $tWZ$  across both channels is measured as,

$$\mu_{up}^{exp} = 1.43^{+2.04}_{-1.03} \quad (4.21)$$

The expected significance of  $tWZ$  across both channels is measured as,

$$Z_\mu^{exp} = 1.61\sigma \quad (4.22)$$

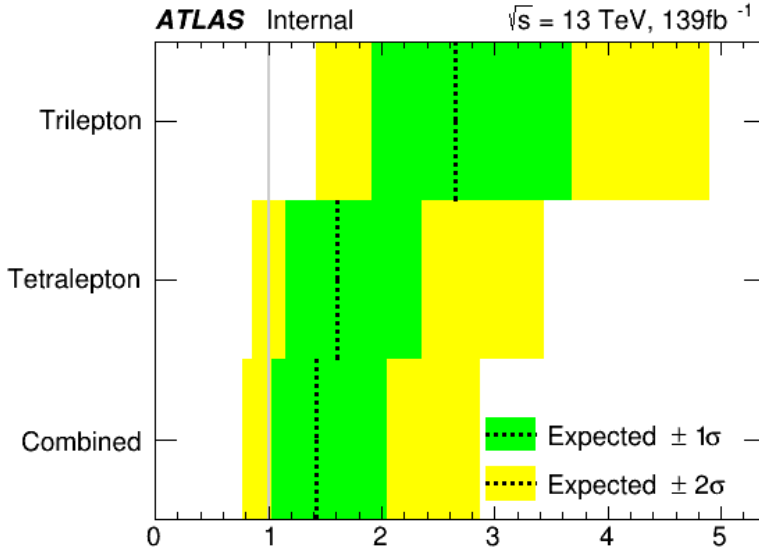


Figure 4.52: The expected upper limits of the trilepton channel, tetralepton channel and both channels combine are shown. The y-axis shows the channels in which the fitting procedure was performed. The expected limits are represented by the vertical dotted line. One- and two-  $\sigma$  uncertainty bands are shown in green and yellow respectively. The vertical grey line indicates when  $\mu(tWZ) = 1$ .

<sup>1294</sup> The best-fit value of the signal strength,  $\mu(tWZ) = \frac{\sigma(tWZ)}{\sigma(tWZ)_{SM}}$ , from the likelihood fit is measured as,

$$\mu(tWZ) = 1.80^{+0.70}_{-0.65} \quad (4.23)$$

<sup>1295</sup> In Figure 4.52, the expected upper limits of the trilepton channel, tetralepton channel and both channels combined  
<sup>1296</sup> are shown.

<sup>1297</sup> It can be seen that the sensitivity of  $tWZ$  is mostly driven by the tetralepton analysis, with the trilepton analysis  
<sup>1298</sup> attributing a small decrease in the expected upper limit of the combined analysis, and its associated uncertainty.

<sup>1299</sup>  
<sup>1300</sup> In Figure 4.53, the best-fit values of  $\mu(tWZ)$  from the fit for the trilepton channel, tetralepton channel and both  
<sup>1301</sup> channels combined are shown.

<sup>1302</sup> It can be seen from Figures 4.52 and 4.53 that the best fit value for the signal strength on  $tWZ$ ,  $\mu(tWZ)$ , and the  
<sup>1303</sup> expected limits for the tri- and tetralepton channels are consistent with one-another (their uncertainties overlap).  
<sup>1304</sup> Therefore it is appropriate to combine these two analyses.

<sup>1305</sup>  
<sup>1306</sup> In Figure 4.54, a ranking plot showing the impact of the systematic uncertainties on the POI,  $\mu(tWZ)$ , in the  
<sup>1307</sup> combined fit across both the tri- and tetralepton channels is shown.

<sup>1308</sup> Some nuisance parameters are pulled down from their nominal pre-fit values, however these are all within 1  $\sigma$   
<sup>1309</sup> uncertainty and are thus relatively small. It is expected that the modelling uncertainties (shape and normalisa-  
<sup>1310</sup> tions) of the most dominant backgrounds (e.g.  $t\bar{t}Z$ ,  $ZZ$ ,  $WZ$ ) have relatively large impacts on  $\mu(tWZ)$ , since the  
<sup>1311</sup> uncertainty of the analysis is dominated by statistical uncertainty.

<sup>1312</sup> The most important systematics are the cross sections of  $t\bar{t}Z$ ,  $ZZ$  and  $WZ + b$ , and shape modelling on  $t\bar{t}Z$   
<sup>1313</sup> ( $t\bar{t}Z$  triangular shape). The aforementioned nuisance parameters are significantly shifted down in the fit from its  
<sup>1314</sup> nominal value. The less important systematics are pulled in the fit from their nominal values, but to a much lesser  
<sup>1315</sup> degree than the cross section of those mentioned above. It is expected that the modelling uncertainties (shape and  
<sup>1316</sup> normalisations) of the most dominant backgrounds (e.g.  $t\bar{t}Z$ ,  $ZZ$  and  $WZ + b$ ) have relatively large impacts on  
<sup>1317</sup>  $\mu(tWZ)$ , since the uncertainty of the analysis is dominated by statistical uncertainty.  
<sup>1318</sup>

#### <sup>1319</sup> 4.11.2.1 Projection to Higher Luminosity

<sup>1320</sup> In this section we apply a fully blinded fit to the ASIMOV dataset for integrated luminosities larger than the  $139\text{fb}^{-1}$   
<sup>1321</sup> currently available from the ATLAS Full Run 2 dataset. This study gives us insight into the sensitivity of  $tWZ$

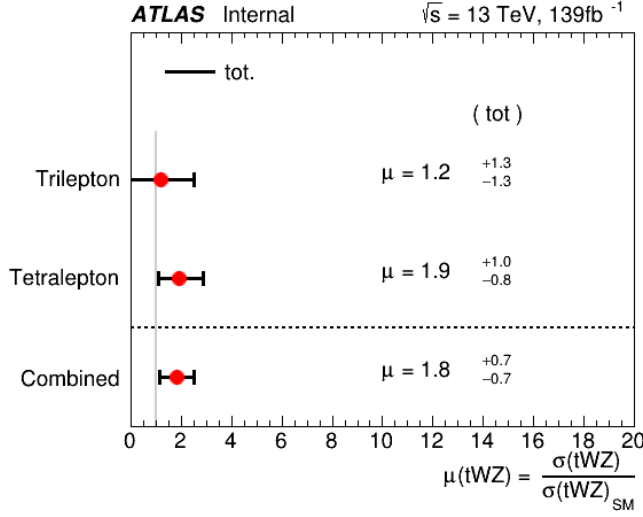


Figure 4.53: The best-fit values of  $\mu(tWZ)$  from the fit for the trilepton channel, tetralepton channel and both channels combined are shown. The y-axis shows the channels in which the fitting procedure was performed. The signal strength  $\mu(tWZ)$  is shown on the x-axis. The nominal signal strengths are represented by the red dots. The total uncertainty associated with the best-fit  $\mu(tWZ)$  value is shown by the black error bars.

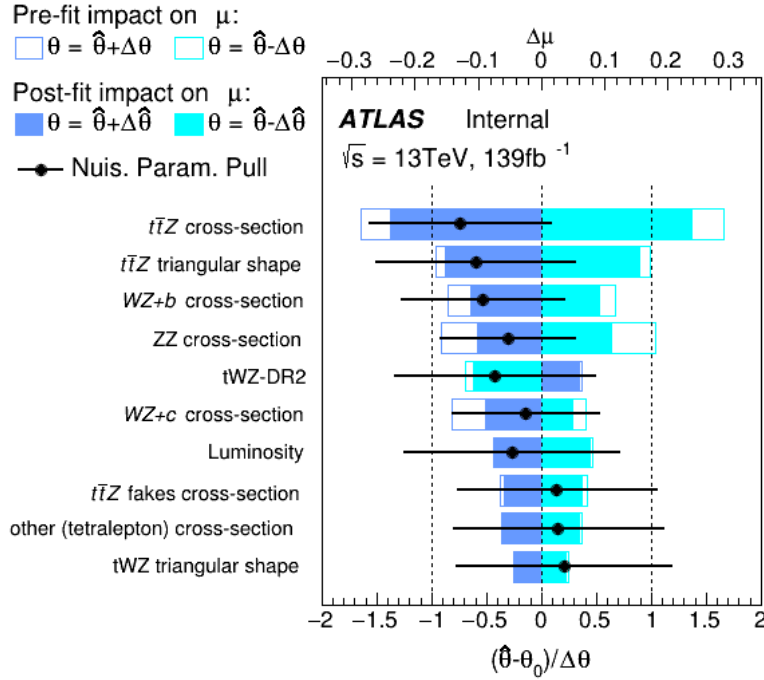


Figure 4.54: A ranking plot showing the impact of the systematic uncertainties (top 10) on the POI,  $\mu(tWZ)$ , in the combined fit across both the tri- and tetralepton channels is shown.  $\hat{\theta}$  is the best-fit value of the nuisance parameter.  $\Delta\hat{\theta}$  and  $\Delta\theta$  are the post-fit and pre-fit uncertainties respectively. The post-fit and pre-fit impact of each nuisance parameter on  $\mu(tWZ)$  are shown with the solid and lined rectangles respectively. The empty and solid blue rectangles correspond to the pre-fit and post-fit impacts on  $\mu(tWZ)$  respectively. These impacts are shown on the upper axis ( $\Delta\mu$ ). On the lower axis, the nuisance parameter pull,  $\frac{\hat{\theta} - \theta_0}{\Delta\theta}$ , is shown ( $\theta_0$  is the nominal pre-fit value of the nuisance parameter). The nuisance parameter pull is indicated by the black points, with their relative post-fit errors ( $\frac{\Delta\hat{\theta}}{\Delta\theta}$ ) shown by the black horizontal error bars.

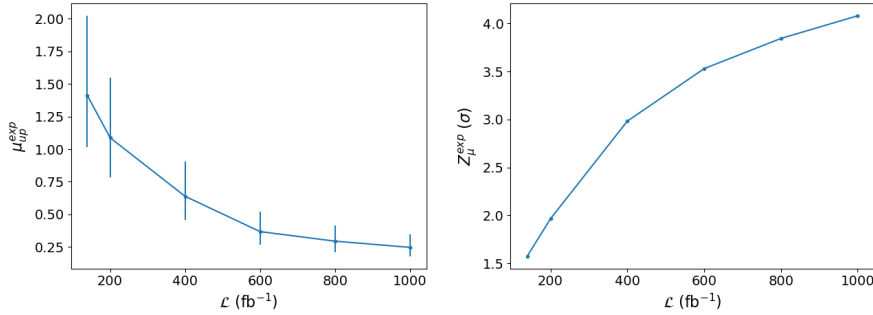


Figure 4.55: The expected upper limit (left) and significance (right) for combined fully blinded fits to the ASIMOV dataset across both the tri- and tetralepton channels for a range integrated luminosities are shown. **Left:** The integrated luminosity,  $\mathcal{L}$ , is shown on the x-axis. The expected upper limit,  $\mu_{up}^{exp}$ , is shown on the y-axis. The vertical lines represent the total uncertainty ( $\pm 1\sigma$ ) on the expected upper limit. **Right:** The integrated luminosity,  $\mathcal{L}$ , is shown on the x-axis. The expected significance,  $Z_\mu^{exp}$ , is shown on the y-axis. The vertical lines represent the total uncertainty ( $\pm 1\sigma$ ) on the expected significance.

1322 which we could expect if we were to replicate the current analysis, given more data. Given the upgrades planned  
1323 for the LHC and the ATLAS detector, we will soon expect an large increase in available  $pp$  collision data (reaching  
1324  $\mathcal{L} = 3000 \text{fb}^{-1}$  [31]). This study therefore gives us an idea of the sensitivity of  $tWZ$  which we can expect in the future.

1325

1326 In Figure 4.55, the expected upper limit and significance for combined fully blinded fits to the ASIMOV dataset  
1327 across both the tri- and tetralepton channels for a range integrated luminosities are shown.

1328 As we increase the total integrated luminosity, the sensitivity of  $tWZ$  increases. The increase in sensitivity is shown  
1329 by the decrease of the expected upper limit and the increase of the expected significance with increasing integrated  
1330 luminosity. It can be noted that a  $3\sigma$  expected significance is achieved at  $\mathcal{L} \sim 400 \text{ fb}^{-1}$ , indicating evidence for  
1331 observation of  $tWZ$ . The  $5\sigma$  significance 'discovery' standard is above our  $1000 \text{fb}^{-1}$  luminosity range of study.  
1332 Furthermore, these plots show that the sensitivity of  $tWZ$  is hindered by the low amount of events we observe,  
1333 rather than the systematic effects. This is evident since increasing the luminosity, therefore increasing the number  
1334 of events we see in the detector, directly causes a steady in increase in sensitivity.

# Chapter 5

## Conclusion

1335

1336

1337 The search for  $tWZ$  production using  $139 \text{ fb}^{-1}$  of  $pp$  collision data at a centre-of-mass energy of  $\sqrt{s} = 13 \text{ TeV}$ ,  
 1338 recorded by the ATLAS experiment at CERN, has been presented. This thesis targeted the tetralepton final state  
 1339 channel. To further increase the sensitivity of  $tWZ$ , a combined analysis was done across the tetralepton and  
 1340 trilepton (studied in an independent analysis by Benjamin Warren (UCT) [80]) channels.

1341 Two SRs and Three CRs were defined. Two SRs, instead of one, were defined in order to suppress and constrain  
 1342 the  $ZZ$  background. The definition of the  $tWZ$  OF SR and the  $tWZ$  SF SR take advantage of the OSSF lepton  
 1343 pairs which originate from the decay of a  $Z$  boson, by requiring that non- $Z$  leptons in the event have the opposite  
 1344 and same flavours, for the  $tWZ$  OF SR and  $tWZ$  SF SR respectively. The resulting SRs successfully separate the  
 1345  $ZZ$  background, with the  $tWZ$  OF SR containing around 6% of the total  $ZZ$  background yield across both regions  
 1346 (implying that the remaining  $\sim 94\%$  is contained in the  $tWZ$  SF SR). The dominant background processes,  $t\bar{t}Z$   
 1347 and  $ZZ$  were constrained by the definition of  $t\bar{t}Z$  and  $ZZ$  CRs, respectively. The dominant source of fake leptons,  
 1348 originating from the  $t\bar{t}Z$  background, was constrained by the  $(tWZ)_{fake}$  CR, using the MC template method.  
 1349

1350 Two BDTs were implemented: an object-level BDT which aims to classify between  $\ell b$  systems coming from top  
 1351 quarks and an event-level BDT which aims to discriminate between  $tWZ$  and our major backgrounds,  $t\bar{t}Z$  and  
 1352  $ZZ$ . The output from the object-level BDT was converted to an event-level variable to be used as input to  
 1353 the event-level BDT. A kinematic reconstruction algorithm,  $2\nu\text{SM}$ , was used to reconstruct top quarks in order  
 1354 to discriminate between  $tWZ$  and  $t\bar{t}Z$ . The output from this algorithm was used as an input variable to the  
 1355 event-level BDT. The trained BDT was shown to discriminate well between signal and background events.

1356 Using a modified ASIMOV dataset in the SRs and real data in the CRs, a blinded maximum-likelihood fit was  
 1357 performed across all regions in the tetralepton channel. The best-fit value of the signal strength in the tetralepton  
 1358 channel was,

$$\mu(tWZ) = 1.91^{+0.95}_{-0.82} \quad (5.1)$$

1359 with an expected significance of  $1.44\sigma$ . The expected upper limit on the signal strength of  $tWZ$  in the tetralepton  
 1360 channel was,

$$\mu_{up}^{exp} = 1.61^{+2.35}_{-1.16} \quad (5.2)$$

1361 Furthermore, a blinded maximum-likelihood fit was performed across all regions across the trilepton and tetralepton  
 1362 channels. The best-fit value of the signal strength across both the trilepton and tetralepton channels were,

$$\mu(tWZ) = 1.80^{+0.70}_{-0.65} \quad (5.3)$$

1363 with an expected significance of  $1.61\sigma$ . The expected upper limit on the signal strength of  $tWZ$  across both the  
 1364 trilepton and tetralepton channels were,

$$\mu_{up}^{exp} = 1.43^{+2.04}_{-1.03} \quad (5.4)$$

1365 Although this result does not satisfy the  $3\sigma$  evidence nor the  $5\sigma$  discovery standards, this is the tightest ever  
 1366 constraint on the  $tWZ$  process. The results in this analysis are heavily statistically limited, we therefore expect  
 1367 that future analyses of this process, using larger datasets (such as that from the HL-LHC), would significantly  
 1368 improve the results.

1371

# Bibliography

- 1372 [1] M. Aaboud et al. “Electron reconstruction and identification in the ATLAS experiment using the 2015 and  
 1373 2016 LHC proton–proton collision data at  $\sqrt{s} = 13$  TeV”. In: *The European Physical Journal C* 79.8 (Aug.  
 1374 2019). ISSN: 1434-6052. DOI: 10.1140/epjc/s10052-019-7140-6. URL: <http://dx.doi.org/10.1140/epjc/s10052-019-7140-6>.
- 1375 [2] M. Aaboud et al. “Measurement of the  $t\bar{t}Z$  and  $t\bar{t}W$  cross sections in proton-proton collisions at  $\sqrt{s} = 13$  TeV  
 1376 with the ATLAS detector”. In: *Phys. Rev. D* 99 (7 Apr. 2019), p. 072009. DOI: 10.1103/PhysRevD.99.072009.  
 1377 URL: <https://link.aps.org/doi/10.1103/PhysRevD.99.072009>.
- 1378 [3] Aaboud, M. and Aad, G. and Abbott, B. and Abbott, D. C. and Abdinov, O. and Abed Abud, A. and  
 1379 Abhayasinghe, D. K. and Abidi, S. H. and AbouZeid, O. S. and et al. “Measurement of ZZ production  
 1380 in the  $\ell\ell\nu\nu$  final state with the ATLAS detector in pp collisions at  $s \sqrt{s} = 13$  TeV”. In: *Journal of High  
 1381 Energy Physics* 2019.10 (Oct. 2019). ISSN: 1029-8479. DOI: {10.1007/jhep10(2019)127}. URL: %7Bhttp:  
 1382 //dx.doi.org/10.1007/JHEP10(2019)127%7D.
- 1383 [4] G. Aad et al. “Measurement of the  $t\bar{t}$  production cross-section in the lepton+jets channel at  $s=13$  TeV  
 1384 with the ATLAS experiment”. In: *Physics Letters B* 810 (2020), p. 135797. ISSN: 0370-2693. DOI: <https://doi.org/10.1016/j.physletb.2020.135797>. URL: <https://www.sciencedirect.com/science/article/pii/S0370269320306006>.
- 1385 [5] G. Aad et al. “Muon reconstruction performance of the ATLAS detector in proton–proton collision data at  
 1386  $\sqrt{s} = 13$  TeV”. In: *The European Physical Journal C* 76.5 (May 2016). ISSN: 1434-6052. DOI: 10.1140/epjc/  
 1387 s10052-016-4120-y. URL: <http://dx.doi.org/10.1140/epjc/s10052-016-4120-y>.
- 1388 [6] Georges Aad et al. “Topological cell clustering in the ATLAS calorimeters and its performance in LHC Run  
 1389 1. Topological cell clustering in the ATLAS calorimeters and its performance in LHC Run 1”. In: *Eur. Phys.  
 1390 J. C* 77 (Mar. 2016), 490. 87 p. DOI: 10.1140/epjc/s10052-017-5004-5. arXiv: 1603.02934. URL:  
 1391 <https://cds.cern.ch/record/2138166>.
- 1392 [7] Shunichi Akatsuka and Shion Chen. *Isolation WPs summary: PLV + LowPtPLV*. Oct. 2019. URL: <https://indico.cern.ch/event/854783/contributions/3595486/attachments/1929380/3195230/PLV-Summary.pdf>.
- 1393 [8] Aaron Armbruster. *Asymptotic Formulae*. Feb. 2013. URL: [https://indico.cern.ch/event/233551/contributions/493678/attachments/389871/542293/asymptotics\\_armbruster.pdf](https://indico.cern.ch/event/233551/contributions/493678/attachments/389871/542293/asymptotics_armbruster.pdf).
- 1394 [9] Pierre Astier et al. “Kalman filter track fits and track breakpoint analysis”. In: *Nuclear Instruments and  
 1395 Methods in Physics Research Section A: Accelerators, Spectrometers, Detectors and Associated Equipment*  
 1396 450.1 (2000), pp. 138–154. ISSN: 0168-9002. DOI: [https://doi.org/10.1016/S0168-9002\(00\)00154-6](https://doi.org/10.1016/S0168-9002(00)00154-6). URL:  
 1397 <https://www.sciencedirect.com/science/article/pii/S0168900200001546>.
- 1398 [10] ATLAS Collaboration. “ATLAS  $b$ -jet identification performance and efficiency measurement with  $t\bar{t}$  events in  
 1399  $pp$  collisions at  $\text{sqrt}s = 13$  TeV”. In: *Eur. Phys. J. C* 79 (2019), p. 970. DOI: 10.1140/epjc/s10052-019-  
 1400 7450-8. arXiv: 1907.05120 [hep-ex].
- 1401 [11] ATLAS Collaboration. *Calibration of light-flavour  $b$ -jet mistagging rates using ATLAS proton–proton collision  
 1402 data at  $\text{sqrt}s = 13$  TeV*. ATLAS-CONF-2018-006. 2018. URL: <https://cds.cern.ch/record/2314418>.
- 1403 [12] ATLAS Collaboration. “Electron and photon performance measurements with the ATLAS detector using  
 1404 the 2015-2017 LHC proton-proton collision data”. In: *JINST* 14 (2019), P12006. DOI: 10.1088/1748-  
 1405 0221/14/12/P12006. arXiv: 1908.00005 [hep-ex].
- 1406 [13] ATLAS Collaboration. “Performance of the ATLAS muon reconstruction in proton–proton collisions at  
 1407  $\sqrt{s} = 13$  TeV”. In: *Eur. Phys. J. C* 79.10 (Oct. 2019). ISSN: 1434-6052. DOI: 10.1140/epjc/  
 1408 s10052-019-7140-6. URL: <http://dx.doi.org/10.1140/epjc/s10052-019-7140-6>.
- 1409 [14] ATLAS Collaboration. “Performance of the ATLAS electron reconstruction in proton–proton collisions at  
 1410  $\sqrt{s} = 13$  TeV”. In: *Eur. Phys. J. C* 79.10 (Oct. 2019). ISSN: 1434-6052. DOI: 10.1140/epjc/  
 1411 s10052-019-7141-5. URL: <http://dx.doi.org/10.1140/epjc/s10052-019-7141-5>.

- [13] ATLAS Collaboration. “Identification and rejection of pile-up jets at high pseudorapidity with the ATLAS detector”. In: *Eur. Phys. J. C* 77 (2017), p. 580. DOI: 10.1140/epjc/s10052-017-5081-5. arXiv: 1705.02211 [hep-ex].
- [14] ATLAS Collaboration. *Measurement of b-tagging efficiency of c-jets in  $t\bar{t}$  events using a likelihood approach with the ATLAS detector*. ATLAS-CONF-2018-001. 2018. URL: <https://cds.cern.ch/record/2306649>.
- [15] ATLAS Collaboration. “Measurements of b-jet tagging efficiency with the ATLAS detector using  $t\bar{t}$  events at  $\sqrt{s} = 13\text{TeV}$ ”. In: *JHEP* 08 (2018), p. 089. DOI: 10.1007/JHEP08(2018)089. arXiv: 1805.01845 [hep-ex].
- [16] ATLAS Collaboration. “Muon reconstruction and identification efficiency in ATLAS using the full Run 2  $pp$  collision data set at  $\sqrt{s} = 13\text{TeV}$ ”. In: (2020). arXiv: 2012.00578 [hep-ex].
- [17] Manuel Guth on behalf of the ATLAS collaboration. *Deep-Neural-Network-based b-Tagging as Basis for Improvements in Top Analyses*. URL: <https://cds.cern.ch/record/2693088/files/ATL-PHYS-SLIDE-2019-751.pdf>.
- [18] ATLAS Internal. *Electron Efficiencies for Analyses*. 2021. URL: <https://twiki.cern.ch/twiki/bin/viewauth/AtlasProtected/ElectronEfficienciesForAnalysis>.
- [19] ATLAS Internal. *Electron Efficiency Correlation Model*. 2021. URL: <https://twiki.cern.ch/twiki/bin/view/AtlasProtected/ElectronEfficiencyCorrelationModel>.
- [20] ATLAS Internal. *Jet Vertex Tagger for Run 2 in reco and analysis*. 2021. URL: <https://twiki.cern.ch/twiki/bin/view/AtlasProtected/JetVertexTaggerTool>.
- [21] ATLAS Internal. *Muon Efficiencies for Analyses*. 2021. URL: <https://twiki.cern.ch/twiki/bin/view/AtlasProtected/MuonEfficienciesForAnalysis>.
- [22] G. Avoni et al. “The new LUCID-2 detector for luminosity measurement and monitoring in ATLAS”. In: *JINST* 13.07 (2018), P07017. DOI: 10.1088/1748-0221/13/07/P07017.
- [23] Richard D. Ball et al. “Parton distributions for the LHC run II”. In: *Journal of High Energy Physics* 2015.4 (Apr. 2015). ISSN: 1029-8479. DOI: 10.1007/jhep04(2015)040. URL: [http://dx.doi.org/10.1007/JHEP04\(2015\)040](http://dx.doi.org/10.1007/JHEP04(2015)040).
- [24] Olga Bessidskaia Bylund. *Measurement of ttZ and ttW production at ATLAS in 13 TeV data, using trilepton and same charge dimuon final states*. Tech. rep. Geneva: CERN, Aug. 2016. DOI: 10.22323/1.276.0237. URL: <http://cds.cern.ch/record/2211022>.
- [25] Ilaria Brivio and Michael Trott. “The standard model as an effective field theory”. In: *Physics Reports* 793 (Feb. 2019), pp. 1–98. ISSN: 0370-1573. DOI: 10.1016/j.physrep.2018.11.002. URL: <http://dx.doi.org/10.1016/j.physrep.2018.11.002>.
- [26] Oliver Sim Brüning et al. *LHC Design Report*. CERN Yellow Reports: Monographs. Geneva: CERN, 2004. DOI: 10.5170/CERN-2004-003-V-1. URL: <https://cds.cern.ch/record/782076>.
- [27] Matteo Cacciari, Gavin P. Salam, and Gregory Soyez. “The anti- $k_t$  jet clustering algorithm”. In: *JHEP* 04 (2008), p. 063. DOI: 10.1088/1126-6708/2008/04/063. arXiv: 0802.1189 [hep-ph].
- [28] Thomas Calvet. *Automatic binning implementation in TTHTFitter - Htop(bb)*. URL: [https://indico.cern.ch/event/455289/contributions/1953694/attachments/1209081/1762963/Calvet\\_binning\\_Htop-160108.pdf](https://indico.cern.ch/event/455289/contributions/1953694/attachments/1209081/1762963/Calvet_binning_Htop-160108.pdf).
- [29] Anadi Canepa. “Searches for supersymmetry at the Large Hadron Collider”. In: *Reviews in Physics* 4 (2019), p. 100033. ISSN: 2405-4283. DOI: <https://doi.org/10.1016/j.revip.2019.100033>. URL: <https://www.sciencedirect.com/science/article/pii/S2405428318300091>.
- [30] CERN Twiki - TOP WG Summary Plots. URL: <https://twiki.cern.ch/twiki/bin/view/LHCPhysics/LHCTopWGSummaryPlots>.
- [31] CERN Yellow Reports: Monographs. *CERN Yellow Reports: Monographs, Vol. 10 (2020): High-Luminosity Large Hadron Collider (HL-LHC): Technical design report*. en. 2020. DOI: 10.23731/CYRM-2020-0010. URL: <https://e-publishing.cern.ch/index.php/CYRM/issue/view/127>.
- [32] Masud Chaichian, Ricardo Gonzalez Felipe, and Katri Huitu. “On quadratic divergences and the Higgs mass”. In: *Physics Letters B* 363.1-2 (Nov. 1995), pp. 101–105. ISSN: 0370-2693. DOI: 10.1016/0370-2693(95)01191-r. URL: [http://dx.doi.org/10.1016/0370-2693\(95\)01191-R](http://dx.doi.org/10.1016/0370-2693(95)01191-R).

- [33] Shion Chen. *Track isolation variable for the PFlow WPs*. Oct. 2019. URL: [https://indico.cern.ch/event/854783/contributions/3595529/attachments/1926980/3190772/IFF\\_20191003\\_PflowWPs.pdf](https://indico.cern.ch/event/854783/contributions/3595529/attachments/1926980/3190772/IFF_20191003_PflowWPs.pdf).
- [34] KyungEon Choi. “Tracking and Vertexing with the ATLAS Inner Detector in the LHC Run-2”. In: *Springer Proc. Phys.* 213 (2018). Ed. by Zhen-An Liu, pp. 400–403. DOI: 10.1007/978-981-13-1316-5\_75.
- [35] CMS Collaboration. *Measurements of  $pp \rightarrow ZZ$  production cross sections and constraints on anomalous triple gauge couplings at  $\sqrt{s} = 13$  TeV*. 2020. arXiv: {2009.01186} (hep-ex).
- [36] The ATLAS Collaboration et al. “The ATLAS Experiment at the CERN Large Hadron Collider”. In: *Journal of Instrumentation* 3.08 (Aug. 2008), S08003–S08003. DOI: 10.1088/1748-0221/3/08/s08003. URL: <https://doi.org/10.1088/1748-0221/3/08/s08003>.
- [37] I. Connolly. “Performance and calibration of b-tagging with the ATLAS experiment at LHC Run-2”. In: 2017.
- [38] Glen Cowan et al. “Asymptotic formulae for likelihood-based tests of new physics”. In: *The European Physical Journal C* 71.2 (Feb. 2011). ISSN: 1434-6052. DOI: 10.1140/epjc/s10052-011-1554-0. URL: <http://dx.doi.org/10.1140/epjc/s10052-011-1554-0>.
- [39] Federico Demartin et al. “tWH associated production at the LHC”. In: *Eur. Phys. J. C* 77.1 (2017), p. 34. DOI: 10.1140/epjc/s10052-017-4601-7. arXiv: 1607.05862 [hep-ph].
- [40] *Electron identification efficiency in data for electrons with  $E_T > 30\text{GeV}$* . URL: [https://atlas.web.cern.ch/Atlas/GROUPS/PHYSICS/PAPERS/EGAM-2018-01/fig\\_16.png](https://atlas.web.cern.ch/Atlas/GROUPS/PHYSICS/PAPERS/EGAM-2018-01/fig_16.png).
- [41] F. Englert and R. Brout. “Broken Symmetry and the Mass of Gauge Vector Mesons”. In: *Phys. Rev. Lett.* 13 (9 Aug. 1964), pp. 321–323. DOI: 10.1103/PhysRevLett.13.321. URL: <https://link.aps.org/doi/10.1103/PhysRevLett.13.321>.
- [42] *Errors in weighted histograms*. URL: <https://www.zeuthen.desy.de/~wischnew/amanda/discussion/wgterror/working.html>.
- [43] Lyndon Evans and Philip Bryant. “LHC Machine”. In: *Journal of Instrumentation* 3.08 (Aug. 2008), S08001–S08001. DOI: 10.1088/1748-0221/3/08/s08001. URL: <https://doi.org/10.1088/1748-0221/3/08/s08001>.
- [44] Guido Fantini et al. *The formalism of neutrino oscillations: an introduction*. 2020. arXiv: 1802.05781 [hep-ph].
- [45] Steve Farrell. *Overlap Removal Tools, FTAG/Hbb Workshop*. URL: [https://indico.cern.ch/event/631313/contributions/2683959/attachments/1518878/2373377/Farrell\\_ORTools\\_ftaghbb.pdf](https://indico.cern.ch/event/631313/contributions/2683959/attachments/1518878/2373377/Farrell_ORTools_ftaghbb.pdf).
- [46] *GoodRunListsForAnalysisRun2*. URL: <https://twiki.cern.ch/twiki/bin/viewauth/AtlasProtected/GoodRunListsForAnalysisRun2>.
- [47] Particle Data Group et al. “Review of Particle Physics”. In: *Progress of Theoretical and Experimental Physics* 2020.8 (Aug. 2020). 083C01. ISSN: 2050-3911. DOI: 10.1093/ptep/ptaa104. eprint: <https://academic.oup.com/ptep/article-pdf/2020/8/083C01/33653179/ptaa104.pdf>. URL: <https://doi.org/10.1093/ptep/ptaa104>.
- [48] Peter W. Higgs. “Broken Symmetries and the Masses of Gauge Bosons”. In: *Phys. Rev. Lett.* 13 (1964). Ed. by J. C. Taylor, pp. 508–509. DOI: 10.1103/PhysRevLett.13.508.
- [49] Peter W. Higgs. “Spontaneous Symmetry Breakdown without Massless Bosons”. In: *Phys. Rev.* 145 (1966), pp. 1156–1163. DOI: 10.1103/PhysRev.145.1156.
- [50] *IFFTruthClassifier GitLab Repository*. URL: <https://gitlab.cern.ch/ATLAS-IFF/IFFTruthClassifier/-/tree/master>.
- [51] *IFFTruthClassifier Lepton Categories*. URL: <https://gitlab.cern.ch/ATLAS-IFF/IFFTruthClassifier/-/tree/master#3-details-about-the-lepton-categories>.
- [52] N. Jarosik et al. “SEVEN-YEAR WILKINSON MICROWAVE ANISOTROPY PROBE (WMAP) OBSERVATIONS: SKY MAPS, SYSTEMATIC ERRORS, AND BASIC RESULTS”. In: *The Astrophysical Journal Supplement Series* 192.2 (Jan. 2011), p. 14. ISSN: 1538-4365. DOI: 10.1088/0067-0049/192/2/14. URL: <http://dx.doi.org/10.1088/0067-0049/192/2/14>.
- [53] F. Jegerlehner. “The hierarchy problem of the electroweak Standard Model revisited”. In: (May 2013).

- [54] V. Khachatryan et al. “Measurement of the ZZ production cross section and  $Z \rightarrow \ell^+\ell^-\ell^+\ell^-$  branching fraction in pp collisions at  $\sqrt{s} = 13\text{TeV}$ ”. In: *Physics Letters B* 763 (2016), pp. 280–303. ISSN: 0370-2693. DOI: <https://doi.org/10.1016/j.physletb.2016.10.054>. URL: <https://www.sciencedirect.com/science/article/pii/S0370269316306256>.
- [55] H. J. W. Kirsten. *Introduction to supersymmetry*. Singapore Hackensack, NJ: World Scientific, 2010. ISBN: 978-9814293426.
- [56] Fabio Maltoni, Luca Mantani, and Ken Mimasu. “Top-quark electroweak interactions at high energy”. In: *Journal of High Energy Physics* 2019.10 (Oct. 2019). ISSN: 1029-8479. DOI: 10.1007/jhep10(2019)004. URL: [http://dx.doi.org/10.1007/JHEP10\(2019\)004](http://dx.doi.org/10.1007/JHEP10(2019)004).
- [57] Luigi Marchese. *Lepton and photon reconstruction and identification performance in ATLAS and CMS*. Tech. rep. Geneva: CERN, Sept. 2019. DOI: 10.22323/1.350.0237. URL: <https://cds.cern.ch/record/2688452>.
- [58] Thomas McCarthy. *Macro developed to compare t/W/Z reconstruction performance (2ℓ, 3ℓ, 4ℓ)*. URL: [https://indico.cern.ch/event/986357/contributions/4172907/attachments/2169451/3666801/reco-performance\\_macro\\_20210112.pdf](https://indico.cern.ch/event/986357/contributions/4172907/attachments/2169451/3666801/reco-performance_macro_20210112.pdf).
- [59] Thomas McCarthy and Florian Fischer. *Exploiting full/partial  $t\bar{t}$  reconstruction for background suppression in 2ℓ*. URL: [https://indico.cern.ch/event/955360/contributions/4016465/attachments/2102418/3534816/top\\_reco\\_bkgd\\_suppression\\_2L\\_20200915.pdf](https://indico.cern.ch/event/955360/contributions/4016465/attachments/2102418/3534816/top_reco_bkgd_suppression_2L_20200915.pdf).
- [60] *MCTruthClassifier - ATLAS Twiki*. URL: <https://twiki.cern.ch/twiki/bin/view/AtlasProtected/MCTruthClassifier>.
- [61] F. Meloni. “Primary vertex reconstruction with the ATLAS detector”. In: *Journal of Instrumentation* 11.12 (Dec. 2016), pp. C12060–C12060. DOI: 10.1088/1748-0221/11/12/c12060. URL: <https://doi.org/10.1088/1748-0221/11/12/c12060>.
- [62] Ken Mimasu. *Top quark electroweak interactions*. 2021. arXiv: 2105.10261 [hep-ph].
- [63] Users MissMJ and Cush. *Standard model of elementary particles - Wikimedia Commons*. URL: [https://en.wikipedia.org/wiki/File:Standard\\_Model\\_of\\_Elementary\\_Particles.svg](https://en.wikipedia.org/wiki/File:Standard_Model_of_Elementary_Particles.svg).
- [64] *Monte Carlo to Monte Carlo scale factors for flavour tagging efficiency calibration*. Tech. rep. ATL-PHYS-PUB-2020-009. Geneva: CERN, May 2020. URL: <https://cds.cern.ch/record/2718610>.
- [65] *MuonSelectionTool, ATLAS TWiki*. URL: <https://twiki.cern.ch/twiki/bin/view/Atlas/MuonSelectionTool>.
- [66] O Oncel. *Search for Single Top Quark Production in Association with a W and a Z Boson in the 3 Lepton Final State with the ATLAS Experiment at 13 TeV*. URL: <https://cds.cern.ch/record/2625170>.
- [67] *Option to force a shape withing an error band by hand - TRF documentation*. URL: [https://trexfitter-docs.web.cern.ch/trexfitter-docs/model\\_building/shape/](https://trexfitter-docs.web.cern.ch/trexfitter-docs/model_building/shape/).
- [68] *Pileup jet recommendations*. URL: <https://twiki.cern.ch/twiki/bin/view/AtlasProtected/PileupJetRecommendations>.
- [69] *Recommended isolation working points*. URL: <https://twiki.cern.ch/twiki/bin/view/AtlasProtected/RecommendedIsolationWPs>.
- [70] *scikit-learn Documentation - Gradient Boosting Classifier*. URL: <https://scikit-learn.org/stable/modules/generated/sklearn.ensemble.GradientBoostingClassifier.html>.
- [71] *Scikit-Learn GradientBoostingClassifier Documentation*. URL: <https://scikit-learn.org/stable/modules/generated/sklearn.ensemble.GradientBoostingClassifier.html>.
- [72] Pedro Ferreira da Silva. *Top quark production at the LHC*. 2016. arXiv: 1605.05343 [hep-ex].
- [73] Jory Sonneveld. *Searches for physics beyond the standard model at the LHC*. 2019. arXiv: 1905.06239 [hep-ex].
- [74] Mark Thomson. *Modern particle physics*. Cambridge, United Kingdom New York: Cambridge University Press, 2013. ISBN: 9781107034266.
- [75] *TopRecoObjTwikiModel*. URL: <https://twiki.cern.ch/twiki/bin/view/AtlasProtected/TopRecoObjTwikiModel>.
- [76] *Total Integrated Luminosity and Data Quality in 2015-2018 - LuminosityPublicResultsRun2*. URL: <https://twiki.cern.ch/twiki/bin/view/AtlasPublic/LuminosityPublicResultsRun2>.

- 1560 [77] Daniel R. Tovey. “Transformation properties of the transverse mass under transverse Lorentz boosts at hadron  
1561 colliders”. In: *The European Physical Journal C* 79.4 (Apr. 2019). ISSN: 1434-6052. DOI: 10.1140/epjc/  
1562 s10052-019-6813-5. URL: <http://dx.doi.org/10.1140/epjc/s10052-019-6813-5>.
- 1563 [78] *TRExFitter*. URL: <https://twiki.cern.ch/twiki/bin/viewauth/AtlasProtected/TtHFitter>.
- 1564 [79] *TRExFitter: Mixed data and MC fit*. URL: <https://trexfitter-docs.web.cern.ch/trexfitter-docs/>  
1565 AdvancedTutorial2020/Mixed/.
- 1566 [80] Benjamin Warren. “A search for tWZ production in the trilepton channel using Run 2 data from the ATLAS  
1567 experiment.” In: (2021).
- 1568 [81] Kenneth G. Wilson. “Confinement of quarks”. In: *Phys. Rev. D* 10 (8 Oct. 1974), pp. 2445–2459. DOI: 10.  
1569 1103/PhysRevD.10.2445. URL: <https://link.aps.org/doi/10.1103/PhysRevD.10.2445>.